

Tunnel Boring Machine Excavation Fluids: From Laboratory to Practice

Dongzhu Zheng

Doctoral dissertation submitted to obtain the academic degree of
Doctor of Civil Engineering

Supervisors

Prof. Adam Bezuijen, PhD* - Prof. Gemmina Di Emidio, PhD* - Tiago Gerheim Souza Dias,
PhD**

* Department of Civil Engineering
Faculty of Engineering and Architecture, Ghent University

** Geotechnical Consulting Group, United Kingdom

August 2021

ISBN 978-94-6355-508-1

NUR 956

Wettelijk depot: D/2021/10.500/56

Members of the Examination Board

Chair

Prof. Em. Luc Taerwe, PhD, Ghent University

Other members entitled to vote

Prof. Hans De Backer, PhD, Ghent University

Prof. Wim Haegeman, PhD, Ghent University

Prof. Em. Robert Mair, PhD, University of Cambridge, United Kingdom

Prof. Mike Mooney, PhD, Colorado School of Mines, USA

Prof. Markus Thewes, PhD, Ruhr-Universität Bochum, Germany

Supervisors

Prof. Adam Bezuijen, PhD, Ghent University

Prof. Gemmina Di Emidio, PhD, Ghent University

Tiago Gerheim Souza Dias, PhD, Geotechnical Consulting Group, United Kingdom

Acknowledgement

I would like to express my sincere gratitude to my supervisor Prof. Adam Bezuijen, who has given me the opportunity to pursue my research together with him. His insights into the nature of research have always inspired me the most. I have got enormous support and encouragement from Prof. Bezuijen while exploring freely in research.

The financial support from China Scholarship Council is greatly appreciated.

Thanks to Prof. Gemmina Di Emidio and Dr. Tiago Dias for their technical suggestions during my research.

I would like to say thanks to Prof. Markus Thewes in Ruhr-University, Bochum, Germany. His genuine help during my research experiments and the technical suggestions in the writing have deeply touched me.

Thanks to the technicians Filip and Jan for their help during my experiments, also to Marius and Sascha at RUB for their help during my visits in Bochum.

Thanks to the secretaries, Linda and Hilde at UGent, and Fabiana at RUB, for their help with office works.

Thanks to the professors and colleagues for their assistance during my research. Special thanks are attributed to my dear friends (Kristine, Pham, Michela, Hamzeh, Ehsan, Alessandro, Ecem, Khan, Hao, Tao, Peng. L, Chenhui, Jinquan, Peng. J, Jianguo, Zhongtian, Chenghao) from the Laboratory of Geotechnics who have made my life abroad colorful. I will never forget the joyful moments we had spent together.

Last but not least, I wish to thank my beloved family who have supported me all the time. Your endless love is a torch through the long tunnel of my life.

Table of contents

TABLE OF CONTENTS	VII
LIST OF NOTATIONS	XI
GLOSSARY OF ABBREVIATIONS AND TERMS USED IN THE STUDY	XV
ABSTRACT	XVII
SAMENVATTING	XXI
CHAPTER 1 INTRODUCTION	1
1.1 BACKGROUND	1
1.2 PROBLEM STATEMENT	4
1.3 CENTRAL OBJECTIVES	6
1.4 OUTLINE OF THE THESIS.....	7
CHAPTER 2 PRESSURE INFILTRATION OF FOAM INTO SATURATED SAND AND ITS CONSEQUENCE FOR EPB SHIELD TUNNELING	9
2.1 INTRODUCTION.....	9
2.2 EXPERIMENTAL SET-UP.....	11
2.2.1 <i>Modified pressure transducers</i>	14
2.3 MATERIALS.....	16
2.3.1 <i>Foam</i>	16
2.3.2 <i>Sand</i>	17
2.4 EXPERIMENTAL PROCEDURE	17
2.5 RESULTS AND DISCUSSION.....	19
2.5.1 <i>Volume and discharge</i>	19
2.5.2 <i>Pore water pressures</i>	27
2.6 VERIFICATION TEST	39
2.7 FIELD MEASUREMENTS.....	42
2.8 CHAPTER SUMMARY	46
CHAPTER 3 MODELLING THE INFILTRATION BEHAVIOR OF FOAM INTO SATURATED	

SAND CONSIDERING THE CAPILLARY RESISTANCE	49
3.1 INTRODUCTION TO THE INFILTRATION MODEL.....	49
3.2 MECHANISMS DURING FOAM INFILTRATION.....	51
3.3 MODEL DERIVATION	52
3.4 RESULTS AND DISCUSSION.....	63
3.4.1 <i>Maximum penetration depth</i>	63
3.4.2 <i>Model simulation</i>	65
3.5 CHAPTER SUMMARY	72
CHAPTER 4 EXPERIMENTAL STUDY ON SANDY FOAM INFILTRATION INTO SATURATED SAND FOR EPB SHIELD TUNNELING: A MECHANISM STUDY	73
4.1 INTRODUCTION.....	73
4.2 DEFINITIONS.....	75
4.3 EXPERIMENTAL STUDY.....	76
4.3.1 <i>Foam, sand and foam-sand mixture</i>	76
4.3.2 <i>Set-up and procedure</i>	79
4.4 RESULTS.....	80
4.4.1 <i>Discharge</i>	80
4.4.2 <i>Pressure</i>	87
4.4.3 <i>Permeabilities</i>	98
4.5 DISCUSSION.....	108
4.6 CHAPTER SUMMARY	110
CHAPTER 5 SURFACE TENSION OF FOAM AND ITS INFLUENCE ON TUNNELING..	113
5.1 INTRODUCTION.....	113
5.2 MATERIALS AND PROCEDURE.....	115
5.2.1 <i>Foaming liquid and capillary tube</i>	115
5.2.2 <i>Procedure</i>	115
5.3 RESULTS AND DISCUSSION.....	116
5.4 CHAPTER SUMMARY	128
CHAPTER 6 A NEW MODEL FOR PREDICTING THE MARSH FUNNEL TEST	131

6.1 INTRODUCTION.....	131
6.2 MARSH FUNNEL GEOMETRY	133
6.3 THEORETICAL DEVELOPMENT.....	134
6.3.1 Rheology model.....	134
6.3.2 Model assumptions:	135
6.3.3 Model derivation	135
6.4 EXPERIMENTAL VERIFICATION	139
6.5 DISCUSSION.....	145
6.6 CHAPTER SUMMARY	149
CHAPTER 7 CLOSING REMARKS.....	151
7.1 SUMMARY.....	151
7.2 CONCLUSIONS AND RECOMMENDATIONS FOR FUTURE WORK	152
APPENDIX: RESULTS FOR ALL PURE FOAM INFILTRATION TESTS.....	157
DISCHARGE	157
PORE WATER PRESSURES	158
REFERENCES	165

List of notations

A_C	cross-sectional area of the sand column
C	consistency index
$C. \%$	concentration of foaming liquid
$C. ' \%$	concentration of the foaming liquid in the foam-soil-mixture
c_v	Terzaghi's consolidation coefficient
d	local diameter at the narrowest point in the throat among sand grains
D	local diameter on top of the bubble
D_1	diameter of the big cylinder
D_2	diameter of the smaller cylinder
D_{15}	diameter at which 15% of the filter material's mass content smaller than
D_c	characteristic length scale
D_i	diameter at point i
D_s	average diameter of the sand grains
$F(\tau_0, \alpha, z)$	function representing the upward pressure induced by the sidewall in the conical section
FER_a	FER at atmospheric pressure
FER_p	FER at the desired air pressure
g	acceleration of gravity
h	capillary rise in the tube
H_F	maximum filling height of the conical section of the funnel
i	number of bubble penetrations across the pore throat
i_1	hydraulic gradient in the mixture
i_2	hydraulic gradient in the saturated sand

i_t	threshold hydraulic gradient
k_f	permeability of the sand for foam
k_{fw}	permeability of foam
k_m	permeability of the mixture
k_s	permeability of the saturated sand
L	length of the capillary tube
L_m	maximum penetration depth by foam bubbles
L_{s1}	length of the big cylinder
L_{s2}	length of the small cylinder
M	maximum value of i
m_v	compressibility
n	flow index
n_{max}	Maximum porosity of the sand
n_{min}	Minimum porosity of the sand
n_s	porosity of the sand column
N	number of bubbles along the maximum penetration depth
p	desired air pressure
p_d	pressure drop due to the dynamic force
P	atmospheric pressure
P_a	pressure inside the bubble
Pe	Peclet number
P_s	suction pressure (negative)
P_w	surrounding pore pressure
P_{w1}	pore water pressure on top of the bubble
P_{w2}	pore water pressure at the bottom of the bubble
Q	discharge

r	local radius of the fluid in the conical section of the funnel
R	radius of the tube
s	radius of the bubble after compression
S	radius of the bubble
R_F	maximum radius of the fluid in the conical section of the funnel
U	characteristic velocity
v	mean velocity of the fluid
v_f	penetration velocity of the foam bubbles
V_{pw}	volume of expelled water
V_s	volume quantity of the foaming agent
V_w	quantity of water
x	penetration depth by the foam bubbles
x'	distance between the foam bubble front and the invisible liquid front
X	infiltration depth
z	height from the top of the capillary tube to the liquid surface
α	angle between the funnel wall and the vertical direction
β	under-relaxation factor
δ	volume ratio between the bubble and the pore space
ϕ_0	piezometric head at the foam front
$\phi_{0,end}$	piezometric head of the foam front at maximum penetration depth
ϕ_i	piezometric head in the foam above the sand level
γ	surface tension of foam
γ_w	surface tension of water
θ	contact angle between the wall and the liquid
λ	pore water replacement
ρ	density of fluid

ρ_a	density of air
ρ_w	density of water
τ	shear stress
τ_0	yield stress
τ_w	wall shear stress
$\tau_{w\ new}$	new value in calculation
$\tau_{w\ old}$	previous value in calculation
ΔL	distance between two adjacent pressure transducers
ΔP	total excess pore pressure
ΔP_a	increase in air pressure inside the bubble
ΔP_{cone}	pressure loss due to yield stress in the conical section of the funnel
ΔP_{tot}	hydrostatic pressure minus the pressure loss due in the conical section of the funnel
ΔP_w	excess pore pressure
$\Delta \phi$	corresponding difference in piezometric head between adjacent pressure transducers
$\Delta \phi_1$	drop in piezometric head in the large cylinder
$\Delta \phi_2$	drop in piezometric head due to the contraction from the large cylinder to the small cylinder
$\Delta \phi_3$	drop in piezometric head in the small cylinder

Glossary of abbreviations and terms used in the study

Deep bed filtration	filtration of the bentonite particles by the slurry infiltrated sand
Drainage	the separation of foaming liquid from foam
EPB	earth pressure balance shield
External cake	a low permeable layer formed due to the filter cake formation in slurry infiltration
Filter cake formation	consolidation of the bentonite particles in the slurry
FIR	foam injection ratio, the ratio between the volume of the injected foam and the excavated soils
Foam spurt	infiltration of foam bubbles into saturated sand
Further infiltration	infiltration of foam bubbles into the saturated sand after foam spurt
Internal cake	a low permeable layer formed due to slurry or foam infiltration
MF	Marsh funnel test
Mud spurt	infiltration of slurry into saturated sand
PWR	pore water replacement, the expelled pore water (λ) from a unit soil divided by the soil porosity (n_s)
TBM	tunnel boring machine
Threshold gradient	the minimum hydraulic gradient required to initiate the Bingham flow in porous medium

Abstract

Tunneling under soft ground conditions often requires active face support to prevent face instability. Foam in an Earth Pressure Balance (EPB) shield Tunnel Boring Machine (TBM) and slurry in a slurry shield TBM are the most common materials for the realization of this support pressure. During ring building at standstill, there will be a filter cake formed at the tunnel face in a slurry shield TBM that could effectively transfer the fluid pressure to the soils. For an EPB shield the foam will have roughly the same function as the slurry in a slurry shield TBM, however, the details of supporting mechanisms are still not fully understood.

The first part of this work aims to study the foam infiltration behavior that may influence the pressure development during standstill. Experiments on pure foam infiltration into saturated sand with different influencing factors such as foam expansion ratio (FER), and sand types were examined. The infiltration characteristics were compared with slurry infiltration and the mechanisms are discussed. Results suggest that the pressure drop can be realized over the foam infiltration zone during foam spurt. There is a maximum infiltration depth by foam during foam spurt. Development of pore pressures shows that the foam infiltrated area functions similarly to an internal cake at the tunnel face of a slurry shield. Verification tests indicate that the permeability of the whole system is determined by the foam infiltrated sand instead of the foam on top of the sand, which is different to the filter cake in a slurry infiltration. Further infiltration that is comparable to the deep bed filtration in a slurry infiltration was found to be the main process after foam spurt. Experimental results were compared with the results field measurement data from the Botlek Rail Tunnel.

Following the improved understanding on the mechanisms during pure foam infiltration, a theoretical study was carried out to interpret the experimental results. The numerical model is based on an infiltration model for slurry infiltration, which considers foam spurt during foam infiltration. The maximum penetration depth by foam bubbles was first estimated by a simplified micro stability model which is based on the limit equilibrium analysis due to capillary resistance. Results from the numerical model were in accordance with the measured discharge behavior during

foam spurt from experiments. The general agreements suggest that the model can explain the foam flow behavior and can be used to describe foam spurt during foam infiltration that can be expected in EPB shield tunneling.

With the improved understanding on pure foam infiltration mechanisms, the infiltration characteristics of sandy foam infiltration into saturated sand were experimentally investigated. Influencing factors including foam injection ratio (FIR) and water content of the foam-sand mixture were studied. Consolidation of the foam-sand mixture is the dominant process as found by comparing the permeabilities at different locations during the test. No foam infiltration could be expected with a FIR lower than 40 Vol % for the fine sand used in the experiments. While foam infiltration with a higher FIR results in a foam infiltration layer that has a lower permeability than the consolidated mixture. It was found that the sand matrix plays an important role in determining the permeability of a sand-foam mixture. As the permeability of the consolidated mixture close to the sand surface is smaller than that far away from the sand surface. Since the consolidated mixture close to the sand surface is subjected to considerable foam loss due to foam infiltration, the sand grains are more compacted than the consolidated mixture far away from the sand surface. Combining the micro stability model for pure foam penetration, the criteria for bubble penetration during sandy foam infiltration were discussed. Based on the analysis, the theoretical value for the permeability of a foam-sand mixture was derived and compared with the recommended values from EFNARC (2005). General agreements were obtained.

In field applications during tunneling, foam is usually injected into the excavation chamber where pore water from the excavated soils will dilute the concentration of foam. This dilution effect will influence the surface tension of foam which may further influence the engineering properties of the foam-soil mixture. The values of surface tension at different concentrations were measured with the capillary rise method. Consequences for the volume change and the compressibility were theoretically investigated while the consequences for the infiltration behavior were experimentally investigated. Results suggest that, during tunneling, the surface tension of the diluted foam can be twice the value of original foam. The influences on the volume change and the compressibility can be negligible for the foams used in tunneling. While it

may have a negative influence on the formation of a foam infiltration layer that has a lower permeability. Results suggest that the dilution of foam by pore water should be considered when studying the foam infiltration behavior. Further foam-soil interaction could also be influenced by this dilution effect which is worth further investigation.

In the second part of the thesis, a new model for predicting the Marsh funnel (MF) test was proposed and validated through experiments. The new model aims at evaluating the bentonite slurries for the slurry shield TBM or Horizontal Directional Drilling (HDD). The physical model accounts for the pressure drop in the upper conical section due to the yield stress of the fluids as well as the dynamic pressure in the lower capillary tube. Results show that for bentonite slurries with a small MF value, the dynamic pressure in the test plays a dominant role that must be taken into consideration. Further discussions show that the two-point measurement in field tests can be used as a fast estimation of the rheological parameters for the bentonite slurries.

Samenvatting

Het boren van een tunnel in slappe grond vereist vaak actieve boorfrontondersteuning om instabiliteit van het boorfront te voorkomen. Schuim in een EPB-schild TBM en slurry in een sluryschild TBM zijn de meest voorkomende toevoegingen voor het realiseren van deze steundruk. Tijdens ringbouw, wanneer er niet wordt geboord, zal er een slecht doorlatende filterkoek gevormd worden aan het boorfront bij een slurryschild TBM die de vloeistofdruk effectief naar de bodem kan overbrengen. Voor een EPB-schild met schuim zal het schuim de doorlatendheid aan het boorfront verlagen. Voor die situatie zijn de ondersteuningsmechanismen echter nog steeds niet volledig begrepen.

Deze studie heeft tot doel het gedrag van schuiminfiltratie te bestuderen dat de ontwikkeling van de boorfrontdruk tijdens boren en stilstand kan beïnvloeden. De studie onderzoekt eerst het gedrag van pure schuiminfiltratie. De resultaten van experimenten met pure schuiminfiltratie in verzadigd zand worden behandeld. Hierin is de invloed van de schuimexpansieverhouding (FER) en zandsoort onderzocht. De infiltratiekarakteristieken worden vergeleken met slurry-infiltratie en de mechanismen worden besproken. Resultaten suggereren dat de drukval aan het boorfront wordt gerealiseerd over een dunne schuiminfiltratiezone tijdens schuimspurt. Er is een maximale infiltratiediepte van enkele centimeters van het schuim tijdens schuimspurt. Ontwikkeling van poriëndrukken toont aan dat het met schuim geïnfiltreerde gebied op dezelfde manier functioneert als een interne filterkoek aan het boorfront van een slurryschild. Verificatietests gaven aan dat de doorlatendheid van het hele systeem wordt bepaald door het met schuim geïnfiltreerde zand in plaats van het schuim bovenop het zand, terwijl bij een slurry-infiltratie de filterkoek op het zand de doorlatendheid bepaalt. Verdere infiltratie, vergelijkbaar is met de diepfiltratie bij slurry-infiltratie, blijkt het belangrijkste proces te zijn na de schuimspurt. De experimentele resultaten in het laboratorium worden vergeleken met veldmeetgegevens van de Botlekspoortunnel.

Met behulp van de resultaten is een rekenmodel opgesteld. Dit model is gebaseerd op een infiltratiemodel voor slurry-infiltratie, waarbij rekening wordt gehouden met

schuimspurt tijdens schuiminfiltratie. De maximale infiltratiediepte die het schuim kan bereiken wordt geschat met een vereenvoudigd microstabiliteitsmodel. Vergelijking tussen het microstabiliteitsmodel en de experimentele resultaten laat over het algemeen een goede overeenkomst zien, behalve voor één van de mediumzanden die in de experimenten is gebruikt. De mogelijke reden hiervoor wordt besproken. De resultaten van numerieke simulatie zijn in lijn met de gemeten waterafvoer tijdens schuimspurt. Dit suggereert dat de fysica juist is gemodelleerd.

Met het verbeterde begrip van de infiltratiemechanismen van puur schuim, worden de infiltratiekarakteristieken van zandige schuiminfiltratie in verzadigd zand experimenteel onderzocht. Factoren die van invloed zijn, zoals de FIR en het watergehalte van het schuim-zandmengsel, worden bestudeerd. Voor deze situatie blijkt niet indringing van het schuim in het zand, maar consolidatie van het schuim-zandmengsel het proces dat bepalend is voor de doorlatendheid. Dit blijkt door de doorlatendheden op verschillende locaties tijdens de test te vergelijken. Er blijkt geen schuiminfiltratie op te treden bij een FIR lager dan 40% voor het fijne zand dat in het experiment werd gebruikt. Terwijl schuiminfiltratie met een hogere FIR resulteert in een schuiminfiltratielaag die een lagere doorlatendheid heeft dan het geconsolideerde mengsel. De zandmatrix speelt een belangrijke rol bij het bepalen van de doorlatendheid van een zand-schuimmengsel. Omdat de doorlatendheid van het geconsolideerde mengsel dichtbij het zandoppervlak aan het boorfront kleiner is dan die verderop in de mengkamer. Het geconsolideerde mengsel nabij het zandoppervlak zal verdichten door de schuiminfiltratie. De criteria voor bellenpenetratie tijdens zandige schuiminfiltratie worden besproken in combinatie met het microstabiliteitsmodel voor schuimpenetratie. Op basis van de analyse wordt de theoretische waarde voor de doorlatendheid van een schuim-zandmengsel afgeleid en vergeleken met de aanbevolen waarden uit EFNARC (2005).

Bij veldtoepassingen tijdens het tunnelen wordt schuim meestal aan het boorfront of in de mengkamer geïnjecteerd, waar het poriënwater uit de uitgegraven bodem de schuimconcentratie zal verdunnen. Dit verdunningseffect zal de oppervlaktespanning van schuim beïnvloeden, wat weer van invloed is op de technische eigenschappen van het schuim-grondmengsel. De oppervlaktespanning is gemeten bij verschillende

concentraties surfactants in water met de capillaire stijgingsmethode. De invloed van de oppervlaktespanning voor de volumeverandering en de samendrukbaarheid zijn theoretisch onderzocht, terwijl de gevolgen voor het infiltratiegedrag experimenteel zijn onderzocht. Resultaten suggereren dat de oppervlaktespanning van het schuim in de mengkamer tweemaal zo groot kan zijn als die van het originele schuim. De invloed van deze verhoogde oppervlaktespanning op de volumeverandering en de samendrukbaarheid zullen verwaarloosbaar zijn voor de schuimen die bij het tunnelen worden gebruikt. Wel zal deze hogere oppervlaktespanning een negatieve invloed kunnen hebben op de vorming van een schuiminfiltratielaag wat resulteert in een hogere doorlatendheid van die laag. De resultaten suggereren dat de verdunning van schuim door poriënwater in overweging moet worden genomen bij het bestuderen van het schuiminfiltratiegedrag. Verdere interactie tussen schuim en bodem kan ook worden beïnvloed door dit verdunningseffect. Hiervoor is nader onderzoek nodig.

In het tweede deel van het proefschrift wordt een nieuw model voor het voorspellen van de Marsh-trechter-test voorgesteld en gevalideerd door middel van experimenten. Het nieuwe model is gericht op het evalueren van de bentonietslurries voor bijvoorbeeld een slurryschild TBM of HDD (Horizontal Directional Drilling). Het rekenmodel gaat uit van een Herschel-Bulkley vloeistof en houdt rekening met de drukval in het bovenste conische gedeelte als gevolg van de vloeispanning van de vloeistoffen en de statische en dynamische drukval in het onderste capillaire buisje. De resultaten laten zien dat voor bentonietslurries met een lage MF-waarde, de dynamische druk in de test een dominante rol speelt waarmee rekening moet worden gehouden. In veldproeven kan een tweepuntsmeting worden gebruikt als een snelle schatting van de reologische parameters voor bentonietslurries.

Chapter 1 Introduction

1.1 Background

The proper use of underground space has become an alternative to the growing need for public transportation nowadays in urban areas and city centers. Mechanized tunneling has shown to be an unprecedented success in the past few decades for its great advantage over conventional tunneling technologies. It is especially favored in densely populated areas where it is often required to avoid disturbance to existing structures and roads as much as possible. This has been one of the major concerns when met with soft ground conditions for which the tunnel face stability during construction is of great importance.

Tunneling under soft ground conditions always requires active face support to prevent face collapse and to reduce ground settlement (Bezuijen, 2020; Mooney et al., 2016; Thewes et al., 2012; Mair, 2011; Peila et al., 2009; Anagnostou & Kovári, 1996). For the excavation under the groundwater table, the support pressure should be able to counterbalance the earth pressure as well as the water pressure.

The application of the Earth Pressure Balance (EPB) shield Tunnel Boring Machine (TBM) for tunneling under soft ground conditions has gained quite some popularity since its first successful application in Japan (Herrenknecht et al., 2011). There are several operating modes in an EPB shield TBM: the open mode requires no face support in case the surrounding rock is rather stable; the semi open mode makes use of compressed air for face support in the upper part of the excavation chamber, while the lower part is filled with the excavated soils for temporarily stable ground conditions; the closed mode requires active face support to prevent face instability in unstable ground conditions. In this thesis, the close EPB mode with active face support will be studied.

In the close EPB shield mode, the support makes use of the excavated soils (Budach & Thewes, 2018; Bezuijen & Dias, 2017; Talmon & Bezuijen, 2002; Broere & van Tol, 2001; Quebaud et al., 1998). Originally designed for soils with at least 30% of

shown in Figure 1-1. The pore pressures in front of the tunnel face can be predicted with the groundwater flow model by Bezuijen (2002). Field measurements have shown that the groundwater flow in front of an EPB shield is comparable to that in front of a slurry shield as the excess pore pressure in front of the tunnel face of both shields can be predicted by the same model (see Figure 1-2).

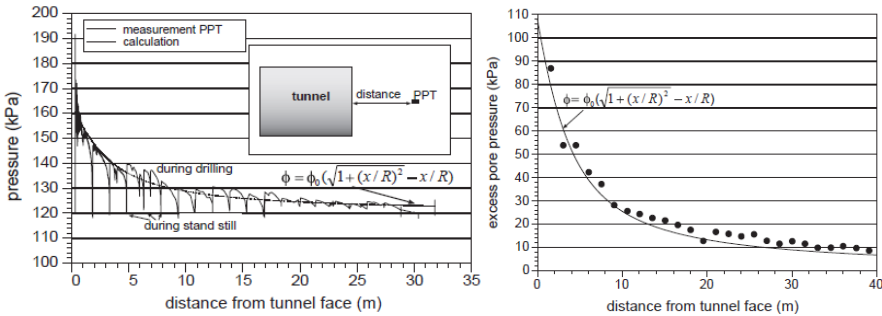


Figure 1-2. Measured excess pore pressure in front of the tunnel face and approximation (Bezuijen, 2002). (Left - slurry shield: 2nd Heinenoord Tunnel; right - EPB shield: Botlek Rail Tunnel, MQ1 South)

In a slurry shield, the support pressure is realized through the bentonite slurry in the excavation chamber (Xu & Bezuijen, 2019; Zizka et al., 2018; Talmon et al., 2013; Broere & van Tol, 2000; Anagnostou & Kovári, 1994). The support pressure is controlled by the slurry feed pipe and/or the air bubble in the pressure bulkhead behind the excavation chamber. Due to the high viscosity and the yield strength of the bentonite slurry, its infiltration into the soil will lead to a low permeable area and the fluid pressure can be partly or fully transferred to the soils in front of the tunnel face. Extensive studies have shown that in front of a slurry shield TBM, the slurry pressure can be transferred to the soil skeleton by the formation of a filter cake (Xu et al., 2018; Zizka et al., 2018; Talmon et al., 2013; Min et al., 2013). Such a filter cake will not form during drilling in saturated sand, because when it starts to form, it will be ‘eaten’ by the TBM (Bezuijen et al., 2016; Broere & van Tol, 2000). During drilling in saturated sand, excess pore water pressures are generated in front of the TBM depending on the permeability of the soil and the advance rate of the TBM. A slurry infiltrated area can form in front of the TBM, which is often addressed as the internal cake in front of a slurry shield TBM.

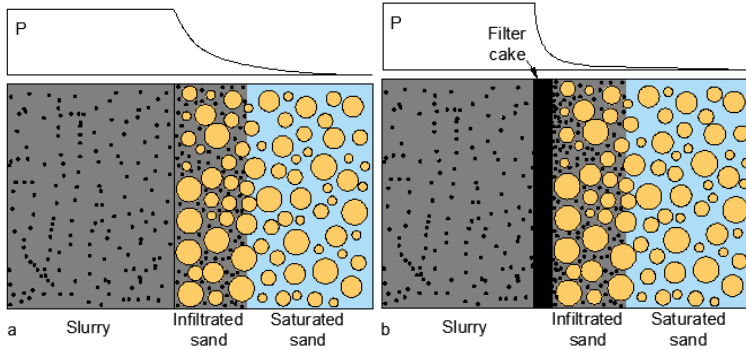


Figure 1-3. Pressure infiltration (a) and pressure filtration (b) processes during slurry infiltration.

As shown in Figure 1-3, there are two separate processes that can be characterized by pressure infiltration and pressure filtration in a typical slurry infiltration (Bezuijen, 2010). During pressure infiltration (Figure 1-3a), the finer particles and the water in the slurry will be pushed into the sand pores while the larger particles remain at the boundary of the sand. The discharged water flow in this stage is dominated by the bentonite flow. The pressure infiltration process results in a mud spurt period. After some infiltration depth, consolidation of the slurry will begin at the boundary of the sand where both the larger and finer bentonite particles will begin to remain, while water flow continues as long as there is a pressure gradient but with a much smaller discharge rate. This will accelerate the consolidation and with the ongoing consolidation of the slurry, the filter cake becomes thicker and the water discharge will be further reduced and will be proportional to the square root of time (Talmon et al., 2013). The permeability of the whole system is determined by the filter cake formed on top of the sand because there are much more finer bentonite particles inside the filter cake than that in the slurry infiltrated sand.

1.2 Problem statement

Although the pressure control can be different in the two types of TBM, the support principle in a slurry shield and an EPB shield is the same since the pressure is directly applied to the materials in the excavation chamber in both types of the TBM. While the supporting mechanisms might not be the same.

There are two processes in a typical slurry infiltration: mud spurt (pressure infiltration) and filter cake formation (pressure filtration) (Xu et al., 2018; Zizka et al., 2018; Talmon et al., 2013; Min et al., 2013). An external filter cake is expected at the later stage of slurry infiltration after mud spurt. Due to the low permeability of the filter cake, the pressure drop within the filter cake can be large enough so that the fluid pressure could be effectively transferred to the soils ahead in order to support the tunnel face. Although an external filter cake is not expected during drilling due to the constant cutting action, it is supposed to play an important role during standstill and in case of chamber intervention. During drilling, the rotating cutting wheel removes (partly) the slurry infiltrated soils so that only slurry infiltration is possible after every tool passage. On the one hand, the soils can be partly stabilized with the seepage force induced by the groundwater flow. On the other hand, mud spurt will result in an internal cake with a low permeability through which the fluid pressure can be partly transferred to the soil skeleton.

Although the development of excess pore pressure in front of an EPB shield is comparable to that in front of a slurry shield, the pressure transfer mechanism during foam infiltration has not been well understood compared with that during slurry infiltration. Xu (2018) showed that ‘foam spurt’ can be expected in the beginning of a foam infiltration compared to mud spurt in a slurry infiltration. However, it was only qualitatively identified by the discharged water in a fine sand sample. More information is needed such as pore pressures during foam infiltration in order to better explain the foam infiltration characteristics. Besides that, the foam infiltration behavior for a coarser sand should also be studied to get a general understanding since the EPB shield TBM is widely used in coarse-grained soils. Therefore, the slurry infiltration characteristics in a slurry shield and the foam infiltration characteristics in an EPB shield are fundamental in the understanding of the supporting mechanism. Moreover, the infiltration behavior from the foam-sand mixture into saturated sand is also worth investigation.

Bentonite slurries are constantly used in field applications for slurry shields TBM. A fast and robust testing method is needed for determining the rheological properties of these slurries on job site. As these rheological properties will influence the slurry

infiltration behaviors that are directly related to the pressure transfer mechanisms. It should be possible to vary the density and the viscosity of the bentonite slurry according to the engineering requirements such as the fluidity regarding the transportation and the infiltration characteristics regarding the pressure control in the excavation chamber. As it is required in a new generation of multi-mode TBM called Variable Density TBM, in which the density and the viscosity of the slurries were changed for different ground conditions (Bäppler et al., 2018).

The Marsh funnel (MF) test has been widely used in the oil industry for nearly a century to evaluate the viscosity of oils. It has been adopted in other disciplines such as grouting application and drilling industry for fast evaluation of the target fluids. More recently, it has been included as one of the testing methods in tunneling applications. Traditionally, the Marsh funnel test only results in one value, the MF time (Marsh funnel viscosity). For Newtonian fluids such as oils, the test is ideal since only viscosity needs to be determined. While for non-Newtonian fluids, more rheological parameters are of interest such as the yield stress, the consistency index and the flow index. For this reason, the Marsh funnel viscosity becomes insufficient for the complete characterization of these fluids. A more appropriate model to describe the bentonite fluid flow in a Marsh funnel test is therefore needed for field use in tunneling applications.

The issues mentioned above are closely related to field applications that understandings on the foam-sand interactions as well as the process of non-Newtonian fluids in a Marsh funnel test should be improved. Although the influence from the rheological properties on the slurry infiltration behaviors remains an interesting topic, this thesis will only focus on the first step of characterization on the rheological properties using the MF test. These will require experimental characterization as well as model development. To ensure that, the findings could also be calibrated and validated with field measurements.

1.3 Central objectives

In this thesis, the pressurized foam infiltration characteristics will be experimentally investigated to better understand the mechanism of foam infiltration that is expected

in tunneling applications. The experiments consist of two parts, one is pure foam infiltration and the other the sandy foam infiltration. The development of pore pressures during foam infiltration will be investigated both during pure foam infiltration and sandy foam infiltration.

Results will be compared with field measurements of the Botlek Rail tunnel constructed in the Netherlands. Apart from experiments, the foam infiltration process will be modeled following the clarified mechanisms. The model could also be combined with the foam infiltration behavior from foam-sand mixture to saturated sand to give some interesting interpretations. The influence from the change in surface tension of the foam due to dilution in tunneling will also be investigated and discussed.

Regarding the modeling of the MF test, a more applicable physical model for field use is proposed. The model is aimed at bentonite fluids that have smaller Marsh funnel viscosities in which the dynamic force will play an important role in the modeling work. Experiments are conducted to validate the model. Further application using the Marsh funnel test data to predict the rheological parameters of the tested fluids is introduced.

1.4 Outline of the thesis

There are 7 chapters in the thesis. Chapters 2 will present the experimental investigation of pressure infiltration from foam into saturated sand. Chapter 3 presents the model interpretation of pure foam infiltration behaviors as shown in Chapter 2. Chapter 4 contains the extended work on sandy foam infiltration into saturated sand. Chapter 5 analyses the change in surface tension due to dilution that could be expected in excavation chamber and its consequences for tunneling. Chapter 6 presents the new model for the MF test. Summaries, conclusions and recommendations for future work will be presented in Chapter 7.

Chapter 2 Pressure infiltration of foam into saturated sand and its consequence for EPB shield tunneling

This chapter is adapted from the technical paper: Zheng, D., Bezuijen, A. & Thewes, M. 2021. An experimental study on foam infiltration into saturated sand and its consequence for EPB shield tunneling. TUST 111: <https://doi.org/10.1016/j.tust.2021.103878>

This chapter presents the experimental investigation of pressure infiltration from foam into saturated sand. The focus is to investigate the foam infiltration characteristics in comparison with slurry infiltration. Results suggest that a pressure drop can be realized over the foam infiltrated area during foam spurt, suggesting that the supporting pressure can be applied to the soils in front of a tunnel face during ring building at standstill. Development of pore pressures shows that the foam infiltrated area functions similarly to an internal cake at the tunnel face of a slurry shield. Verification tests indicate that the permeability of the whole system is determined by the foam infiltrated sand instead of the foam itself, different to the situation in a slurry infiltration. In the meanwhile, further infiltration phenomenon of foam bubbles was found in the experiment to be the main process after the foam spurt period. General agreement was found when comparing the experimental results with field measurement data from the Botlek Rail Tunnel.

2.1 Introduction

As introduced in Chapter 1, the support pressure in the excavation chamber of an EPB shield is a fluid pressure. The fluid pressure can be applied to the tunnel face to avoid face instability, on the condition that the permeability of the soils at the tunnel face is decreased to the extent that the state of ‘micro stability’ is reached (Bezuijen & Xu, 2019). According to Van Rhee and Bezuijen (1992), in case of a vertical slope in a saturated sand condition, the hydraulic gradient perpendicular and inward directed into the slope should be at least 3 in order to prevent face instability. However, hydraulic gradients in the field are seldom much greater than 1 (Mitchell, 1976). For

instance, in the model described by Bezuijen (2002), the hydraulic gradient in field condition is only 1 with a shield diameter of 10 m and an excess pore pressure of 50 kPa. To increase the local hydraulic gradient, the appropriated additives, slurry for a slurry shield or foam for an EPB shield, should be able to decrease the local permeability in the soils at the tunnel face.

Maidl (1995) carried out some pioneering work in the foam penetration experiment. The experimental results revealed that there are two phases during foam penetration: the fast penetration and the slow but constant penetration rate. Quebaud et al. (1998) also conducted some foam penetration tests. They made use of an apparatus where the foam was pressurized into the soil and found that the initial 30 mm of penetration length occurred almost instantaneously. However, the penetration rate in such a test is significantly influenced by the hydraulic gradient. Considering that the hydraulic gradient in a field condition may be much lower than that in a laboratory set-up, the initial penetration rate of foam can be much smaller in the starting penetration period. Bezuijen & Schaminée (1999) did some mixing tests with foam. In these tests, the pore water replacement in sand by foam was varied. They found that the permeability of such a mixture depends significantly on the amount of remaining pore water. Galli (2016) conducted a series of experiments on foam penetration into cohesionless soils. The objective was to assess the residual water content during drilling of an EPB shield TBM, so the test duration was 3 minutes. The infiltration process was described with the water discharge and quantified with regression analysis. Xu (2018) compared the infiltration characteristics between slurry and foam infiltration tests and found that a comparable “foam spurt” period is also present in the beginning of the tests with foam. Also, the infiltration depth of foam into sand decreases with increasing foam expansion ratio (FER) until FER of 15. However, only one fine sand was used in the experiment by Xu (2018) and foam spurt was only qualitatively identified with the discharged water.

The research reviewed above indicates that the mechanism of foam infiltration is still not clearly understood compared with the mechanism during slurry infiltration. It is therefore interesting to explore the foam infiltration characteristics. In this chapter, foam infiltration experiments are conducted to investigate the change of pore water

pressures during standstill which comprises of ring building and other unplanned downtime. A laboratory set-up that provides a comparable hydraulic gradient to field behavior is employed in the study. Modified pore pressure transducers are developed in order to correctly measure the pore water pressure during foam infiltration. The experiments were conducted with different types of sand in combination with foam of different FERs. The pore pressure transfer mechanism during foam infiltration is first analyzed and discussed. Special attention is focused on the pressure development during fast infiltration period when the foam infiltration velocity is relatively high, and mostly happens during tunnel excavation. Two additional tests are conducted to explore whether there is a consolidation process at the boundary of the sand during foam spurt. Field measurement data from Botlek Rail Tunnel are compared with the experimental interpretation.

2.2 Experimental set-up

Figure 2-1 shows the schematic view of the experimental set-up during this study. Five pore pressure transducers (k1, k2, k3, k4 and k5) are installed on the wall of the Perspex cylinder to measure the pressure head in the foam and also in the sand sample during test. Specifically, k1 is placed in foam which is 2 cm above the foam-sand boundary. k2 is 2 cm below the foam-sand boundary and k4 and k5 are located below k2 with the depths of 6 cm and 10 cm with respect to the foam-sand boundary, respectively. k3 is located not in the same vertical line with the other four, but the vertical distance between k2 and k3 is 2 cm.

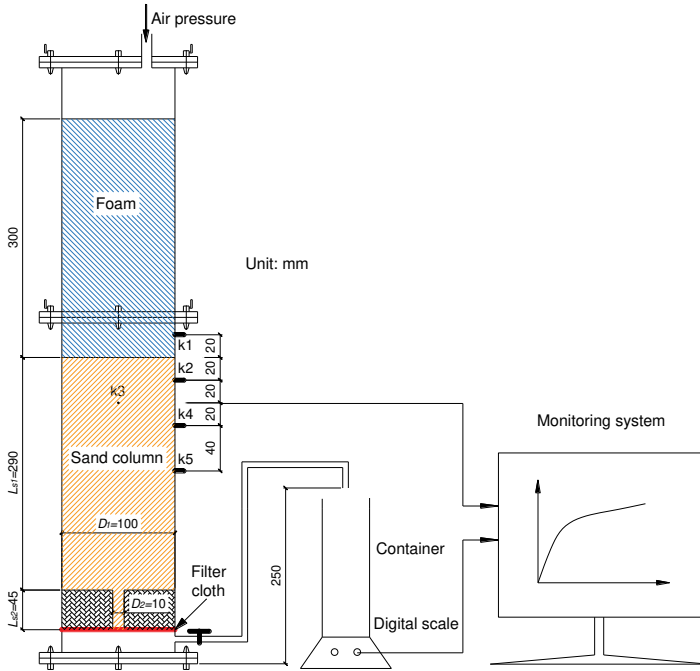


Figure 2-1. Schematic view of the experimental set-up.

This set-up is similar to what Xu and Bezuijen (2018) used in their experiments where the hydraulic gradient was comparable to what can be expected in front of a slurry TBM. In this set-up, a small cylinder is added to create an extra flow resistance. The schematic view of the flow lines is shown in Figure 2-2. Assume a steady water flow through the sand from the large cylinder to the small cylinder. The piezometric head at the sand surface is ϕ_1 and the drop in piezometric head in the large and the small cylinder is $\Delta\phi_1$ and $\Delta\phi_3$, respectively. $\Delta\phi_2$ represents the drop in piezometric head when the flow has to concentrate from the large cylinder to the small cylinder.

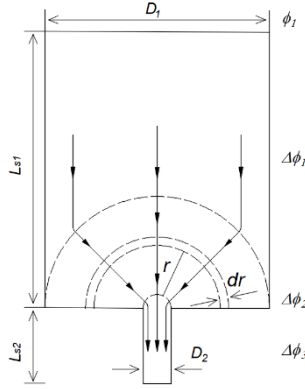


Figure 2-2. Schematic view of the flow lines from the large cylinder to the small cylinder.

The following relations can be obtained since the flow rate (Q) is the same everywhere.

$$Q = k \frac{\Delta\phi_1}{L_{s1}} \frac{\pi D_1^2}{4} \quad (2-1)$$

$$Q = k \frac{\Delta\phi_3}{L_{s2}} \frac{\pi D_2^2}{4} \quad (2-2)$$

With L_{s1} the length of the big cylinder, L_{s2} the length of the small cylinder, D_1 the diameter of the large cylinder and D_2 the diameter of the smaller cylinder.

Assume a circular flow from the larger cylinder to the smaller cylinder, the drop in piezometric head in a small area as indicated in Figure 2-2 is (flow in a half-sphere):

$$Q = 2\pi k r^2 \frac{d\phi}{dr} \quad (2-3)$$

Integration from $D_1/2$ to $D_2/2$ it comes to:

$$Q = \frac{\pi k \Delta\phi_2}{1/D_2 - 1/D_1} \quad (2-4)$$

The total drop in piezometric head is ϕ_1 , leading to:

$$\phi_1 = \Delta\phi_1 + \Delta\phi_2 + \Delta\phi_3 \quad (2-5)$$

Combining the above equations yields:

$$\phi_1 = \Delta\phi_1 \left(1 + \frac{L_{s2}}{L_{s1}} \frac{D_1^2}{D_2^2} + \frac{D_1^2}{4D_2 L_{s1}} - \frac{D_1}{4L_{s1}} \right) \quad (2-6)$$

Consider an equivalent cylinder length (L_s) with the same diameter and the same flow rate to the large cylinder, the relation can be described as:

$$k \frac{\Delta\phi_1}{L_{s1}} = k \frac{\phi_1}{L_s} \quad (2-7)$$

The equivalent length is then obtained:

$$L_s = L_{s1} + L_{s2} \left(\frac{D_1}{D_2} \right)^2 + \frac{D_1^2}{4D_2} - \frac{D_1}{4} \quad (2-8)$$

With the dimensions in this set-up (two layers: 45 mm thick in the small cylinder and 290 mm thick in the large cylinder), the equivalent length calculated by Equation (2-8) will be about 5 m. Applying an air pressure of 50 kPa will result in a hydraulic gradient of $\Delta\phi/L_s = 1$. This is comparable to the hydraulic gradient predicted by the groundwater flow model described in Bezuijen (2002) with a shield diameter of 10 m and an excess pore water pressure of 50 kPa. Although there is 0.25 m of elevation during the test by the discharge line as shown in Figure 2-2, the elevation effect can be negligible compared with 5 m of piezometric head. Numerical simulations (Zizka et al., 2017; Bezuijen et al., 2001) and field measurements (Bezuijen, 2002) have shown the feasibility of the groundwater flow model. It essentially means that the measured foam penetration velocity in this experiment will be almost the same to what can be expected in front of an EPB shield.

2.2.1 Modified pressure transducers

In the experiment, Honeywell-24PCCFA6G miniature low-pressure transducers were utilized. By using a Wheatstone bridge, the pressure transducer provides a signal that is proportional to the applied pressure. This is realized by the four active piezo resistors that form the Wheatstone bridge. For this principle, the pressure transducer itself cannot distinguish between pore water pressure or grain stresses in a porous medium. Moreover, due to the special structure of this pressure transducer, there is a small chamber in front of the Wheatstone bridge. On the one hand, soil particles may reside inside the chamber, which may result in the measurement of effective stress. On the other hand, the foam bubbles can get into the small chamber during test and thus influence the measurement result.

Therefore, a proper filter system was developed to ensure the transmission of pore water pressure from the porous medium to the pressure transducer. In order to transfer pore water pressure, a water reservoir in contact with the pressure transducer must be created by a proper filter system. In the meanwhile, foam is comprised of more than 90% of air which is highly compressible and should be prohibited in the water reservoir. Consequently, the filter system should also be able to stop the foam bubbles from entering the water reservoir.

Concerning the aforementioned requirements, the filter system plays an important role in the measurement of pore water pressure. Two essential functions of the filter system can be categorized into the following specifications:

1) Solid / liquid separation. The compartment filled with water must be able to stop the sand grains from entering, while water could interact freely with the entrapped water to transfer the pore water pressure.

2) Water / foam bubble separation. The most important function of the filter system is the prevention of foam bubbles from entering the compartment. Air in the foam bubbles is highly compressible and could induce a delayed response when pressure is applied. The pore size of the filter membrane should be small enough to keep foam bubbles outside the compartment while water could easily flow through the filter.

Considering these specifications, the pressure transducer was modified in the lab of UGent by adding a hydrophilic filter membrane (Millipore, PVDF/HVPP hydrophilic filter) that was used by Oung and Bezuijen (2003). The pore size is $0.45\ \mu\text{m}$ and the thickness $115\ \mu\text{m}$. The water compartment was realized by a stainless-steel housing. Two perforated stainless-steel plates were put inside the steel housing to hold the membrane for robustness while the drilled holes ($0.5\ \text{mm}$ in diameter at the back side and $1\ \text{mm}$ at the front side of the chamber) allow the pressure transfer of the fluids. O-ring was used for airtight sealing to make sure only water can travel through the filter membrane. The pressure transducer head including the chamber, the filter membrane and the perforated stainless steel were immersed in water and set in a vacuum for 24 hours. This procedure ensures that the compartment and the filter membrane is deaired and saturated. A schematic view of the pressure transducer

modification is shown in Figure 2-3.

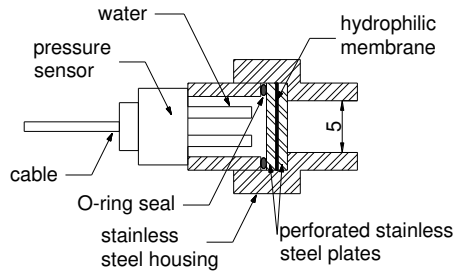


Figure 2-3. Schematic view of the pressure transducer installation (unit: mm)

2.3 Materials

2.3.1 Foam

Foam was produced using a small laboratory foam generator used by Galli (2016). The surfactant used was Condat CLB F5/TM in a concentration of 3.0 M %. The foam used in the experiment was first generated under atmospheric pressure and then filled inside the cylinder. Applying an excess pressure will cause a volume decrease of the foam and thus decreases the FER of the foam. In this research, the FER will represent the ratio between the volume of foam and the volume of the foaming liquid under applied pressure in accordance with EFNARC (2005). The choice of FER may be influenced by ground types, since a clayey soil may absorb water from foam, the FER should be smaller for fine-grained soils to compensate for the possible liquid loss. For coarse-grained soils, the FER can be larger to reduce the use of surfactant. In a typical application, the FER might be 10 to 20 (Milligan, 2000). The EFNARC (2005) recommends a FER between 5~30 in engineering application. Based on the information above, the FER was chosen to be 10, 15 and 20 (under applied pressure) in this research to study its influence on the pressure development during foam infiltration.

The bubble images were analyzed with a commercial software AmScope in order to determine the bubble size distribution curve. The bubble size distribution curves for different foams are displayed in Figure 2-4.

2.3.2 Sand

In this research, one fine sand and two medium sands were utilized to represent different sand stratum. The sands were commercial products purchased from Euroquarz GmbH (Product type: Siligran). Particle size distribution curves of the three types of sand are shown in Figure 2-4 together with the bubble size distribution curve.

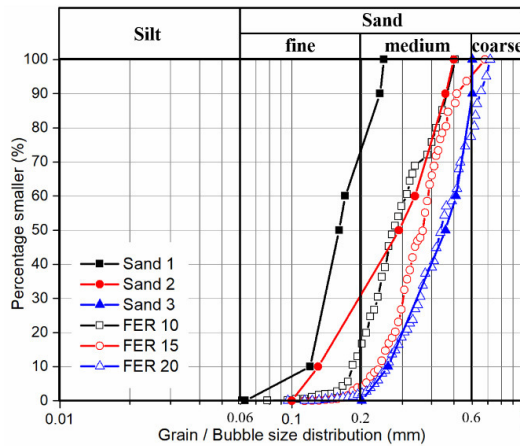


Figure 2-4. Grain / Bubble size distribution curve of the three sands / foam.

2.4 Experimental procedure

For sample preparation, sand was rained in and densified by tamping it in water environment layer by layer (Xu, 2018; Galli, 2016). This procedure assures the non-existence of unsaturated condition in the sand column. The final height of both the sand column and water as well as the weight of the used sand were recorded for the calculation of the sample parameters. Prior to the filling of foam, the permeabilities of the different sand samples were obtained by the measured pore pressures between two adjacent pressure transducers and water discharge. The parameters of the different sand columns used in this experiment are listed in Table 2-1. The remaining water on top of the sand column was carefully removed by a syringe.

Table 2-1. Parameters of the sand column

	Porosity	Relative density (%)	Permeability (m/s)
Sand 1	0.40	80	1.5×10^{-4}
Sand 2	0.41	70	5.0×10^{-4}
Sand 3	0.40	80	6.0×10^{-4}

A foam layer of 300 mm thickness was then filled on top of the sand column. An air pressure of 50 kPa was then applied and the foam will therefore be compressed. According to Boyle's Law the following relation can be obtained:

$$FER_p = \frac{p_a}{p} (FER_a - 1) + 1 \quad (2-9)$$

where FER_p is the FER at the desired air pressure, FER_a the FER at atmospheric pressure, p_a the atmospheric pressure and p the desired air pressure (total pressure: atmospheric plus excess pressure).

The foam is first produced at atmospheric pressure and then pressurized during the test at an applied pressure of 0.5 bar. Therefore, the FER at atmospheric pressure is about 1.5 times higher than the FER at applied pressure with Equation (2-9). For example, to get a foam of FER 10 at 1.5 bar, the FER should be 14.5 at atmospheric pressure.

The test started by opening the valve at the bottom (see Figure 2-1). Pore water pressures and discharged water were recorded at a time interval of 1 s. After 2 hours of testing, the valve was closed, and the air pressure was released.

In the meanwhile, foam will degenerate as time goes on. In tunneling application, this process is usually characterized by a "half-life" test. The degeneration process of foam can also influence the foam infiltration characteristics since foaming liquid could travel faster than foam bubbles. Therefore, the drainage behavior was tested using the same method that was used by Thewes and Budach (2012) but extended to 2 hours with continuous measurement every minute.

2.5 Results and discussion

2.5.1 Volume and discharge

During each test, infiltration of foam into the sand column was rather noticeable that a foam-infiltrated area distinguished itself easily from the water-saturated sand. Figure 2-5 shows that there were three sections: foam, foam-infiltrated sand and water-saturated sand. It shows that foam is infiltrating into the sand column, making the foam-infiltrated area similar to dry sand which can be easily distinguished from the original saturated sand. The interface between foam-infiltrated and water-saturated sand is apparent and it remained stable while moving further downwards during the test.

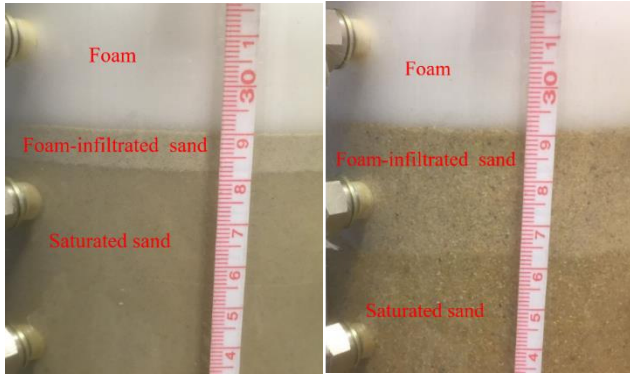


Figure 2-5. Image of the foam-sand boundary and the foam front 1 min after test (left: 1-4 Sand 1 FER 15; right: 3-1 Sand 3 FER 10).

Figure 2-5 also shows that the interface between foam-infiltrated and water-saturated sand is parallel to the foam-sand boundary, indicating that the pore water in the foam-infiltrated sand has been replaced by the foam bubbles evenly over the entire cross-sectional area of the sand column. Therefore, it is reasonable to deduce an infiltration depth (X) by foam.

$$X = \frac{V_{pw}}{n_s A_C} \quad (2-10)$$

with X the infiltration depth, V_{pw} the volume of expelled water, A_C the cross-sectional area of the large cylinder and n_s the porosity of the sand column. It should be

mentioned that the calculated infiltration depth (X) by discharged water includes the influence from the drainage behavior. Therefore, the calculated infiltration depth can be larger than the actual penetration depth by the foam bubbles. Unless otherwise stated, the infiltration depth in this thesis refers to the depth calculated using Equation (2-10).

Table 2-2. Discharged volume, Peclet number and foam spurt length in all tests.

Test no.	Sand type	FER	Discharged volume	Peclet number	L (cm)
1-1	1	10	346.4	$0.002 < Pe < 0.003$	$0 < L < 2$
1-2		10	307		$0 < L < 2$
1-3		10	380.4		$0 < L < 2$
1-4		15	290.8	$Pe = 0.004$	$4 < L < 6$
1-5		15	325.6		$0 < L < 2$
1-6		15	322.4		$4 < L < 6$
1-7		20	269.2	$Pe = 0.004$	$4 < L < 6$
1-8		20	318.2		$4 < L < 6$
1-9		20	296.4		$4 < L < 6$
2-1	2	10	571.2	$0.005 < Pe < 0.009$	$4 < L < 6$
2-2		10	499		$4 < L < 6$
2-3		10	500.4		$4 < L < 6$
2-4		15	430.6	$0.008 < Pe < 0.013$	$4 < L < 6$
2-5		15	435		$10 < L$
2-6		15	445.2		$10 < L$
2-7		20	355.2	$0.005 < Pe < 0.013$	$6 < L < 10$
2-8		20	395.6		$10 < L$
2-9		20	399.6		$10 < L$
3-1	3	10	420.8	$0.003 < Pe < 0.013$	$6 < L < 10$
3-2		10	475.6		$6 < L < 10$
3-3		10	500.8		$6 < L < 10$
3-4		15	404.8	$0.006 < Pe < 0.017$	$6 < L < 10$
3-5		15	456		$10 < L$
3-6		15	424.2		$10 < L$
3-7		20	519.4	$0.011 < Pe < 0.018$	$6 < L < 10$
3-8		20	486.4		$10 < L$
3-9		20	467.4		$10 < L$

Early results (Xu, 2018; Galli, 2016; Quebaud et al., 1998; Maidl, 1995) show that the

penetration of foam into sand is very fast at the beginning and rather slow at the following infiltration period. This has also been noticed in this research. To get a closer view on both periods, apart from the linear relation with time also the square root of time has been chosen to plot the results. Furthermore, square root of time enables the possibility to take into account the influence from consolidation behavior if it happens. The results are presented in Figure 2-6.

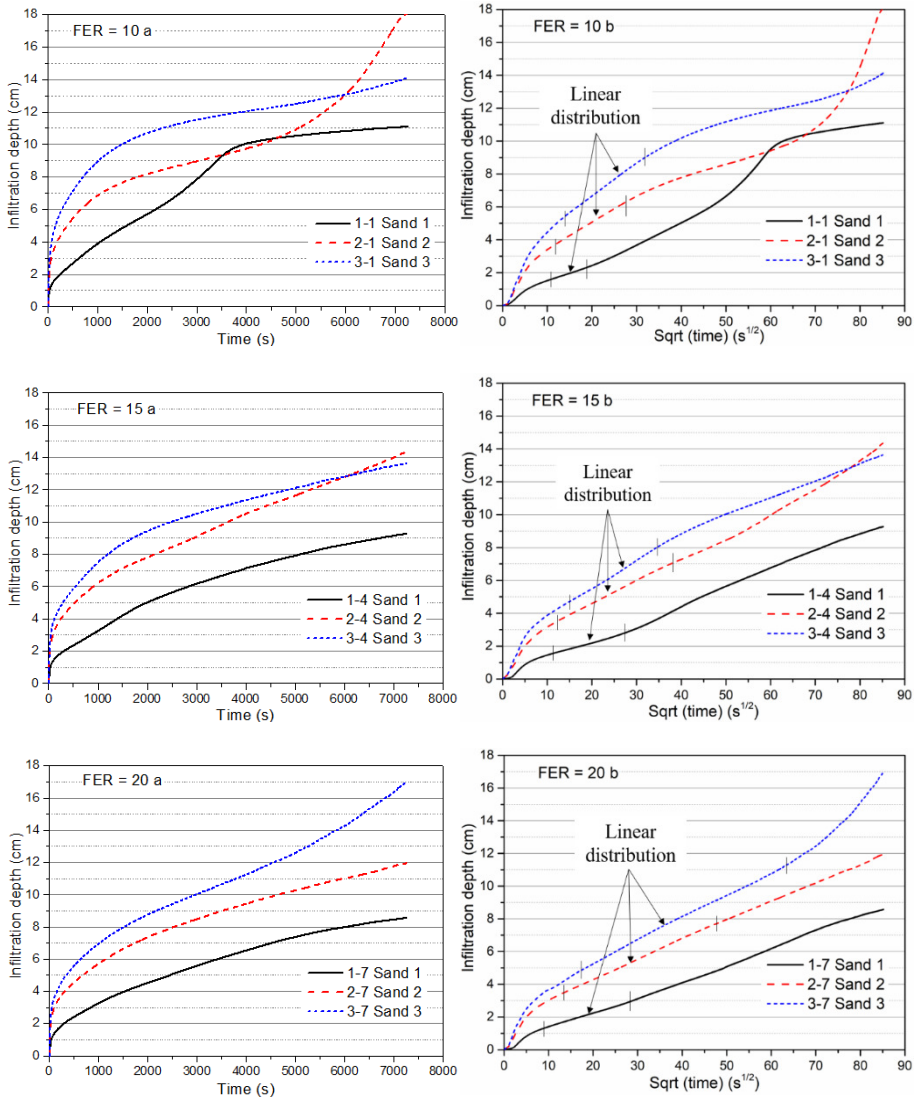
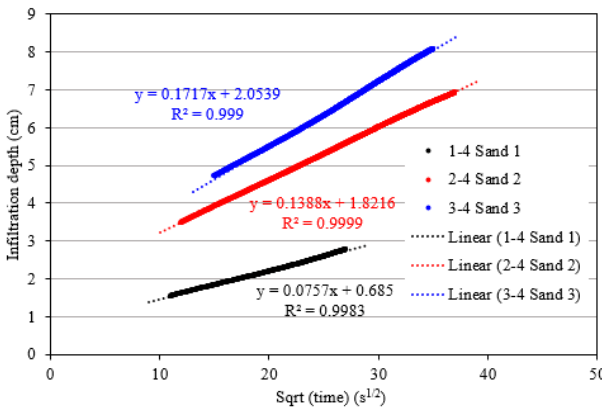
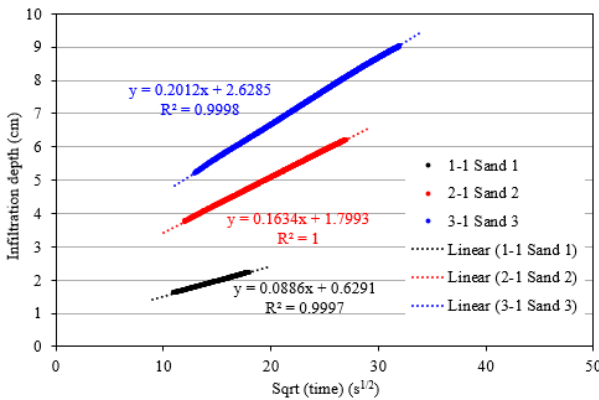


Figure 2-6. Foam infiltration against (a) time and (b) square root of time.

When plotting the foam penetration against time (Figure 2-6a), it is difficult to distinguish one period from another. After a short period of fast penetration, the increase in infiltration depth kept decreasing. Replotting the results against the square root of time enables to distinguish a linear distribution period after the initial fast penetration period (see Figure 2-6b, results of the linear fit are shown in Figure 2-7). From visual observation during the experiment, this straight-line period usually happens after the fast penetration at the beginning, suggesting that a comparable consolidation process might occur at this stage. There are some different discharge patterns after this linear distribution period for some unknown reasons as can be seen from Figure 2-6b, this chapter will only focus on the initial fast penetration period and the linear distribution period. Following results will be presented in square root of time in order to keep the analysis consistent.



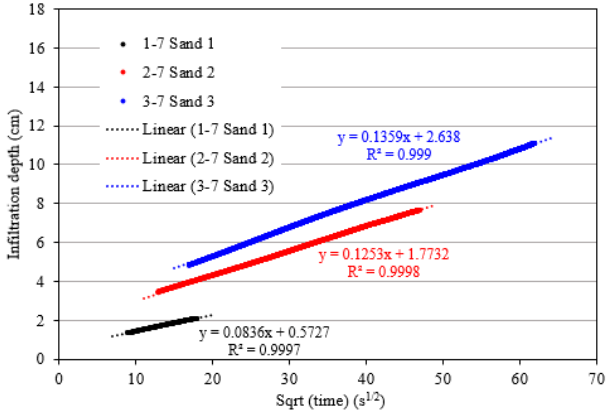


Figure 2-7. Linear fit of part of the data shown in Figure 2-6b.

The experimental results presented by Maidl (1995) show that the observed foam penetration depth is smaller than the calculated depth with expelled water. A recent study by Wu et al. (2018) shows that the drainage behavior in a foam is caused by the liquid loss among the foam bubbles. The drainage behavior in the foam should be responsible for the extra expelled water.

To further investigate the drainage behavior, it is useful to specify whether there is drainage behavior during the experiment. The theory of Peclet (Pe) for distinction between drained and undrained behavior was proposed by Winterwerp & van Kesteren (2004) and could be implemented here as a reference to the drainage behavior. It is defined by:

$$Pe = \frac{UD_c}{c_v} \quad (2-11)$$

with U the characteristic velocity, D_c the characteristic length scale and c_v the Terzaghi's consolidation coefficient, which is defined (Talmon et al., 2013):

$$c_v = \frac{k_{fw}}{\rho_w g m_v} \quad (2-12)$$

with k_{fw} the permeability of foam (m/s), ρ_w the density of water and m_v the compressibility (1/Pa).

Drainage behavior occurs when $Pe < 1$. The foam exhibits undrained behavior when Pe is greater than 10.

The permeability of foam to water (k_{fw}) was calculated with the measurement data from the foam drainage test and ranges between 3×10^{-8} m/s and 3×10^{-6} m/s (Thewes et al., 2012). For the foam with a FER of 15 (93% of air), the compressibility under 150 kPa (50 kPa above the atmospheric pressure) is around 1.24×10^{-5} (1/Pa). Then the resulting consolidation coefficient will be in a range of $2.4 \times 10^{-7} < c_v < 2.4 \times 10^{-5}$ m²/s.

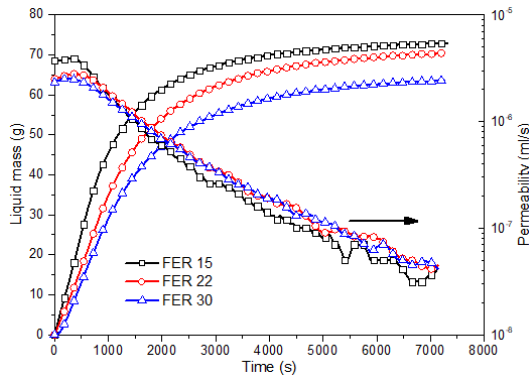


Figure 2-8. Results from foam drainage tests and the calculated permeability.

In the foam drainage tests, 80 g of each foam was put in the filter funnel and the drainage liquid was recorded. The test was carried out at atmospheric pressure, so the FER of the foam is approximately 1.5 times the value of the foam used in the foam infiltration test (which is under 1.5 kPa of absolute pressure). The measurement results are shown in Figure 2-8. It shows that the half-life of the foam (time for 40 g of drained liquid) increases with increasing FER. The total drained liquid decreases with increasing FER. It should be mentioned that the drainage of liquid leads to the rupture of the bubbles. Small bubbles have a higher internal pressure than larger bubbles and therefore are included in the larger bubbles.

With the diameter 13 cm of the filter funnel, the hydraulic gradient 1 in the foam during the test, the permeability of the foam can be obtained with the measured liquid mass. The calculated permeabilities are shown in Figure 2-8. The permeability of FER 15 is almost 2 times larger than that of FER 22 and FER 30 in the beginning until 500 s. After around 1000 s, the permeability of FER 15 became the smallest as can be seen in the figure. The results suggest that the foam with a smaller FER may not be stable compared with a larger FER, because its ability to retain the liquid among the bubbles

is relatively poor.

From the foam penetration test the characteristic velocity of the foam (U) can be calculated by

$$U = \frac{Q}{nA_C} \quad (2-13)$$

with Q the discharge, which was smoothed with a moving average of 15 in these tests.

The characteristic length (D_c) of the foam should be the diameter of the foam bubbles. Here d_{10} (0.18 mm, 0.24 mm and 0.26 mm for FER of 10, 15 and 20, respectively) was taken as the characteristic size for each foam.

The Peclet number indicates that when $Pe < 1$, the mixture will exhibit drainage behavior. From the calculated Peclet number (Table 2-2) it is concluded that the foam exhibits drainage behavior during the experiments. This is in line with the experimental results presented above.

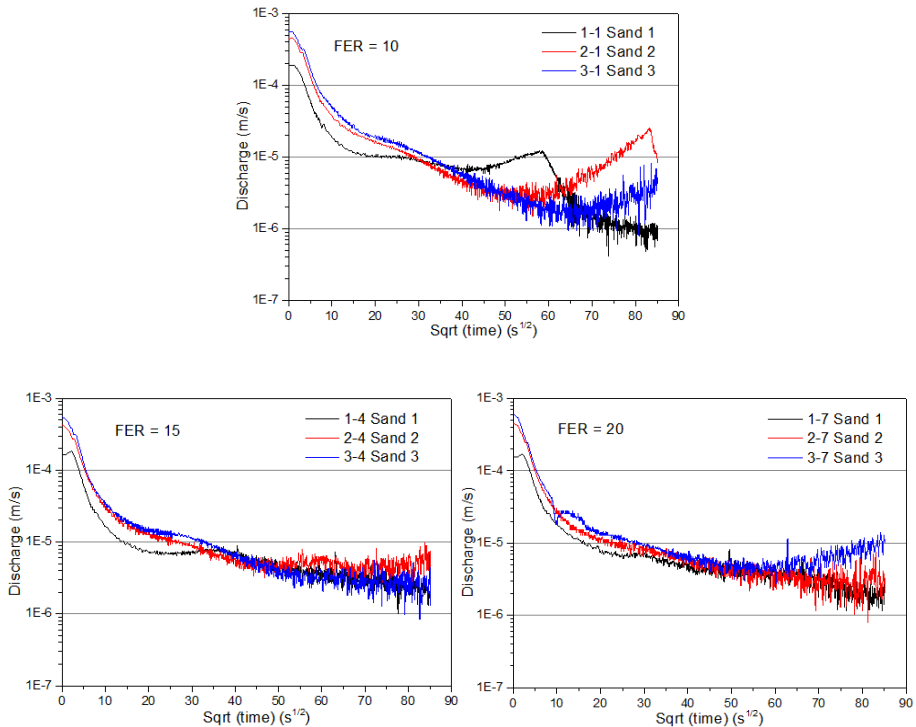


Figure 2-9. Specific discharge against square root of time

Figure 2-9 shows the calculated specific discharge against the square root of time in tests with different FERs for the three types of sand. For the results with sand 1, the Darcy velocities at the beginning of the test in different FERs are almost the same at about 1.5×10^{-4} m/s. It is mentioned that the hydraulic gradient in the set-up is 1 with an excess pressure of 50 kPa. Therefore, the Darcy velocity at the beginning of the test (when no foam has yet infiltrated into sand) should be more or less the same to the water permeability of the sand column. This is demonstrated by the test series with sand 2 and sand 3, in which the specific discharge at the beginning of the test is 4.5×10^{-4} m/s and 5.5×10^{-4} m/s, respectively.

The specific discharge of all the tests quickly decreased by one order of magnitude at about 100 seconds ($10 \text{ s}^{1/2}$). After 100 seconds, the decrease in discharge started to slow down. But the test with FER of 10 presents a bigger value than with FER of 15 or 20 after the sharp decrease. We attribute this to the larger amount of water loss from the foam with FER of 10 than that of 15 or 20.

All test results show a small increase in specific discharge at some point, after which it dropped to an even smaller value. It should be noted that the specific discharge with FER of 10 gives a smaller value at 1×10^{-6} m/s, while the other two give the value at about 2×10^{-6} m/s, showing a decrease by two orders of magnitude in the overall permeability.

As for sand 2, the results show some similar trend to those of sand 1. At the very beginning of the test, the Darcy velocities are more or less the same to the water permeability of the sand column, 5×10^{-4} m/s. They quickly decreased by one order of magnitude at about 100 seconds and similar to the tests with sand 1, the test with FER of 10 results in a higher permeability than the tests with FER of 15 or 20 right after the sharp decrease. In the test with FER of 10, the specific discharge presents an increase that goes from 3×10^{-6} m/s up to 2×10^{-5} m/s. Followed by a sharp decrease that within 2 hours of test had not yet reached a minimum value. Upon the end of the test, a decrease by two orders of magnitude in the overall permeability is reached.

The results from sand 3 are in general similar to those of sand 2. Except for test with FER of 10, in which the specific discharge presents an increase at the end of the test

while no decrease follows afterwards. The test with FER of 20 also presents an increase near the end of the testing period. The increase in the specific discharge could be caused by the deterioration of the foam bubbles in the foam infiltrated sand (Xu, 2018). The overall permeability was decreased by two orders of magnitude at the end of the test for all the tests.

One important knowledge revealed in this section is that the drainage behavior is not separate from the period of foam spurt. Drainage behavior could happen even during the foam spurt period. Here in this research, the period of foam spurt is defined as the condition in which most of the foam bubbles near the foam front could travel further into deeper sand. It should be noted that the foaming liquid in the foam could be faster than the foam bubbles, resulting in the drainage behavior of foam but not necessarily mean the stoppage of the foam spurt period.

2.5.2 Pore water pressures

One of the major objectives in this research is to investigate the pore water pressure development during foam infiltration. The modified pressure transducers were installed at different locations below the sand level in order to monitor the changes in pore water pressure during the experiment. It is also interesting to investigate how the pore water pressure inside the foam infiltrated sand develops during the experiment. However, as presented in the section above, Equation (2-11) indicates that a lower infiltration velocity will result in a smaller Peclet number and thus more prone to drainage behavior. To avoid the influence from the additional drained water on the analysis, the results from Sand 3 FER 10 were analyzed to get a general understanding. The measured pore water pressures were plotted against the square root time. Figure 2-6 shows the infiltration depth could reach nearly 14 cm, indicating that the foam front has passed all the pressure transducers located in different depths. As a result, the pressures were also plotted as a function of the infiltration depth.

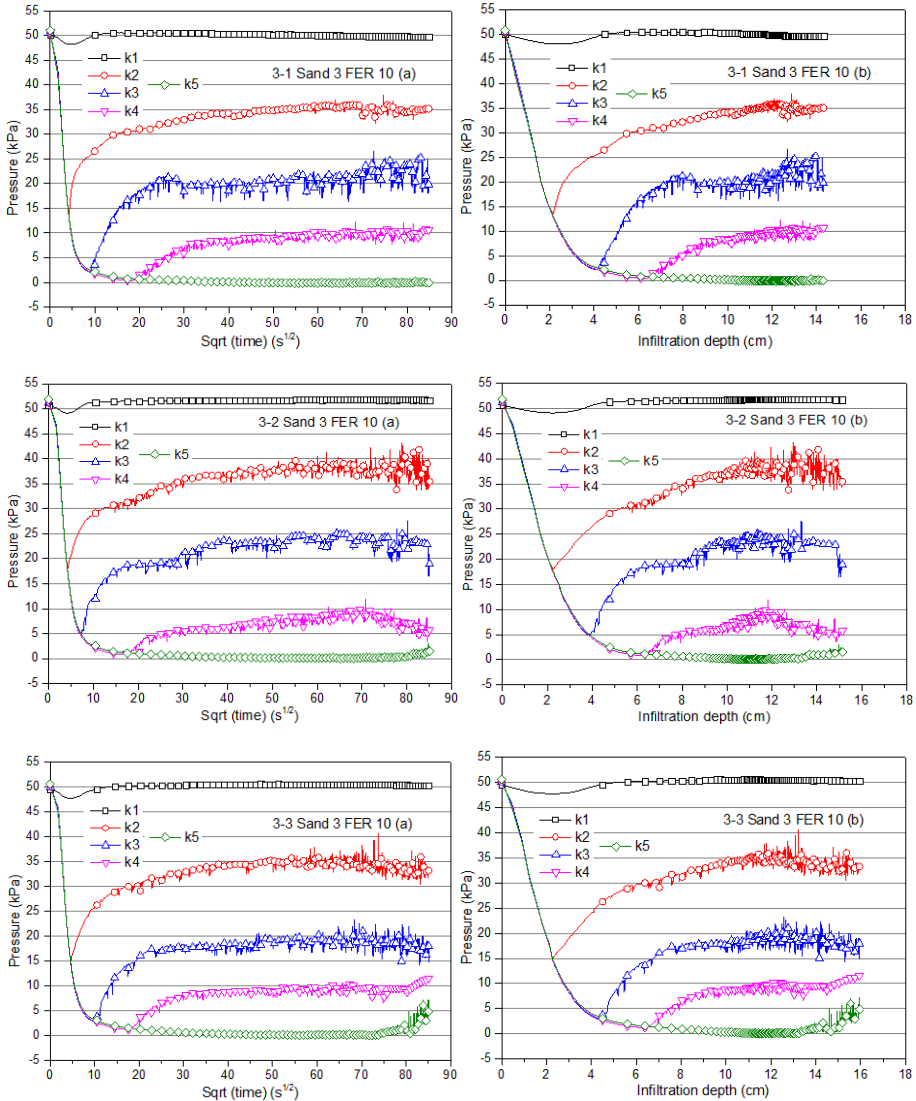


Figure 2-10. Pore water pressure distribution curve in tests with Sand 3 FER 10. The pressures were plotted against both square root of time (a) and infiltration depth (b)

Figure 2-10 shows the measured pore water pressures against both square root of time (Figure 2-10a) and infiltration depth (Figure 2-10b) in tests with Sand 3 FER 10. Upon the start of the test, the pressures at different locations were more or less the same. After the test started, the pore pressures in the sand quickly decreased with foam infiltration.

As indicated by Figure 2-2, most of the drop in piezometric head is in the small cylinder which takes 4.5 m of 5 m. During steady flow without foam infiltration, the pore pressures measured by $k_2 \sim k_5$ should stay relatively high at around 50 kPa. However, due to foam infiltration in the test as shown in Figure 2-5, the flow resistance in the foam infiltrated area increases and the drop in piezometric head is now concentrated in the foam infiltrated area. The measured pore pressures in the saturated sand below the foam infiltrated area decreases fast as a consequence. At the end of the test, k_5 is nearly 0 as it is barely influenced by foam infiltration, indicating that most of the piezometric head is taken by the foam infiltrated area while the drop in piezometric head in the saturated sand is negligible. The fast dissipation of the pore water pressures in the sand column suggests that the excess pore pressures were being transferred to the soil skeleton.

Shortly after the foam front passed k_2 , it started to increase (Figure 2-10b), while k_3 , k_4 and k_5 continued to decrease. The contrast in the pressure development at this infiltration depth indicates that the foam infiltrated area has a strong influence over the pore pressure distribution. As the foam front traveled even deeper, k_2 got even higher, but with a slower increase. Similar to k_2 , at the infiltration depth of about 4 cm and 6.5 cm, k_3 and k_4 also started to increase, respectively.

With more infiltration time, k_5 continued to drop to smaller values. Figure 2-10a shows that after about 400 seconds, the pore pressure in the original sand (k_5 , 10 cm below the sand level) almost reached steady values, while k_2 , k_3 and k_4 continued to increase.

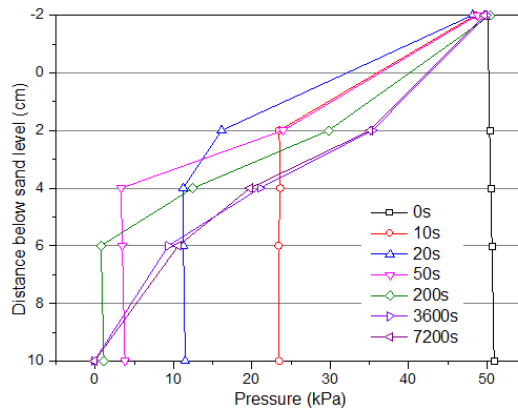


Figure 2-11. Pore water pressure distribution at different times as a function of location 3-1 Sand 3 FER 10.

Figure 2-11 shows the measured pore water pressure as a function of depth at different times. Prior to the start of the test, the pore water pressure increases with depth because they are hydrostatic pressures. When the test started, flow resistance in the upper part of the sand column increased due to foam infiltration and the excess pore water pressure in the sand column dissipated fast. At 10 seconds, the pore water pressures in the sand column were more or less the same, but with a smaller value than that in foam. After 20 seconds, the pore water pressure at 2 cm below the sand level shows a higher value than at 4 cm, 6 cm and 10 cm, indicating that the foam front has passed k2. This is confirmed that as time went on, the distribution of pore water pressure at the depth of 4 cm, 6 cm and 10 cm continued to drop, while at 2 cm, the pore water pressure showed some increasing trend. Similar development in pore water pressure happened at the depth of 4 cm and 6 cm later on.

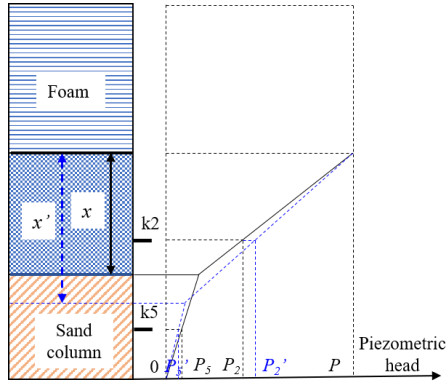
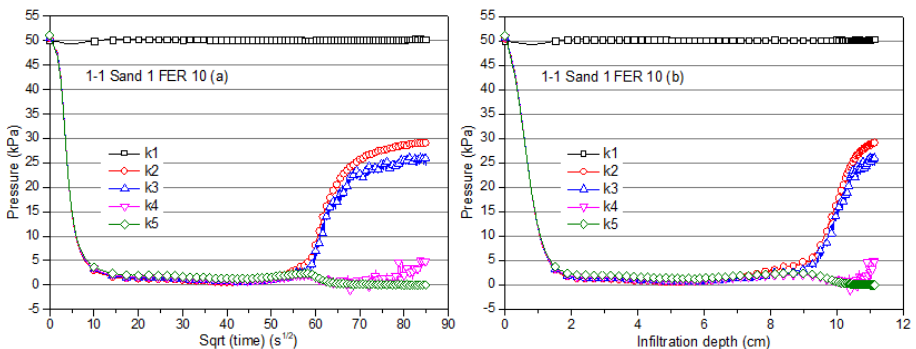


Figure 2-12. Change in piezometric head in foam infiltrated sand and saturated sand.

A schematic view over the change in piezometric head in both foam infiltrated sand (measured by k_2) and saturated sand (measured by k_5) is shown in Figure 2-12. The upper part is pure foam, and the foam has penetrated in the blue dotted area and below that it is still saturated sand. In the diagram the foam front settles further to deeper sand (from x to x'), k_2 changes from P_2 to P_2' , and k_5 changes from P_5 to P_5' during this process.

Assume there is a linear distribution of pore water pressure over the foam infiltrated sand, which seems a reasonable assumption, from the measurement results shown in Figure 2-11. A pressure increase in k_2 is expected when the foam front passes k_2 and infiltrates further into the sand. While the decreasing trend in saturated sand (as indicated by k_5 in Figure 2-12) corresponds with the measurement results as shown in Figure 2-10. The increase in k_2 , k_3 and k_4 illustrates that the foam front has passed 2 cm, 4cm and 6 cm, respectively, see Figure 2-10b.



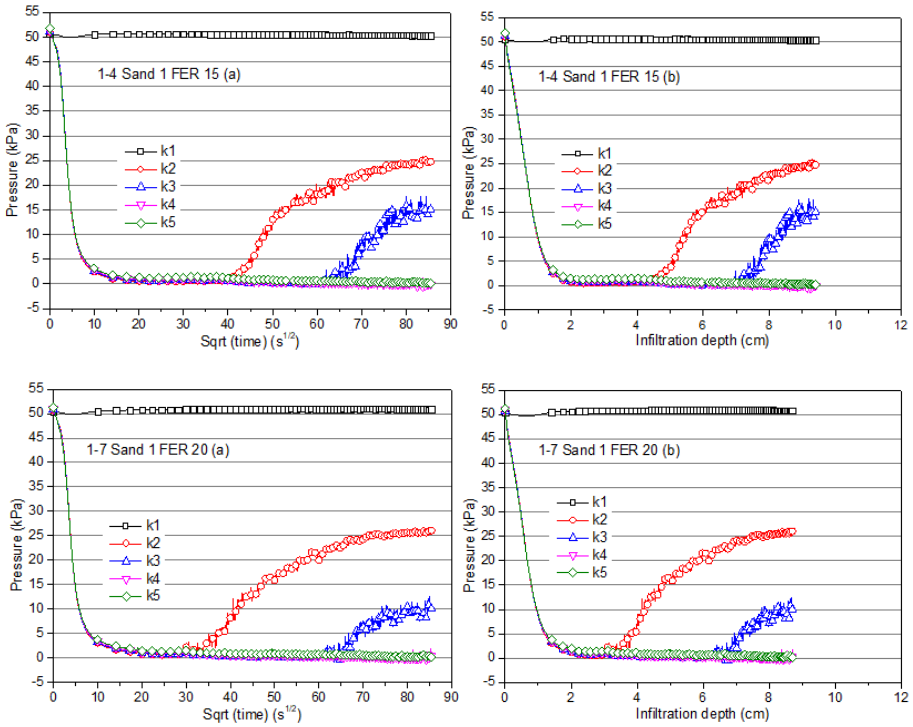


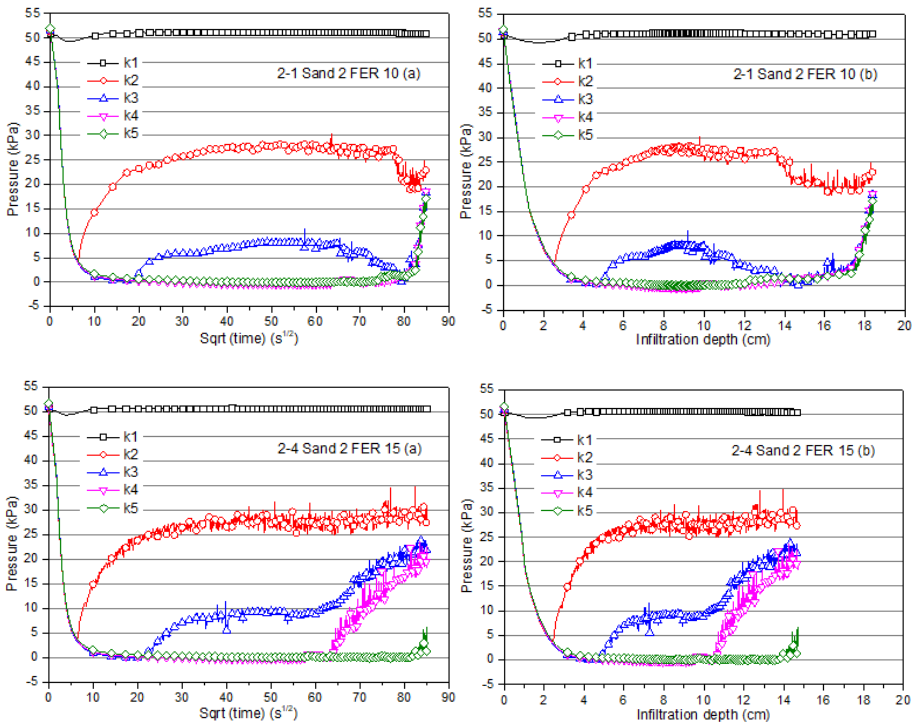
Figure 2-13. Pore water pressure distribution curve in test with Sand 1. The pore pressures were plotted against both square root time (a) and infiltration depth (b)

Figure 2-13 shows the measured pore water pressures against both the square root of time (Figure 2-13a) and the infiltration depth (Figure 2-13b) in tests with Sand 1. According to the conclusion presented above, the pore water pressures will increase when the foam front passes the pressure transducers. However, there are differences regarding the pressure development when foam bubbles pass the pressure transducer in the experiments with different FERs.

In the test with FER of 15 and 20, k2 showed an immediate sharp increase as the foam front passed it. This increase continued as foam infiltrates further into the sand column, but later with a slower trend. While in the test with FER 10, k2 increased only slightly for a time period after the foam front passed. It seems that k3 also started to increase slightly at some point but remained smaller than k2. After a while, the increase in k2 and k3 became rather ‘steep’. Shortly after the sharp increase in k2 and k3, k4 started to fluctuate while k5 remained stable. This indicates that the foam front has passed k4.

While k_4 also increased slightly, similar to k_2 and k_3 when the foam front passed them, respectively. During 2 hours of testing, the sharp increase in pressure was not observed in k_4 as k_2 and k_3 . The slight increase was also observed in test with FER 15 and 20, but it happened in k_4 , while no sharp increase followed during the test duration of 2 hours.

Figure 2-13 shows that the maximum calculated infiltration depth increases as the FER decreases, indicating that less pore water will be expelled during the test duration when foam is drier. While there were no pressure fluctuations in k_5 in the tests with Sand 1, even the calculated infiltration depth surpasses 10 cm. This essentially suggests that the foam front has not yet reached k_5 (10 cm below the sand level), corresponding to the early conclusion that drainage behavior during the experiment resulted in more water expelled than the actual foam bubble penetration depth.



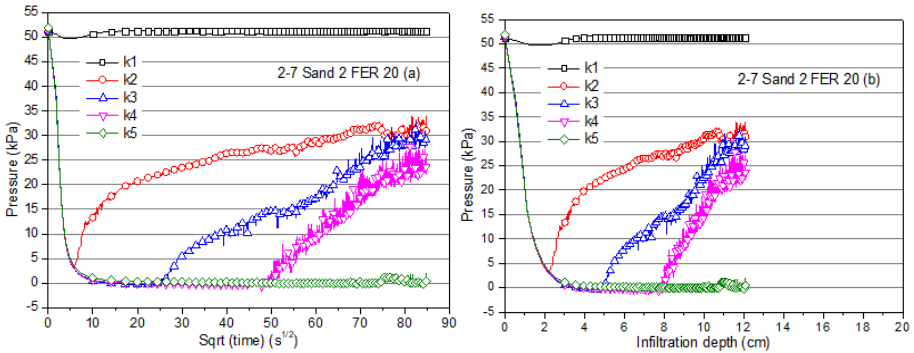


Figure 2-14. Pore water pressure distribution curves in test with Sand 2. The pore pressures were plotted against both square root time (a) and infiltration depth (b)

Figure 2-14 shows the results from tests with Sand 2. A notable difference compared with the results from Sand 1 comes from the pressure development of k2 and k3 in test with FER 10. In the test with Sand 1 FER 10 (Figure 2-14), k2 and k3 only increased slightly after the foam front passed and the sharp increase appeared after a certain time period. While in the test with Sand 2, k2 and k3 immediately increased sharply after the foam front passed them separately. However, a similar situation happened to k4 in case of Sand 2 when comparing to k2 and k3 in Sand 1. That k4 in test with FER 10 only increased slightly as the foam front passed. While for the tests with FER 15 and 20 (Figure 2-14), the sharp increase in pressure almost happened immediately in k4 after the foam front passed it. There is also the slight increase in pressures measured by k5, though it happened near the end of the test and, probably because the testing time was not long enough, no sharp increase followed up. It should be mentioned that the sharp increase in pressure was observed almost at the same time in k3 and k4 at the end of the test with Sand 2 and FER 10. This is similar to what is observed in test with Sand 1 FER 10. The reason remains unclear upon the finish of this chapter.

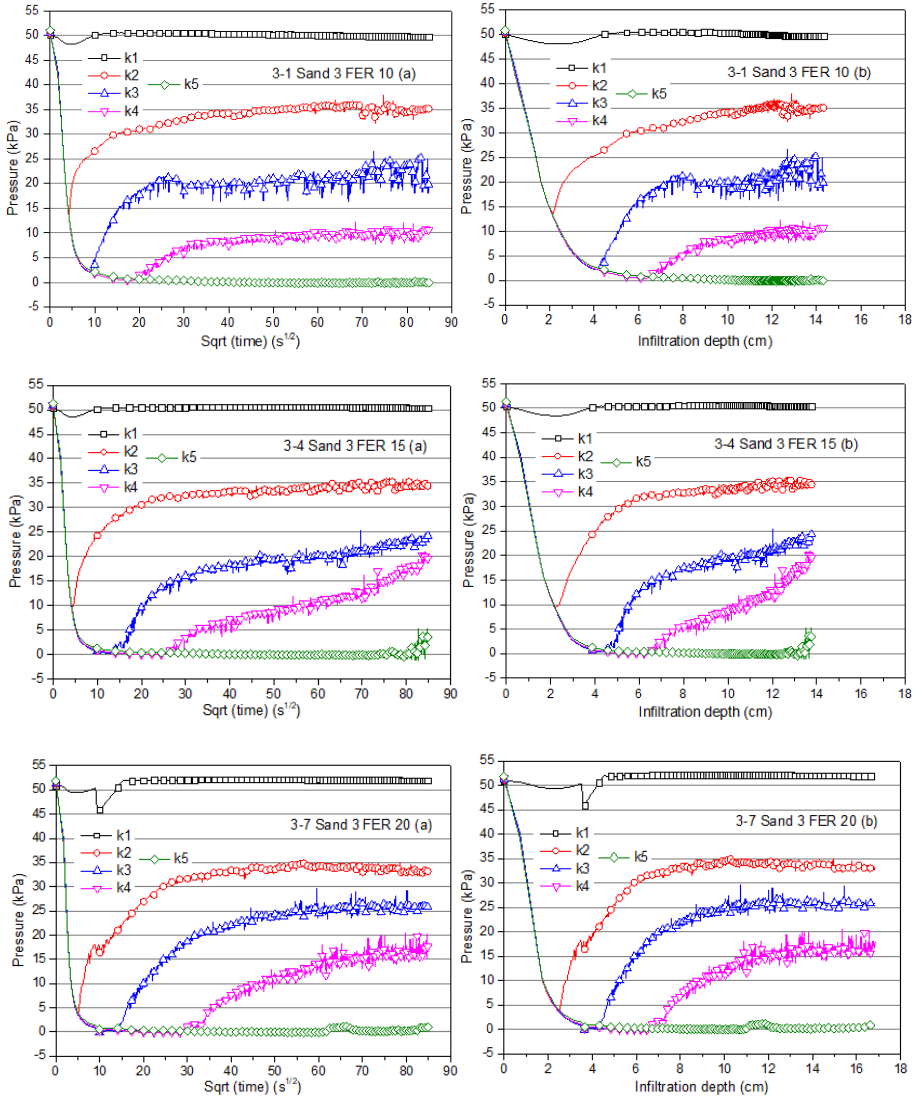


Figure 2-15. Pore water pressure distribution curve in test with Sand 3. The pore pressures were plotted against both square root time (a) and infiltration depth (b)

As for the results from Sand 3, Figure 2-15 shows that a sharp increase in pressure was observed as foam front passed k2 and later k3 and k4 in tests with all the different FERs. In the test with FER 10, although the calculated infiltration depth is 14 cm, more than 10 cm, hardly any pressure increase was observed in k5. This suggests that the foam bubble front has not passed k5. In the tests with FER 15 and 20, however,

the pressure measured by k5 presents some slight increase, indicating that the foam front has passed k5. It should be mentioned that the calculated maximum infiltration depth in test with Sand 3 FER 20 is the largest in Figure 2-15, which is not following the conclusion in tests with Sand 1 and Sand 2. It seems the increase in discharge after the linear line against square root time (Figure 2-6b) is responsible for the largest infiltration depth in the tests with Sand 3. Because the focus of this study is the initial fast penetration period and the linear distribution period that follows, the increase in discharge after the linear line is not studied in detail.

From the measured pore water pressures presented in this section, it is evident that the infiltration of foam bubbles will cause a decrease in the permeability of the sand, thus increasing the local hydraulic gradient that is required to ensure the micro stability. This is confirmed by the measured pore water pressure. When the foam front passed the pressure transducer, there is in most cases a sharp increase in pressure, indicating that the local hydraulic gradient in the foam infiltrated area was considerably enlarged. Specifically, the hydraulic gradient over the sand layer between k1 and k2 is more than 7 as can be found from Figure 2-11, suggesting that micro stability at the tunnel face can be assured.

Apart from the observed sharp increase in pressure due to the passing of foam front, another phase of slight increase is present in some test results. The slight increase in pressure suggests that the increase in local hydraulic gradient is limited because the local permeability is only slightly decreased. In this phase, the foam front seems to pass rather slowly, and very likely only part of the small foam bubbles could migrate into the deep sand. Less foam bubbles among the sand grains only induce limited reduction in its permeability and thus the increase in local hydraulic gradient is rather small. This resulted in a slight increase in the pore water pressure when the foam front passed.

As it is pointed out by Xu (2018), the foam spurt defines the stage when foam bubbles are quickly entering the sand pores. The foam spurt period is followed by the permeability reduction, during which foam bubbles will be blocked and entrapped among the sand grains. The dominating flow in this stage will be the drainage of the foaming liquid, which is similar to the foam aging process (Wu et al. 2018, Koehler

et al. 2004, Magrabi et al. 1999).

However, this research shows that the foam spurt period is followed by a type of further infiltration during which the foam bubbles still migrate further into the sand. During the further infiltration period, only a small proportion of the foam bubbles at the foam front will be able to travel further. These small bubbles will decrease the permeability of the sand to some extent.

Based on the analysis, the foam spurt period can be redefined as follows:

The foam bubbles are infiltrating into the sand evenly over the cross-sectional area because most of the bubbles at the foam front can travel further into the sand. They will simply deform when the foam bubble is larger than the pore. The foam bubbles replace most of the pore water among the sand grains and thus decrease the water permeability to a large extent. The pore water pressure inside this foam infiltrated area distributes almost linearly since the 'density' of foam bubbles on the cross-sectional area along the infiltration path is more or less constant. There is an end to the foam spurt period, when most of the foam bubbles are blocked by the sand grains and the pressure gradient is not high enough anymore to deform the bubbles. After that only a small proportion of the foam bubbles can further infiltrate deeper into the sand, leading to a limited influence on the water permeability of the sand.

Followed by the definition of foam spurt, the foam spurt length (L) for each test can be obtained from the measured pore water pressures. Results are also included in Table 2-2.

Table 2-2 shows that the foam spurt length is influenced by both sand type and FER. It increases with increasing grain size of the sand because normally the pore size will be bigger with larger sand grains. Movement among large pore size will be easier compared with that among smaller pore size. The foam spurt length also increases with increasing FER, although this is not obvious in the tests with Sand 3.

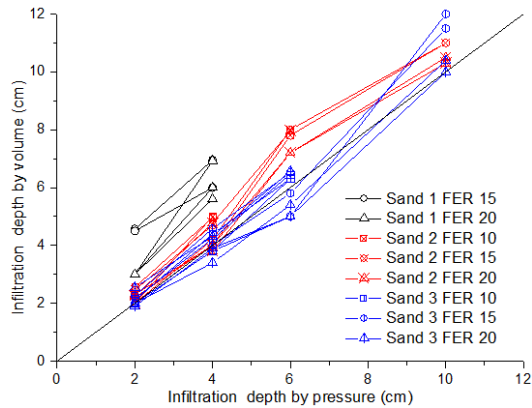


Figure 2-16. Comparison between infiltration depth determined by measured pressure and volume.

Figure 2-16 shows the comparison between the infiltration depth by the measured pore pressures and the discharged water. In general, the infiltration depth by pressure is smaller than that by discharged water in Sand 1 and Sand 2. With an increase in grain size, the deviations between these two values are smaller, suggesting the drainage behavior may not be a significant phenomenon in coarse-grained soils. The deviations between the two values in Sand 3 are not so clear with different FER as can be seen in Figure 2-16.

For Sand 3 there is a certain amount of part that the infiltration depth by pressure is larger than by discharged water. This could be caused by the fact that the bubbles could only display part of the pore water among the sand grains. As shown in Figure 2-4, most of the foam bubbles are smaller than Sand 3, which could explain the situation here. The drainage volume from the foam in this case could not compensate for the pore water that is not expelled by the foam bubbles. The infiltration depth by pressure is larger than by discharged water as a consequence.

The results from this section show that the pore pressure inside the foam infiltrated sand is much larger than that in the saturated sand ahead of the foam front, suggesting that the foam infiltrated sand functions similarly like an internal cake in case of a slurry infiltration. Large pressure drop can be realized over the first few centimeters of soils even during the foam spurt period. After foam spurt, further infiltration was found to be the main process in which foam bubbles infiltrate further into the sand at

a much lower speed while the foaming liquid around the foam bubbles travel faster than the foam bubbles. This has been indicated by the development of pore water pressures at the moment when foam front passed the pressure transducers.

2.6 Verification test

A typical pattern of the consolidation process in a slurry infiltration test is that the permeability is determined by the filter cake, and the properties of the filter cake are only determined by the slurry properties and the applied pressure. Changing the sand will not necessarily have any influence on the permeability of that filter cake as long as there is a filter cake formed. Thus, the slope of the discharged water during filter cake formation should not be influenced by the type of sand medium. However, Figure 2-6 shows that when infiltrating with foam during the linear part there is an influence of the sand. The slope of the linear line becomes bigger when the sand gets coarser, suggesting that this period has a relation to the sand type. This is contrary to the filter cake formation process for slurry infiltration since the permeability is clearly not determined by the foam on top of the sand when varying the sand types while keeping the foam with the same FER (see Figure 2-6).

This suggests that although with a similar discharge pattern, the dominating flow at this linear part may not be the consolidation process in the foam above the sand itself but the foam bubble infiltration. The first consolidation process refers to the process during which water drains from foam above the sand, resulting in a drier foam and eventually reduces permeability while in the latter the foam bubble infiltration results in a foam-sand mixture with a lower permeability. The major objective of this verification test is to determine which process is dominating by comparing the permeability of these two parts. Since the permeability will be determined by the layer with the lowest permeability, the pressure difference will be the largest over that layer. Therefore, in these tests it is measured which part has the largest pressure difference on the whole system. Two additional tests were conducted with altered locations of the pressure transducers. The tests were performed with Sand 1 and Sand 2, both with foam at FER 20. The set-up remains the same with the exception of the pressure transducers' locations. Two pressure transducers were reallocated to be located above

the sand level to measure the pore pressures inside the foam and the other two were below the sand level. The distance between adjacent transducers is 4 cm as can be seen in Figure 2-17.

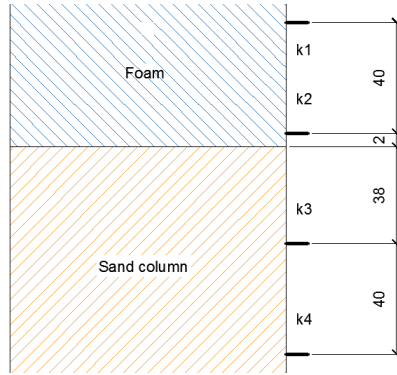


Figure 2-17. Distribution of the pressure transducers in additional tests (unit: mm).

Figure 2-6 also indicates that the linear distribution part after the fast penetration stage could last as long as the test is going on. The focus of these two additional tests was to investigate the infiltration behavior after the initial fast penetration period. Therefore, the duration of these two additional tests was one hour instead of two.

The measured pore pressures as well as the calculated infiltration depth are presented in Figure 2-18. It can be seen that the overall development shows similar patterns with those presented earlier in this chapter. The excess pore pressures in the sand dissipate quickly during the initial fast penetration period after which there is a linear distribution of the discharged volume against the square root of time.

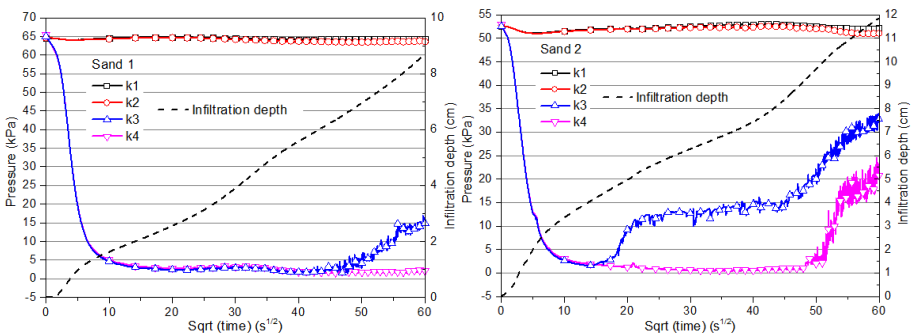


Figure 2-18. Measured pressures and calculated infiltration depth against square root of time for Sand 1 (a) and Sand 2 (b).

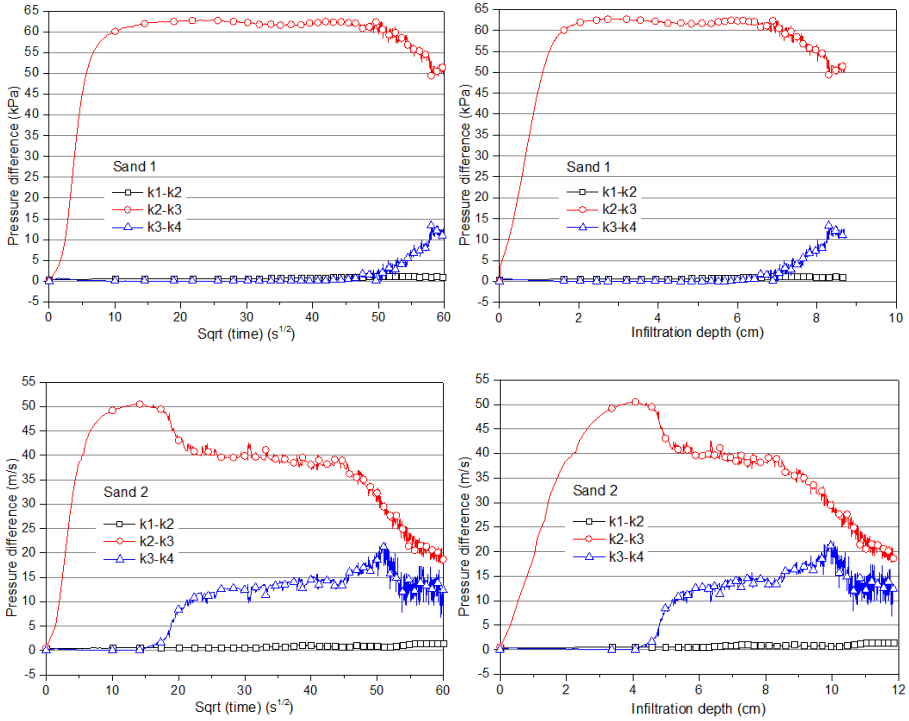


Figure 2-19. Pressure difference between pressure transducers against square root of time and infiltration depth for Sand 1 and Sand 2.

Figure 2-19 shows the pressure difference between adjacent pressure transducers as a function of the square root of time and also as a function of the calculated infiltration depth. It shows that the pressure difference in the sand near the sand level (k2-k3) increases sharply while there is hardly any pressure difference building up in foam (k1-k2) or original sand (k3-k4) during the foam spurt period. And this pressure difference is maintained mainly in k2-k3 after the initial fast penetration period with foam bubbles infiltrating further into the sand. Although k2-k3 will be influenced by foam since there is 2 mm of foam layer between k2 and the sand level, it is reasonable to assume that this influence can be negligible since there is hardly any pressure difference as shown by k1-k2. There is some increment in k3-k4 after the foam front passes k3, indicating that the foam infiltrated area has a strong influence on the pressure drop in the whole system. The results from Sand 2 show a similar pattern that hardly any pressure difference exists in foam, suggesting the pressure drop is

primarily maintained in the foam infiltrated sand.

The results from the verification tests show that the permeability of the whole system during the test is determined by the foam infiltrated sand instead of the foam on top of the sand. This explains the finding that the slope of the linear distribution varies with different sand types. That the permeability of the foam infiltrated sand is influenced by the grain size of the sand when mixed with the same foam.

2.7 Field measurements

The finding in this chapter could help better understand the mechanism of pressure transfer in an EPB shield during standstill. The excess pore water pressure is mainly consumed in the foam infiltrated soils for high permeable ground conditions. Because the permeability of the foam infiltrated sand will be significantly lowered compared to the permeability of the sand without foam. It could explain the measurement of the Botlek Rail Tunnel where an EPB shield was used for excavation. The pressure in the excavation chamber and at the tunnel face were measured in the project. As shown in Figure 2-20, a considerable part was bored through Pleistocene sand under a highwater table. The Pleistocene sand has a d_{50} ranging from 200 to 700 μm and the permeability is around 3×10^{-4} m/s (Bezuijen & Talmon, 2014). More information regarding the site and geology of the tunnel construction can be found in Maidl (1999).

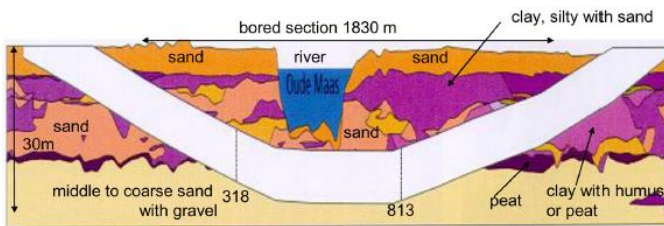


Figure 2-20. Geological profile of the Botlek Rail Tunnel (after Bezuijen & Talmon, 2014).

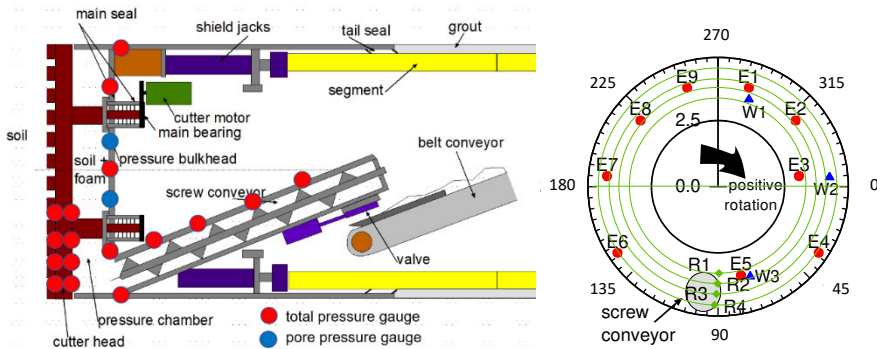


Figure 2-21. Instrumentation of the EPB shield (left). Positions of the total and pore pressure transducers in the TBM (E and W respectively) and on the cutting wheel (R) looking from the tunnel to the TBM and definition of rotation (right). See further text (Bezuijen & Talmon, 2014).

The instrumentation is shown in Figure 2-21. The instruments E1 until E9 measured the total pressure and W1 until W3 the water pressure at the pressure bulkhead. R1 until R4 are pairs of total pressure transducers on the cutter wheel, with two at each location, one measuring at the front (f) and one measuring at the back (b) of the cutter wheel in the pressure chamber. The green circles indicate the course of the instruments during drilling when the cutter wheel is rotating. The radii of these circles are from the smallest (R1) to the largest (R4) 3.25, 3.584, 4.044 and 4.442 m respectively. For more details on the measurements it is referred to Bezuijen & Talmon (2014).

The measurement results during standstill after drilling for ring 622 were plotted in Figure 2-22. During the standstill, the pressure transducers are located at a lower position below the tunnel axis as shown on top right of the figure. R2 f and R2 b had a comparable position to E5. R2 f denotes the pressure measured at the front and R2 b the pressure at the back of the cutting wheel. All the measured pressures present a decreasing trend during standstill due to the ongoing groundwater flow from the excavation chamber to the soil.

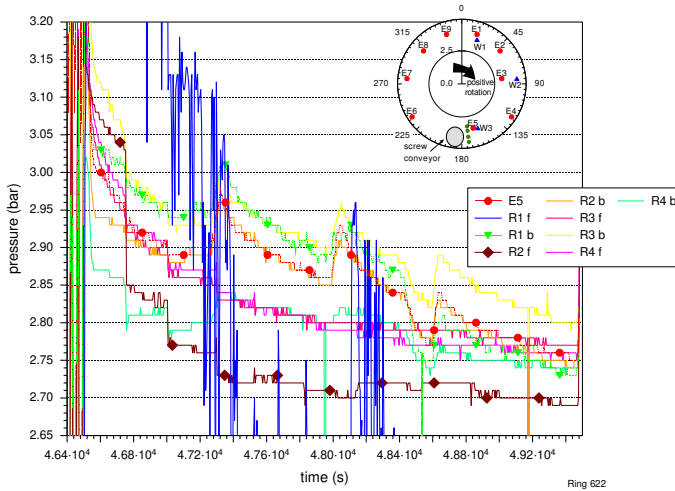


Figure 2-22. Ring 622. Pressures during stand still measured at the cutting wheel and the pressure bulkhead. Position pore pressure transducers on cutting wheel indicated with green dots.

The plot shows the pressure in front of the cutting wheel (R2 f) decreased sharply at the beginning of the standstill. While the pressure at the back side of the cutting wheel (R2 b) only reduces at a slower rate. Since there is hardly any effective stress in the excavation chamber, R2 b should be the pore water pressure in the excavation chamber as appeared from the measurements. The difference in the pressures at the back (R2 b) and the front side (R2 f) of the cutting wheel shows there is some influence from foam infiltration. Similar conditions apply to the pressures measured by R3 f and R3 b.

The development of the pressures on both sides of the cutting wheel can be comparable to the situation in the foam infiltration test. That the pressure at the back side of the cutting wheel corresponds to that in the foam-sand mixture, while the pressure in front of the cutting wheel is comparable to that in the original sand. During standstill, the pressure of the foam-soil-mixture in the excavation chamber will slowly decrease due to groundwater flow to the surrounding soil (Bezuijen & Dias, 2017), while the pressure in the soil ahead of the tunnel face will decrease at a faster rate due to the low permeability of the foam infiltrated sand at the invert of the TBM.

For some unknown reason, the development of the pressures measured by R4 f and R4

b shows some differences to R2 and R3. R4 b decreases largely in the beginning but later remains similar to R4 f, which might be influenced by the development of effective stress in the mixture. R1 f presents considerable fluctuations. The course of R1 f, also during drilling, gives the impression that this gauge was not working properly.

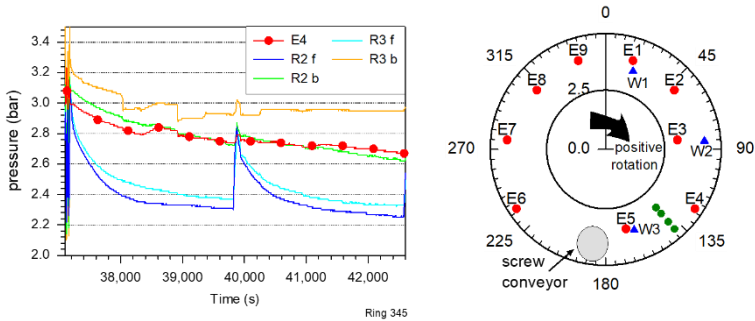


Figure 2-23. Ring 345. Pressures during stand still measured at the cutting wheel and the pressure bulkhead. Position pore pressure transducers on cutting wheel indicated with green dots.

For ring 345, the pressure transducers on the back and the front of the cutting wheel are in an upper position but still below the tunnel axis (see Figure 2-23). From measurement results, R3 b is always larger than R2 b due to the hydrostatic pressure in the lower position. Same is the case for R3 f and R2 f. The pressures in the foam-soil-mixture (back side of the cutting wheel) decrease slowly compared with those in the soils (front side of the cutting wheel). When the pressures become low, foam injection at the cutting wheel will start and it results in a large pressure increase at the front of the cutting wheel compared with that at the back.

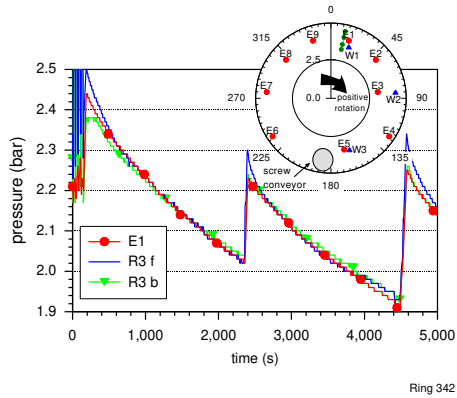


Figure 2-24. Ring 342. Pressures during stand still measured at the cutting wheel and the pressure bulkhead. Position pore pressure transducers on cutting wheel indicated with green dots.

At the top of the cutting wheel there is no sand between the wheel and the front face and there the pressures at the pressure bulkhead and the front and back of the cutting wheel are the same. This was measured during stand still after drilling of Ring 342 when the cutterhead stops drilling with the pressure gauges (green dots) in a high position (see Figure 2-24). It corresponds to the foam infiltration zone of the experimental results where the pore pressures are relatively high compared with those in the saturated sand.

2.8 Chapter summary

A laboratory set-up that can provide a hydraulic gradient comparable to field condition has been used for pressure infiltration of foam into saturated sand. Modified pore pressure transducers were used in the measurement of pore water pressures. Different test series regarding different sand types have been conducted. Based on the experimental results, the following conclusions can be made.

1) The drainage behavior is not separate from the period of foam spurt. Drainage behavior could happen even during the foam spurt period. Here in this research, the period of foam spurt is defined as the condition in which most of the foam bubbles near the foam front could travel further into deeper sand. It should be noted that the migration of the liquid among the foam could be faster than the foam bubbles,

resulting in the drainage behavior of foam but not necessarily indicate the end of the foam spurt period.

2) There are two processes during foam infiltration: foam spurt and further infiltration. Further infiltration process is found to be the main process after the foam spurt process. During foam spurt, the foam bubbles travel fast into the sand, resulting in an internal low permeable layer that creates a large pressure drop over the infiltrated sand. After the foam spurt, the total excess piezometric head will be maintained inside the internal cake and the foam penetration steps into another process of further infiltration. During further infiltration, foam bubbles can still infiltrate into the sand, but the dominating flow will be controlled by the low permeable layer created during the foam spurt process. From the measured water discharge as shown in Figure 2-6, the foam spurt period is within one hour of the tests. After foam spurt, different behaviors appear and since the time period during standstill can be over one hour, it is of engineering importance to further study the infiltration behaviors during the further infiltration period.

3) There is no impermeable layer formed at the foam-sand boundary as in a slurry infiltration test, contrary to what is suggested by Bezuijen and Xu (2019). While the foam infiltrated area could maintain a pressure drop of the excess pore pressure. Although the discharge pattern is similar to that in a slurry infiltration test, the consolidation process is not observed in foam infiltration tests. Results from additional tests show that this can be attributed to the foam spurt period in which the foam infiltrated sand thickens with elapsed time, and the permeability of the whole system is determined by this infiltrated area that results in a similar sealing effect as a filter cake in a slurry condition.

4) The experimental results also show that the foam spurt length increases with increasing bubble size. Since this layer determines the flow resistance in front of the tunnel face, better understanding on the pressures will be obtained with more information on this foam spurt length. Further work focusing on the bubble infiltration behaviors at pore scale, in which surface tension of the foam bubbles and the resulting bubble migration will be introduced in Chapter 3.

Chapter 3 Modelling the infiltration behavior of foam into saturated sand considering the capillary resistance

This chapter presents a model study on foam flow into saturated sand based on experimental analysis. The model accounts for foam spurt during foam infiltration that was experimentally discovered in Chapter 2. The maximum penetration depth by foam bubbles is estimated with a simplified micro stability model based on the minimum pressure difference over an individual foam bubble across the pore throats. Although the micro stability model underestimates the maximum penetration depth in one of the sands used, it predicts well with the results obtained for two other sands. Possible reason for the underestimation in one of the sands is discussed. Further results from the numerical model are in accordance with the measured discharge behavior during foam spurt. The general agreements suggest that the model could explain the foam flow behavior and can be used to describe foam spurt during foam infiltration that can be expected in an EPB shield tunneling.

3.1 Introduction to the infiltration model

The wide application of the EPB shield TBM has led to a number of studies in related subjects (Bezuijen & Dias, 2017; Budach & Thewes, 2015; Bezuijen, 2012; Thewes & Budach, 2012; Peila et al., 2009; Merritt & Mair, 2006; Anagnostou & Kovári, 1996). Most research focused on the bulk properties of the conditioned soils such as fluidity (Peila et al., 2009), shear behavior (Psomas, 2001), compressibility (Bezuijen, 2013) and permeability (Borio et al., 2010) and the effect of the conditioned soils on the mechanical parts of the machinery such as tool wear (Wei et al., 2019) and rotating torque (Merritt & Mair, 2006). While only limited research can be found regarding the interaction between foam and soils (Wu et al., 2020; Wang et al., 2020; Xu, 2018; Galli, 2016).

Bezuijen (2002) proposed a groundwater flow model to predict the excess pore pressure in front of the tunnel face. He compared the field measurement data and found the difference in the maximum pore pressure measured in the soil in front of a

slurry shield and an EPB shield is only small. This suggests that the groundwater flow model can be used in both slurry shield and EPB shield. The course of the pore water pressure in the soil for a slurry shield was investigated by Broere and van Tol (2000, 2001) and Bezuijen et al. (2001, 2016). Bezuijen et al. (2001, 2016) assume the formation of an internal and external filter cake. As shown in Chapter 2, slurry infiltration has been extensively studied (Xu et al., 2018; Zizka et al., 2018; Talmon et al., 2013; Min et al., 2013). Although foam infiltration has been studied experimentally by Xu et al. (2020), Galli (2016), Quebaud et al. (1998) and Maidl (1995), the mechanism of foam infiltration remains unclear.

Bezuijen and Dias (2017) developed a model to describe the pressure dissipation in the excavation chamber during standstill of an EPB shield. By fitting the field measurement data to the theoretical model, the permeability of the soils in front of the tunnel face was estimated. It was found that the permeability of the soils predicted by the model is 2 to 3 times smaller than that from field measurements. Indicating that there could be a foam infiltration layer with a high flow resistance that results in the underestimation of the soil permeability by the model of Bezuijen and Dias (2017). Although bubble migration is not included, the model was employed by Yu et al. (2020) and reasonable agreement was obtained with field measurements during both drilling and standstill.

Galli et al. (2021) conducted a series of experiments on foam penetration into cohesionless soils with the aim to assess the residual water content during drilling of an EPB shield TBM. The penetration process was described qualitatively by regression analysis using the power law model within the testing duration of 3 minutes. Chapter 2 showed that foam spurt results in an internal low permeable layer that creates a large pressure drop over the infiltrated sand. Although there are still fine bubbles migrating further into the sand after foam spurt, most of the bubbles are entrapped among the sand pores near the sand surface and the dominating flow will be the drainage from the foam.

The use of foam in EPB shield tunneling is still mainly based on experience over nearly 50 years of development and has not become a standard process regarding its

injection strategy. One possible reason is the lack in the understanding of the foam-soil interaction, of which foam flow in saturated sand plays an important role. With the aim to understand how the foam infiltration could influence the flow behavior during standstill as well as to what extent the low permeable layer with high flow resistance could be formed, a series of foam infiltration experiments was conducted as shown in Chapter 2. This chapter focuses on the model interpretation of the foam infiltration behavior. The model is based on an infiltration model for slurry infiltration (Bezuijen et al., 2016). In addition, a finite permeability of the water through the foam in the sand is assumed. An individual bubble is considered when it penetrates the sand and the limit equilibrium state is described in a simplified micro stability model. A calculation model is developed based on a micro stability model to predict the maximum penetration depth during ‘foam spurt’ (explained in the next section). The calculation model predicts the flow behavior during foam infiltration, which accounts for the bubble flow as well as the flow of the foaming liquid causing drainage of the foam. Results from the model simulation are compared with the measurement data presented in Chapter 2.

3.2 Mechanisms during foam infiltration

Analogous to the two processes of mud spurt and filter cake formation for slurry infiltration (Talmon et al., 2013), a comparable foam spurt process was observed by Xu et al. (2020) and it is adopted in this study. It was found in Chapter 2 that there is a maximum penetration depth by foam bubbles during foam spurt. After foam spurt, the migration of foam bubbles almost stops, and the flow is mainly controlled by the foam infiltrated sand which have the lowest permeability of the whole system. Further infiltration process was found to be the main process after foam spurt. The further infiltration process is somewhat similar to the deep bed filtration during slurry infiltration where bentonite particles are retained in the pores and the permeability of the sand decreases slowly (Yin et al., 2021; Xu & Bezuijen, 2019). The mechanisms may be different because during further infiltration, fine bubbles will not remain in the pores due to adhesion but are entrapped in the pores due to its larger volume compared with the pore throats. During further infiltration, only a small proportion of

the foam bubbles at the foam front could be able to travel further and the main flow will be the water flow through the foam infiltrated sand. Besides the bubble infiltration, there is always a liquid flow due to the drainage behavior of the foam. Consequently, there is an invisible liquid front ahead of the foam front (see Figure 3-1).

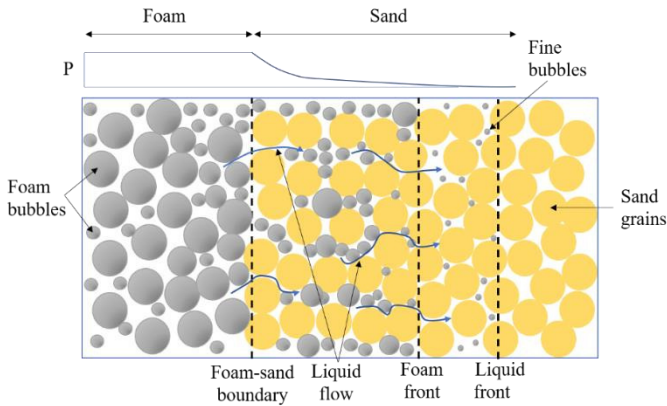


Figure 3-1. Sketch of mechanisms during foam infiltration into saturated sand

3.3 Model derivation

In this chapter, the flow behaviors during foam spurt as well as the companion liquid flow through the foam in the sand are modelled. After foam spurt, the fine bubbles migrating during further infiltration are not included in the model because it is unable to determine these amounts of the fine bubbles. The model is calibrated using the results of experiments, therefore the experimental setup is described.

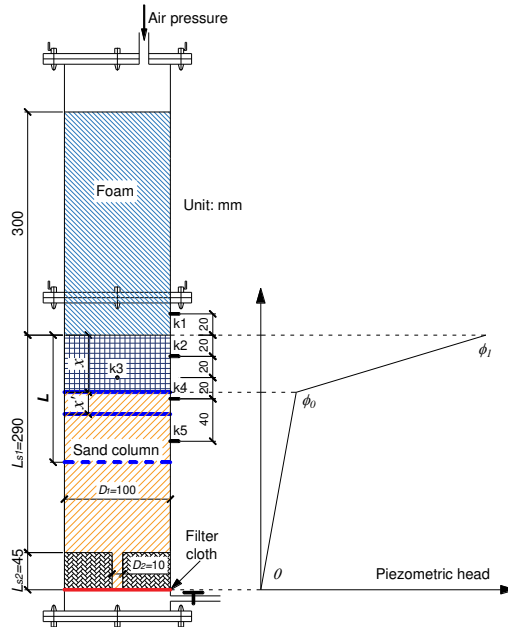


Figure 3-2. Definition sketch of penetration zone and piezometric head during foam penetration (adapted from Figure 2-1)

A definition sketch is shown in Figure 3-2, x is the penetration depth by the foam bubbles and x' the distance between the foam bubble front and the invisible liquid front. ϕ_1 represents the piezometric head in the foam above the sand surface and ϕ_0 the piezometric head at the foam front. The piezometric head at the bottom of the sand column is taken to be 0.

In this set-up, a small cylinder (with diameter D_2 and length L_{s2}) is added beneath the large cylinder (with diameter D_1 and length L_{s1}) to create an extra flow resistance which makes the equivalent length (L_s) of the sand column be equal to 5 m. The hydraulic gradient in the sand column will be $\Delta\phi/L_s = 1$ when the applied pressure is 50 kPa during the test. This is comparable to the hydraulic gradient predicted by the groundwater flow model described in Bezuijen (2002) with a shield diameter of 10 m and an extra pore water pressure of 50 kPa. Detailed explanation can be found in Chapter 2.

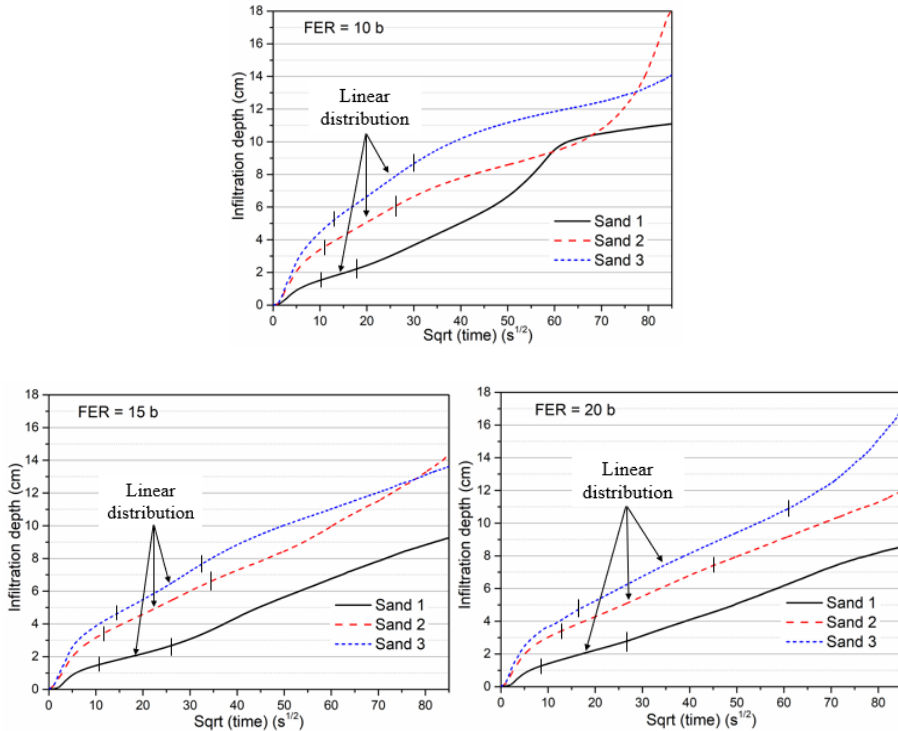


Figure 3-3. Experimental results of the water discharge against square root of time (from Figure 2-6)

Figure 3-3 shows the experimental results of the infiltration depth against square root of time. The infiltration depth is calculated assuming there is no liquid drainage from the foam and therefore this depth is larger than the actual penetration depth by foam bubbles. It shows that after the initial fast penetration of the foam bubbles, there is a slower discharge period which is approximately linear against square root of time. It was found that the permeability of the foam-infiltrated sand (x in Figure 3-2) is the lowest in the whole system. There is no impermeable layer formed on top of the sand, but the linear part is related to the layer of low permeability formed during foam spurt. After foam spurt, there is limited foam bubble infiltration and the dominant flow will be the water flow from the foam. The linear line against square root of time is the result of the increase of the foam infiltration layer and therefore can be simulated. There are some different discharge patterns after the linear distribution period for some unknown reasons as can be seen from Figure 3-3. This chapter will only focus

on the simulation of foam spurt which comprises the initial fast discharge and the linear discharge against square root of time shown in Figure 3-3.

As shown for slurry infiltration (Bezuijen et al., 2016), the penetration of slurry into the sand does not follow Darcy's law, because slurry is a fluid with yield stress and a certain pressure drop is necessary to push the slurry further into the sand. The experimental results from Chapter 2 suggest that there is a maximum penetration depth (L_m) when foam is pressurized into saturated sand, indicating a yield stress in the foam flow. Assume foam to be a Bingham fluid, the flow in porous media can be expressed as follows (Bezuijen et al., 2016):

$$v_f = \frac{k_f}{n} \left(\frac{d\phi}{dx} - i_t \right) \quad (3-1)$$

With v_f the penetration velocity of the foam bubbles, k_f the permeability of the sand for foam, n_s the porosity of the sand and i_t the threshold hydraulic gradient.

The threshold hydraulic gradient (i_t) can be calculated when the maximum penetration depth (L_m) is known. Specifically, because there is a water flow after the foam has reached its maximum penetration depth, indicating that there is a certain pressure difference over the foam front and the outlet at the maximum penetration depth. The threshold hydraulic gradient (i_t) can be estimated:

$$i_t = \frac{\phi_1 - \phi_{0,end}}{L_m} \quad (3-2)$$

With $\phi_{0,end}$ the piezometric head of the foam front at maximum penetration depth.

Considering that there is always drainage behavior even during the foam spurt period, an extra water flow through the sandy foam should be accounted for in the total discharge.

$$v_{fw} = k_{fw} \frac{\phi_1 - \phi_0}{n_s x} \quad (3-3)$$

The pore water velocity in the sand ahead of the foam front can be calculated:

$$v = k_s \frac{\phi_0}{n_s (L_s - x)} \quad (3-4)$$

With k_s the permeability of the saturated sand and v the discharge rate of water.

By definition, there is a relation:

$$v = v_f + v_{fw} \quad (3-5)$$

At the maximum penetration depth, the bubble penetration stops ($v_f = 0$), and there will only be a water flow. With flow consistency, it comes to the following relation:

$$k_{fw} \frac{\phi_1 - \phi_{0,end}}{L_m} = k_s \frac{\phi_{0,end}}{L_s - L_m} \quad (3-6)$$

The Equations (3-1) ~ (3-4) can be solved numerically using an explicit scheme starting from $x = 0$ at $t = 0$.

The maximum penetration depth (L_m) can be obtained by analyzing the micro stability of an individual foam bubble across the sand pores. Rossen and Gauglitz (1990) developed a model to describe the minimum pressure gradient of foam flow through porous media. But the pressure difference in their model is between gas and liquid which is more applicable in the field of enhanced oil recovery. While here a model to describe the difference in pore water pressure is needed. Therefore, a simplified micro stability model is proposed to get L_m .

In the experimental part presented in Chapter 2, one fine sand and two medium sands were tested to represent different sand stratum. The FER of the foam used in the experiment were 10, 15 and 20. Grain (bubble) size distribution curves of the three types of sand (foam) are shown in Figure 2-4. It should be mentioned that the bubble size is measured at atmospheric pressure and calculated at an absolute pressure of 1.5 bar according to Boyle's Law. The volume of an individual bubble will increase as it travels further due to the decrease in its surrounding pore water pressure. The compressibility in this case will be discussed in the following part.

The filter rule derived by Terzaghi and regulated in USACE (2000) is a common guidance for filter design in dams and dikes. A filter material is placed downstream to prevent particle loss of the base material. A major criterion for the filter material is $D_{15}/d_{85} \leq 4$ (D_{15} for the filter material and is the diameter which 15% of the filter material's mass content smaller than, d_{85} for the base material). Assume the foam being a base material with the same gradation and the sand column being a filter

material, the potential of particle loss from the base material into the filter material is first checked with the filter rule. A regular base material is different to foam because sand particles cannot be compressed or deformed like foam bubbles. If it fulfills the filter rule, there would hardly be any transportation of foam bubbles into the pore space of the sand column without changing its shape. The related values are summarized in Table 3-1. It shows that the combinations of different base and filter materials fulfil the filter rule, suggesting that no bubble penetration could take place without changing its shape.

Table 3-1. Values of D_{15}/d_{85} found in different combinations

Filter Base	Sand 1	Sand 2	Sand 3
Foam 1	0.29	0.28	0.44
Foam 2	0.26	0.28	0.56
Foam 3	0.21	0.22	0.44

Figure 3-4 shows a sketch of shape changes in a bubble penetration over an individual pore throat. The changes in shape require a pressure difference to initiate the deformation which is related to the geometry of the pore throat and the surface tension of the bubble. Here the mechanism is first discussed in general and the determination of relevant parameters will be introduced subsequently.

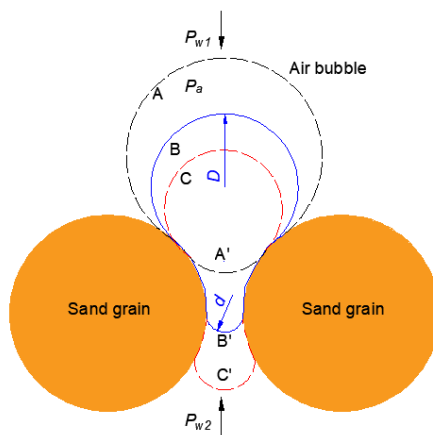


Figure 3-4. Principle of the bubble deformation during foam penetration of a pore throat

As illustrated in Figure 3-4, the bubble changes from position A to B and C . A' , B' and C' denote the bottom part of the bubble at corresponding moments, respectively. The pore water pressure on top of the bubble is P_{w1} and at the bottom P_{w2} . The difference in pore water pressure on either side of the pore throat ($P_{w1}-P_{w2}$) pushes the bubble downwards that the bottom part bulges through the pore throat.

Because the surface tension resists the forward movement during the change from A' to B' , the capillary pressure is the greatest at the narrowest position B' where the bottom part of the bubble has the largest curvature. The movement will carry on from B to C when the pressure difference ($P_{w1}-P_{w2}$) can overcome this largest capillary pressure. Because position $B-B'$ is very crucial to a bubble penetration, it will be analyzed from the equilibrium state point of view.

By the definition of surface tension (γ), the following relations can be obtained:

$$P_a - P_{w1} = \frac{4\gamma}{D} \quad (3-7)$$

$$P_a - P_{w2} = \frac{4\gamma}{d} \quad (3-8)$$

With D the local diameter on top of the bubble and d the local diameter at the narrowest point in the throat.

Combining Equations (3-7) and (3-8) yields:

$$P_{w1} - P_{w2} = 4\gamma\left(\frac{1}{d} - \frac{1}{D}\right) \quad (3-9)$$

Equation (3-9) represents the minimum difference in pore water pressure for a bubble to travel through an individual pore throat. Above this pressure difference, the bubble will continue to penetrate further. At the maximum penetration depth (L_m), the pressure difference will no longer be able to push the bubble forward, and the penetration will stop.

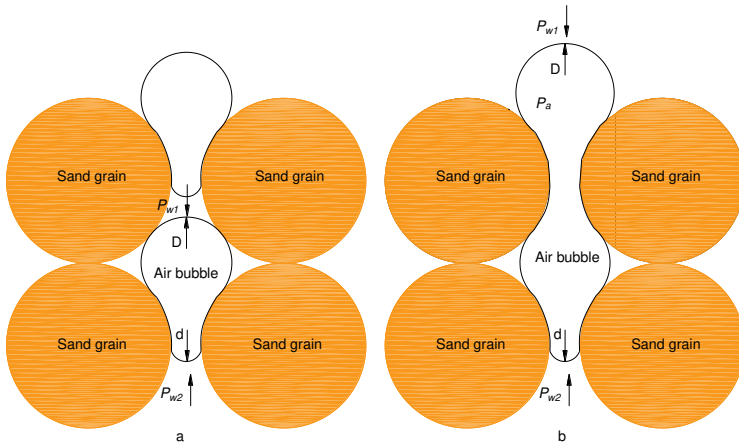


Figure 3-5. Possible conditions when foam bubbles penetrate through pore throats

There can be two different conditions regarding the sizes between the bubble and the pore body with the values listed in Table 3-2, as shown in Figure 3-5, these two conditions mainly influence the local diameter on top of the bubble (D).

1) The bubble size is equal to or smaller than the pore body (Figure 3-5a) but bigger than the throat diameter (Sand 3-FER 10). In this case, a foam bubble can fully pass through an individual throat before it starts the next penetration. The pressure drop over one foam bubble is equal to the pressure difference over one pore throat. D in this case will be taken as the average diameter of the bubbles. The diameter of the bubble is influenced by the pore water pressures at different vertical locations. Assume i (starting from $i=1$) to be the number of bubble penetration across the pore throat. The pressure drop in one bubble penetration is (neglecting the hydrostatic pressure difference):

$$P_{wi} - P_{w(i+1)} = 4\gamma \left(\frac{1}{d} - \frac{1}{D_i} \right) \quad (3-10)$$

With i the number of bubble penetrations across the pore throat and D_i the diameter at that point which can be calculated according to Boyle's law:

$$D_{(i+1)} = 3 \sqrt{\frac{P + P_{wi}}{P + P_{w(i+1)}}} D_i \quad (3-11)$$

With P the atmospheric pressure.

The calculation scheme stops when $P_{w(i+1)} \leq 0$. Assuming the pore space to be equal to the diameter of the sand grains, the maximum penetration depth can be calculated by:

$$L_m = MD_S \quad (3-12)$$

With M the maximum value of i and D_S the average diameter of the sand grains.

The calculation scheme described by Equations (3-10) to (3-12) can be carried out starting from $i = 1$, $D_i = D$ and $P_{w1} = 50$ kPa.

2) The bubble size is bigger than the pore body (Figure 3-5b). An individual bubble needs to take up more than one pore throat at a time that the bubble flows as ‘bubble trains’ during penetration (Rossen, 1990). In this case, a volume factor (α) is introduced to represent the number of pore throat occupied by one bubble. The volume of the bubble can be calculated when the pore water pressure is known. A simplification in this model takes the local diameter on top of the bubble to be equal to the pore space which is equal to the diameter of the sand grains, the pressure drop in one bubble penetration is:

$$P_{wi} - P_{w(i+1)} = 4\gamma\left(\frac{1}{d} - \frac{1}{D}\right) \quad (3-13)$$

The number of foam bubbles along the infiltration path can be obtained by:

$$N = \frac{\Delta P}{P_{wi} - P_{w(i+1)}} \quad (3-14)$$

With N the number of bubbles along the maximum penetration depth and ΔP the total excess pore pressure.

Since the volume of the bubbles is inversely proportional to the absolute pressure, the volume factor for bubbles at different places along the penetration path can be obtained and the maximum penetration depth is:

$$L_m = D \sum_{i=1}^N \delta \frac{P + \Delta P}{P + [\Delta P - (i-1) \frac{\Delta P}{N}]} \quad (3-15)$$

With δ the volume factor which is determined by the volume ratio between the bubble and the pore space.

Here d_{10} ($d_{10,s}$ for sand and $d_{10,f}$ for foam) is taken to be the characteristic values that are summarized in Table 3-2.

Table 3-2. Parameters found in experiments and model simulation

	FER	$d_{10,s}$ (m)	$d_{10,p}$ (m)	$d_{10,f}$ (m)	Volume factor (δ)	L_m (m)		
						Micro stability model	Model fit	Experiment*
Sand 1	10			1.8×10^{-4}	4	0.016	0.017	$0 < L < 0.02$
	15	1.2×10^{-4}	3.5×10^{-5}	2.4×10^{-4}	8	0.033	0.036	$0.04 < L < 0.06$
	20			2.6×10^{-4}	11	0.045	0.045	$0.04 < L < 0.06$
Sand 2	10			1.8×10^{-4}	3	0.026	0.06	$0.04 < L < 0.06$
	15	1.3×10^{-4}	5.5×10^{-5}	2.4×10^{-4}	7	0.061	0.061	$0.04 < L < 0.06$
	20			2.6×10^{-4}	8	0.069	0.069	$0.06 < L < 0.1$
Sand 3	10			1.8×10^{-4}	1	0.017	0.09	$0.06 < L < 0.1$
	15	2.6×10^{-4}	7.0×10^{-5}	2.4×10^{-4}	1	0.016	0.09	$0.06 < L < 0.1$
	20			2.6×10^{-4}	1	0.023	0.09	$0.06 < L < 0.1$

* Experimental data from Chapter 2.

3.4 Results and discussion

3.4.1 Maximum penetration depth

The surface tension (γ) of the foaming liquid was measured with a single capillary tube with an inner diameter of 0.15 mm and outer diameter of 0.25 mm and a length of 300 mm (CM Scientific, CV1525 Borosilicate Glass Round Capillaries) at room temperature of 20 °C. The measurement was also conducted with water as a reference. Measurement results are listed in Table 3-3.

Table 3-3. Measured capillary rise and calculated surface tension

	h (m)	γ (N/m)
water	0.1982	0.0728
Foaming liquid	0.0583	0.0214

The measurement result on water is very close to standard value of 0.07275 N/m (Vargaftik et al., 1983), indicating the reliability of the capillary rise method.

The throat diameter of the sand was determined by the measured water retention curve. Water retention curve was measured using the hanging water column test in which suction pressures were created by varying water column in a stepwise manner (see Lins, 2009). The testing method has the advantage of its ability to obtain very small suction pressure among a small pressure range since sand usually presents a relatively small range of air entry values (Lins, 2009). During the measurement, air will displace the water in the pore space as long as the pressure difference can overcome the capillary pressure. As indicated in Figure 3-4, the capillary pressure is the largest at the narrowest point with the throat diameter d . Therefore, the measured water retention curve has a relation with the throat diameter. By fitting the measurement data to the van Genuchten model (1980), the range of air entry values for each sand can be obtained statistically using:

$$P - P_s = \frac{4\gamma_w}{d} \quad (3-16)$$

With P the atmospheric pressure, P_s the suction pressure (negative) and γ_w the surface tension of water.

Take Sand 1 as an example, the air entry value is between 3.2~12 kPa and the calculated throat diameter is between 0.024~0.091 mm. The pore space for each sand is considered to be the same to its characteristic grain size $d_{10,s}$. With the maximum and minimum throat diameter, a distribution curve regarding the throat diameter can be developed with different air entry values and their corresponding volumetric water contents. The results are shown in Figure 3-6.

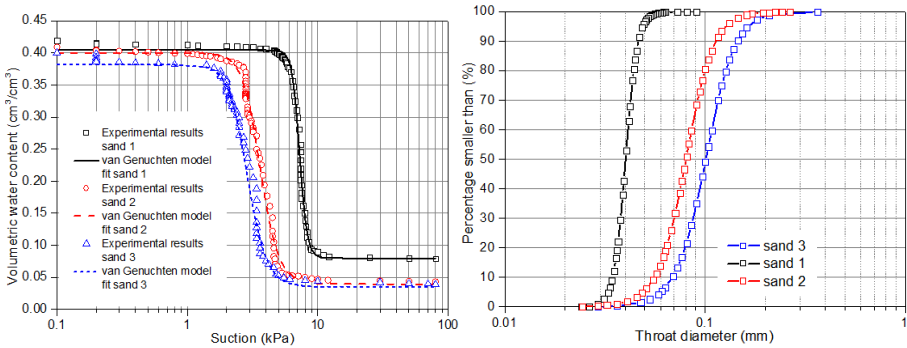


Figure 3-6. Measured water retention curves and their fit with van Genuchten model (left) and the distribution curve of the throat diameter for each sand (right).

With the distribution curve, $d_{10,p}$ is taken to be the characteristic throat diameter and the values for each sand are listed in Table 3-2. The Terzaghi model assumes the throat diameter ($d_{10,p}$) to be approximately one quarter of the characteristic grain size ($d_{10,s}$). While the ratio of $d_{10,p} / d_{10,s}$ can be found in Table 3-2 and it is 0.29, 0.42 and 0.27 for Sand 1, Sand 2 and Sand 3, respectively. It can be seen that only for Sand 2, the ratio is apparently different from the Terzaghi value of 0.25, which could be induced by its relative density of 70%. For Sand 1 and Sand 3, it is quite close (0.29 and 0.27 for Sand 1 and Sand 3, respectively) at the relative density of 80%. Table 3-2 shows that the micro stability model prediction compared with experimental results from Chapter 2. It shows that the model prediction for FER 10 is less than half the results with that for FER 15 and FER 20 in Sand 1 and Sand 2. This is caused by the smaller bubble size in FER 10 that the “bubble trains” are shorter, while the pressure difference at maximum penetration depth is the same when foam bubbles are larger than the pore space. This corresponds to the condition shown in Figure 3-5b in which bubble size is larger than the pore space. For Sand 3, however, Table 3-2 shows little difference in

model prediction with different FERs. This is induced by the situation shown in Figure 3-5a in which bubble size is equal to or smaller than the pore space. Table 3-2 indicates that the model predicts well compared with the experimental results for Sand 1 and Sand 2. It underpredicts the maximum infiltration depth for Sand 3, probably because finer bubbles are smaller than the larger pore throats in Sand 3 and thus are simply transported. Although Table 3-1 shows that there is no bubble penetration without changing its shape with the filter rule, Figure 2-4 and Figure 3-6 show that a large proportion of foam bubbles are smaller than the measured larger pore throats in Sand 3. For foam FER of 10, the proportion is about 70% and about 60 % and 40 % for foam FER of 15 and 20, respectively. As a consequence, the multiple number of bubbles in a single pore space likely result in the bubbles being more or less connected, which results in a smaller pressure drop over an individual pore throat than the model prediction.

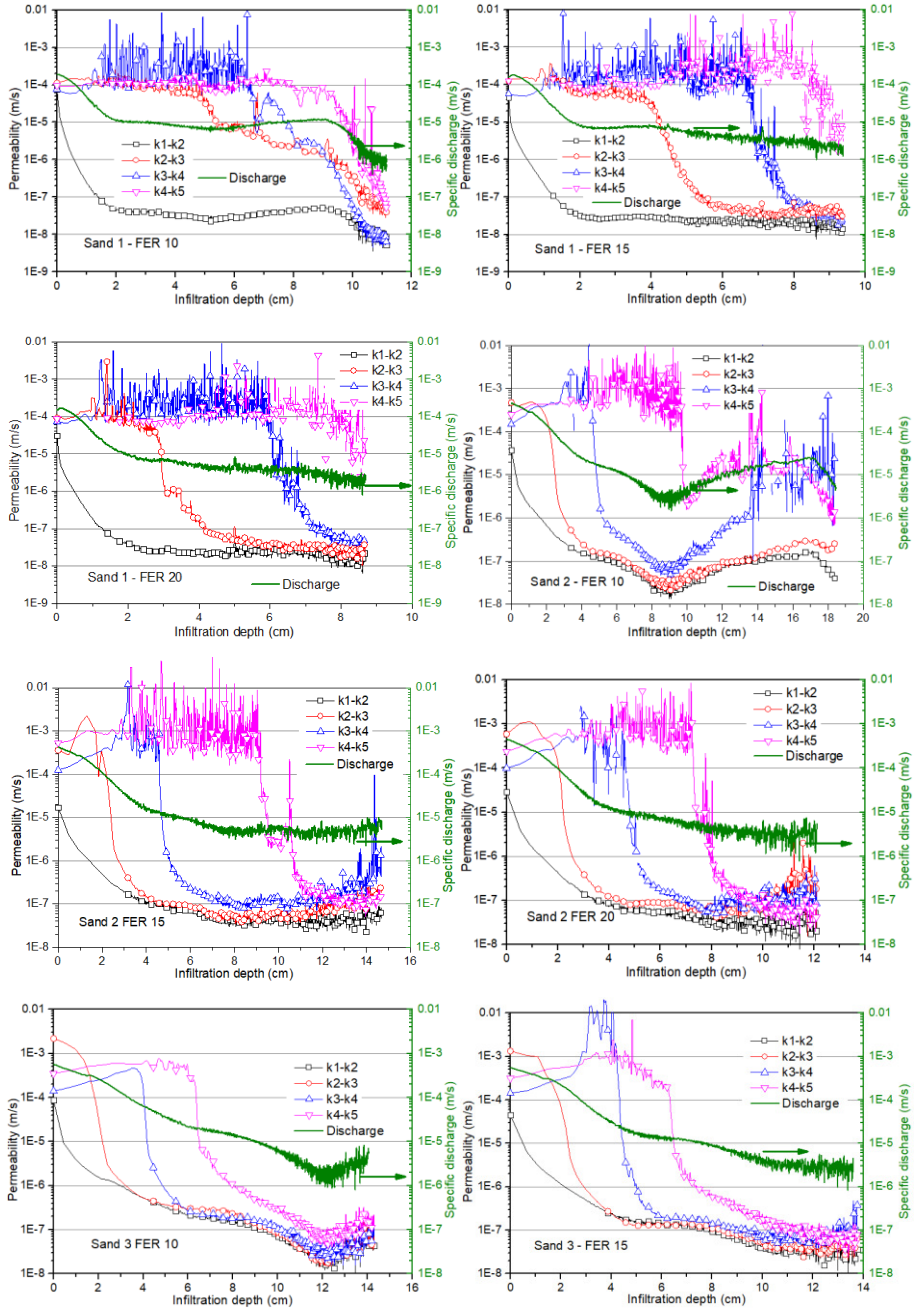
3.4.2 Model simulation

The permeability of the sandy foam for water (k_{fw}) can be determined according to Darcy's Law:

$$k_{fw} = \frac{\Delta L Q}{A_C \Delta \phi} \quad (3-17)$$

With ΔL the distance between two adjacent pressure transducers and $\Delta \phi$ the corresponding difference in piezometric head. The distance (ΔL) between k_1 and k_2 is only 2 cm because the first 2 cm is pure foam. For k_{2-3} and k_{3-4} this distance is also 2 cm while for k_{4-5} it is 4 cm.

At the maximum penetration depth, the bubbles will reach an equilibrium state which is described in the micro stability model. At the equilibrium state, the measured pore pressures by adjacent transducers can be used to calculate the permeability of the sandy foam, because there is only a water flow.



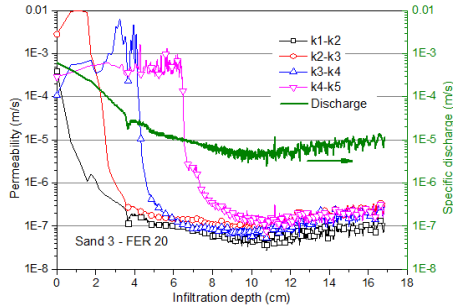


Figure 3-7. Calculated permeabilities and specific discharge as a function of infiltration depth

Figure 3-7 shows the calculated permeabilities using Equation (3-17). The infiltration depth on the horizontal axis was calculated assuming there was no liquid drainage from the foam and therefore is larger than the actual penetration depth by the bubbles. It shows calculated values exhibit decreases in permeabilities by several orders of magnitude after the foam bubbles penetrated the corresponding sand layers. For k_{1-2} this decrease happens at the beginning of the test, because the foam bubbles immediately penetrate the sand pores when the test starts. The values of k_{2-3} kept constant for some infiltration depth, after which they also presented a sharp decrease. A similar situation applies to k_{3-4} , but only after the foam front has penetrated the sand layer sandwiched by k_3 and k_4 . Some fluctuations of k_{4-5} were observed at the later part of the tests, which is attributed to the small water discharge at the later stage because the accuracy of the pressure transducers and the discharge rate started to influence the results. It should be mentioned that the theoretical infiltration depth at which k_{2-3} and k_{3-4} start to decrease for the test with Sand 1 FER 10 should be 0.02 m and 0.04 m, respectively. While these two values are 0.04 m and 0.065 m from Figure 3-7, larger than the theoretical values. It suggests that the drainage from foam has resulted in a larger infiltration depth when calculated with the discharged water. Similar condition applies to other tests shown in Figure 3-7.

Before the foam bubbles infiltrate into the sand pores, the calculated values by Equation (3-17) should be constant and they should reflect the permeability of the sand sample.

Table 3-4 shows that there is a general agreement when comparing the sand

parameters and the calculated constant values from Figure 3-7.

Basic requirements should be applied when employing the permeability of the sandy foam (k_{fw}) calculated by Equation (3-17) in the numerical model:

- 1) The foam bubbles stop penetrating further. This criterion can be roughly met when the maximum penetration depth described in the micro stability model is reached. Although some local unstable state can be expected during the further infiltration process, most part of the foam bubbles in the sand are stranded and the calculated values by Equation (3-17) will be regarded as the permeability of the sandy foam (k_{fw}).
- 2) The sand layer sandwiched by adjacent pressure transducers is fully penetrated by the foam bubbles. This is to ensure that the seepage length through sandy foam is equal to the distance between adjacent transducers when criterion 1 is fulfilled. It can be distinguished from Figure 3-7 whether this criterion is fulfilled or not. For instance, when k_{4-5} starts decreasing, then the sand layer between k3 and k4 is fully infiltrated by foam bubbles because now the bubbles have reached beyond k4.

Following the above discussions, k_{fw} was chosen to be around 2×10^{-8} m/s for the test with Sand 1 FER 10 according to Figure 3-7. The values are listed in Table 3-4.

Another parameter that needs to be obtained for the numerical model is the permeability of the sand for foam (k_f). Since it is unrealistic to obtain through measurement, k_f was determined by fitting the measurement data into the simulation results.

The fitting procedure starts from k_f and then both L_m (from the micro stability model) and k_{fw} (from Figure 3-7) can be slightly adjusted if model output can better fit into the experimental results. The resulting L_m can be found in Table 3-2 and the permeabilities in Table 3-4. It should be mentioned that the changes in parameters are manual to get better outputs compared with experimental results.

Table 3-4. Permeabilities found in experiments and model simulation

	$k_s (\times 10^{-4} \text{ m/s})$		FER 10 ($\times 10^{-8} \text{ m/s}$)			FER 15 ($\times 10^{-8} \text{ m/s}$)			FER 20 ($\times 10^{-8} \text{ m/s}$)		
	k_s (Figure 3-7)	k_s^*	k_{fw} (Figure 3-7)	k_{fw}	k_f	k_{fw} (Figure 3-7)	k_{fw}	k_f	k_{fw} (Figure 3-7)	k_{fw}	k_f
Sand 1	1.0	1.5	2.0	2.6	8.0	2.0	1.8	4.0	2.0	1.5	3.0
Sand 2	4.0	5.0	2.0	4.3	42.0	3.0	4.0	30.0	2.0	2.3	25
Sand 3	6.0	6.0	15.0	5.8	80.0	10.0	3.6	45.0	5.0	2.3	40

* Experimental data from Chapter 2.

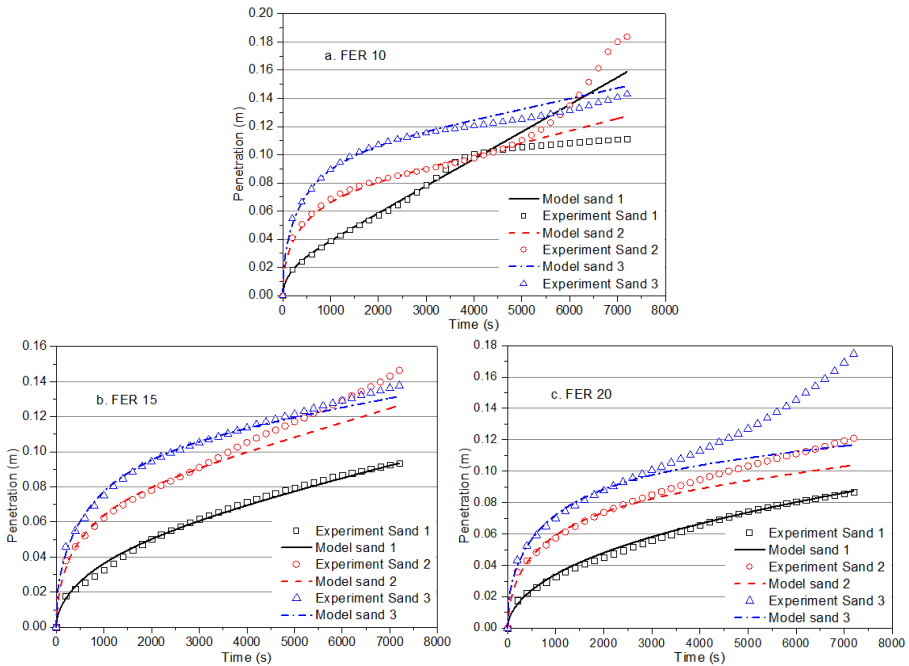


Figure 3-8. Penetration depth against time from experiments compared to model results.

Results from both model simulation and experiments are plotted in Figure 3-8. Although the micro stability model underpredicted the maximum infiltration depth for the tests with Sand 3, the simulation yields good agreements with L_m of 0.09 m. For Sand 1 and Sand 2, the maximum penetration depth (L_m) fits well with the experimental results except in the test with Sand 2 FER 10, where the value of L is 0.06 m, larger than 0.026 m found in the micro stability model. A possible reason for the underestimation is that 5 % of the foam bubbles in foam of FER 10 are smaller than the pore throats in Sand 2. The smaller bubbles can simply be transported during the test, which results in a larger penetration depth than the micro stability model prediction. While in general, the good agreements between experiments and model simulation indicate the right physics of the model presented in this study. It suggests that the model can be used to describe the infiltration behavior during foam spurt which can be expected during EPB shield tunneling.

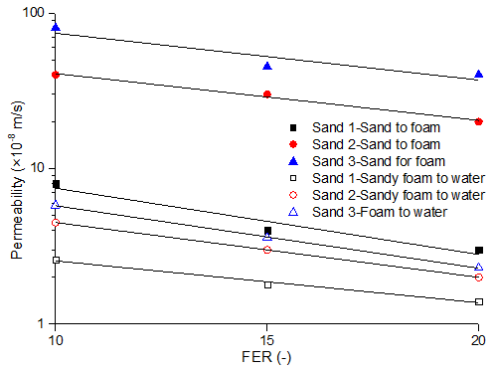


Figure 3-9. Permeabilities used in model simulation

Figure 3-9 shows the values of the permeabilities used in the model simulation. It shows that with a certain sand type, its permeability to foam is decreasing with an increasing FER. And the permeability of the sandy foam formed during pressure infiltration decreases with an increasing FER. Suggesting that a foam with larger foam bubbles and less water content (bigger FER) results in a lower permeability when infiltrating into the sand. With a coarser sand, its permeability to a certain foam will be larger, which is logical because the throat diameter will be larger in a coarser sand, and it will be easier for both foam bubbles and water to pass through. An interesting point worth further investigation is that all permeabilities decrease by a factor of approximately 2 when FER increases from 10 to 20. A possible reason is that the smaller liquid content in the foam of FER 20 results in the film of the bubbles being thinner, further resulting in a smaller permeability.

Furthermore, the model can be used to calculate the foam infiltration in the tunnel front and the water flow from the excavation chamber during standstill. To do that Equation (3-3) has to be changed (Bezuijen et al. (2016)):

$$v = k_s \frac{\phi_0}{nR} \quad (3-18)$$

The other equations remain the same.

The calculation results shown in Figure 3-8 will be identical for a field test in saturated sand with an EPB shield with 10 m diameter, the permeabilities of the sand 1, 2 and 3 and a face pressure that is 50 kPa above the pore water pressure.

3.5 Chapter summary

This chapter presents the model interpretation of the mechanisms during foam infiltration, based on the analysis of the experiments in Zheng et al. (2021). A calculation model is established to describe the flow behavior during foam infiltration into saturated sand tailored to EPB shield tunneling. The model describes the foam bubble flow as well as the companion water flow during foam spurt. The maximum penetration depth by foam bubbles is predicted with a simplified micro stability model. The micro stability model results in good predictions when the foam bubbles are bigger than the pore throat in the sand, while it underestimates the maximum penetration depth in other cases (for example, the tests with Sand 2 – FER 10 and Sand 3). Model results show good agreements when compared with experimental results during foam spurt.

The good agreement between the model and experimental results confirms the mechanisms during pure foam infiltration. Although further research is needed for sandy foam infiltration, which seems to be a more realistic situation in an EPB shield, pure foam infiltration is still a possible scenario during standstill as foam is injected through the cutter head to maintain the pressure from time to time. The injection will create a pure foam infiltration which is described in this chapter.

Despite the fact that the model neglects the infiltration behavior after foam spurt, the model provides a good way to quantify the flow behavior during foam infiltration. Further application of the model can be extended to the prediction of the pore pressures in front of the tunnel face, which could help better understand the pressure development and the foam-soil interaction in EPB shield tunneling.

Chapter 4 Experimental study on sandy foam infiltration into saturated sand for EPB shield tunneling: A Mechanism Study

This chapter investigates the infiltration behavior of a foam-sand mixture into saturated sand that can be expected at the tunnel face in an EPB shield. The infiltration behavior is studied in the set-up from Chapter 2 in which pore pressures are measured at different locations. Influence from foam injection ratio (FIR), remaining water content and sand type are examined. It was found that there is hardly any foam infiltration with a low FIR (40 Vol %) for the fine sand used in this experiment. Consolidation of the foam-sand mixture is the dominating process that results in a consolidated mixture with a smaller permeability. With a higher FIR and a lower water content, the foam infiltration results in a foam infiltration layer which has a lower permeability than the consolidated mixture. Further analysis indicates that the sand matrix plays an important role in determining the permeability of a foam-sand mixture. The bubble penetration is influenced by the ratio between the permeability of the foam-sand mixture and the saturated sand. Mechanisms are discussed and implications for field applications are forwarded.

4.1 Introduction

As discussed in Chapter 2, the active support in the excavation chamber should be a fluid pressure that could counterbalance the earth pressure as well as the hydrostatic pore pressure below the groundwater level. With the support pressure in the chamber, the excess pore pressure will induce a ground water flow from the chamber to the soils ahead.

Figure 4-1 shows a schematic view of a foam-soil-mixture in the excavation chamber during drilling and standstill. The excavation spoil is removed through the rotating screw conveyor at the bottom back of the chamber. The pressure in the chamber can be controlled by both adjusting the thrust force from the shield jack and regulating the rotating speed with the screw conveyor. The weight of the foam-soil-mixture in the chamber introduces a vertical pressure gradient that results in larger bubbles at the top

of the tunnel compared with the bubble size at the invert (Bezuijen et al., 2020). Consequently, the apparent FIR is larger in the upper part of the tunnel compared with that in the lower part.

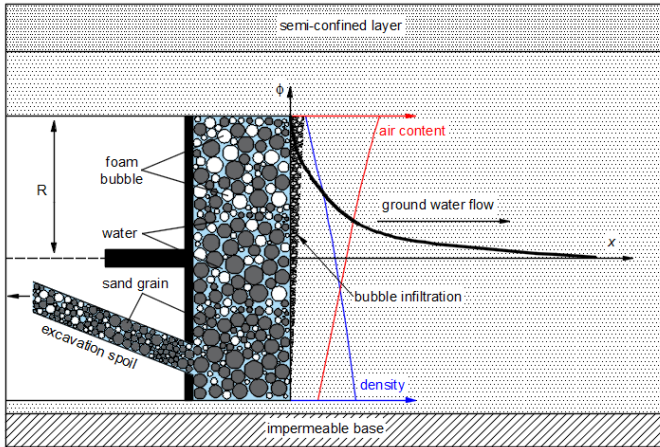


Figure 4-1. Schematic view of a foam-sand-mixture in the excavation chamber

The theoretical model from Bezuijen and Dias (2017) showed good agreement when compared with field measurement data regarding the pressure dissipation in the excavation chamber. However, by fitting the field measurement data to the theoretical model, the permeability of the soils in front of the tunnel face was found to be 2 to 3 times smaller than that from field measurement results. Comparing this conclusion with that from Bezuijen et al. (2006) and Broere and van Tol (2001), there could be a foam infiltration layer with a high flow resistance at the tunnel face.

Since the full coverage of the tunnel face solely by foam is not realistic, and the excavation chamber is filled with a foam-sand mixture which is usually the medium that performs for face support (Galli, 2016; Maidl, 1995). It will be more applicable to study the infiltration behavior of a foam-sand mixture into the soil in front of the tunnel face. This chapter will present the experimental study of sandy foam infiltration into saturated sand.

One of the main objectives of the experimental study with foam-sand mixtures is to investigate whether there is an infiltration area by foam bubbles that results in a low permeable layer. In the experiments with foam-sand mixture, the possibility of a low permeable layer formed during infiltration is first explored with a variation of FIR.

The influence on permeability reduction by foam infiltration was systematically studied in the experiments with pure foam and it is proven that the permeability of the sand can be decreased by several orders of magnitude as shown in Chapter 2. With the low permeable layer, the ground water flow will be limited and the fluid pressure in the excavation chamber can be effectively transferred to the soils in front of the tunnel face. Without this low permeable layer, more water will flow from the excavation chamber to the soils and the consolidation process in the excavation chamber could result in effective stresses during standstill, which could induce, as a consequence, an increase in the torque required to resume the cutting process.

Another goal of the study is to investigate the influence of the water content on the permeability of the foam-sand mixture as well as the possible infiltration by foam. Model test results from Bezuijen and Schaminée (1999) show that the permeability of such a mixture can be a factor of 100 smaller than the original saturated sand when all free water is expelled by foam, while only a factor of 2 without pore water replacement. This has consequences for the support pressure, because the excess pore pressure in the excavation chamber will dissipate relatively fast when the permeability of the mixture is large compared with a smaller permeability (Bezuijen & Dias, 2017). Although foam penetration was not observed in the model tests by Bezuijen and Schaminée (1999), Galli (2016) argued that the occurrence of foam penetration would depend on the density of the foam-soil-mixture. While Xu (2018) found that a low permeable layer could be realized by foam infiltration at a certain FIR. The characterization on foam infiltration therefore needs to be implemented based on bubble migration. The influence from different FIRs and the remaining water content will be investigated. These will help to better understand the infiltration behavior that is fundamental in field applications.

4.2 Definitions

In this chapter the following definitions are used:

FER: foam expansion ratio, the ratio between the total amount of foam (by volume Q_F) and the amount of surfactant solution (Q_L) (water and surfactant).

FIR: foam injection ratio, the ratio between the volume of the injected foam and the

excavated soils.

PWR: pore water replacement, the expelled pore water (λ) from a unit soil divided by the soil porosity (n_s)

4.3 Experimental study

4.3.1 Foam, sand and foam-sand mixture

The foam and the sand used in this study are the same as the ones used in Chapter 2. The characteristics of the sand are listed in Table 4-1. In this study, foam with FER of 10 (under applied pressure of 0.5 bar) was used to make the foam-sand mixture. The characteristics of the sand are listed in Table 4-1.

Table 4-1. Characteristics of the sand types

	d_{10} (mm)	d_{50} (mm)	d_{60} (mm)	d_{80} (mm)	n_{min} (-)	n_{max} (-)	Relative density (%)	k_s (m/s)
Sand 1	0.12	0.16	0.17	0.21	0.38	0.47	80	1.5×10^{-4}
Sand 2	0.13	0.3	0.34	0.41	0.38	0.48	70	5.0×10^{-4}
Sand 3	0.26	0.46	0.51	0.56	0.38	0.48	80	6.0×10^{-4}

The amount of pore water taken into the excavation chamber by the cutting action is influenced by foam infiltration. This has consequences on the water content of the foam-sand mixture and further influences the infiltration behavior of the foam-sand mixture. The concept of pore water replacement (PWR) could help to better understand foam bubble infiltration. Figure 4-2 shows a conceptual view on FIR and pore water replacement. The volume of injected foam in an original unit soil is defined as FIR, and the expelled pore water (λ) from the unit soil divided by the soil porosity (n_s) represents the pore water replacement. If all pore water is expelled by foam, then its PWR is 1.

It should be noted that the concepts FIR and PWR are independent parameters. In field applications, there is smallest FIR that could be able to increase the porosity of the excavated soil no smaller than its maximum porosity. The PWR is only influenced by the foam bubble infiltration.

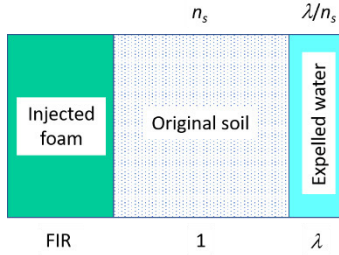


Figure 4-2. Definition sketch for FIR and pore water replacement ratio (adapted from Bezuijen, 2012)

Figure 4-3 shows the measured foam infiltration velocity in the tests with pure foam (from Chapter 2). It shows that the infiltration velocity at the beginning of the tests can be 0.5~1.4 mm/s which is comparable to the drilling velocity during tunneling. Assume the drilling velocity in field condition to be around 1 mm/s, then there can be different percentage of pore water that is displaced by foam infiltration. In this study, the pore water replacement was varied in different tests to study its effect on the results as shown in Table 4-2.

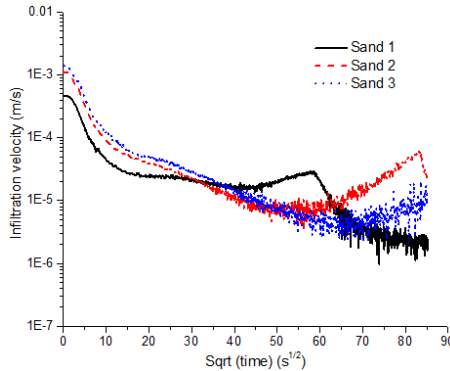


Figure 4-3. Measured infiltration velocity of foam in experiments with pure foam (FER 10)

Therefore, the pore water replacement ratio in tests with Sand 1 in this study is varied in the experiments to investigate the possible blockage as well as the influence on its permeability. For example, 0.3 means that 30% of original water in the saturated sand has been expelled by foam and therefore the foam-sand mixture contains less water than the original saturated sand. For Sand 2 and Sand 3, Figure 4-3 shows that the foam infiltration velocity is larger than the drilling velocity, indicating that all the

excavated soil is infiltrated by foam. Galli (2016) shows that not all pore water in the sand can be replaced by foam infiltration and the residual water should be considered in the evaluation of the foam-soil-mixture. There will be an amount of residual water content in the soil even when it is fully infiltrated by foam. The residual water content was determined with the measured soil-water retention curve in this study and applied to the design of the foam-sand mixture. The total amount of conducted experiments was listed in Table 4-2.

Table 4-2. Properties of the foam-sand mixtures

Sand	Number	FIR (Vol %)	PWR (-)	FER _m (-)	Fraction (Vol %)			Density (kg/m ³)
					Air	Liquid	Sand	
Sand 1	1-1	20	0	1.4	15	35	50	1675
	1-2	30	0	1.6	21	33	46	1554
	1-3	40	0	1.8	26	31	43	1450
	1-4	50	0	2.0	30	30	40	1360
	1-5	60	0	2.2	34	29	38	1281
	1-6	60	Residual	4.8	42	11	47	1351
	1-7	70	0	2.3	37	28	35	1212
	1-8	70	0.15	2.5	38	25	37	1220
	1-9	70	0.3	2.8	40	22	38	1228
	1-10	70	0.5	3.3	42	18	40	1240
	1-11	70	Residual	5.1	46	11	43	1260
	1-12	80	0	2.5	40	27	33	1150
	1-13	80	0.15	2.7	41	24	35	1155
	1-14	80	0.3	3	43	21	36	1161
	1-15	80	0.5	3.6	45	18	37	1240
	1-16	80	Residual	5.4	49	11	40	1182
	1-17	90	0	2.7	43	26	32	1095
Sand 2	2-1	40	Residual	4.8	34	9	57	1608
	2-2	50	Residual	5.3	39	9	52	1478
	2-3	60	Residual	5.7	43	9	48	1369
	2-4	70	Residual	6.1	46	9	45	1276
Sand 3	3-1	45	0.3	2.2	30	25	45	1438
	3-2	45	0.5	2.6	32	20	48	1465
	3-3	45	0.7	3.4	34	15	51	1497

3-4	54	0.3	2.4	34	24	42	1353
3-5	54	0.5	2.9	36	19	45	1374
3-6	54	0.7	3.7	38	14	47	1398
3-7	63	0.3	2.6	37	23	40	1279
3-8	63	0.5	3.1	39	19	42	1294
3-9	63	0.7	4.0	42	14	44	1312
3-10	50	Residual	7.2	39	6	55	1511
3-11	60	Residual	7.5	43	7	50	1399
3-12	70	Residual	7.8	47	7	47	1303
3-13	80	Residual	8.0	50	7	43	1220
3-14	90	Residual	8.2	52	7	41	1148
3-15	100	Residual	8.3	54	7	38	1084

* “Residual” means that all pore water except the absorption water is replaced by foam infiltration

4.3.2 Set-up and procedure

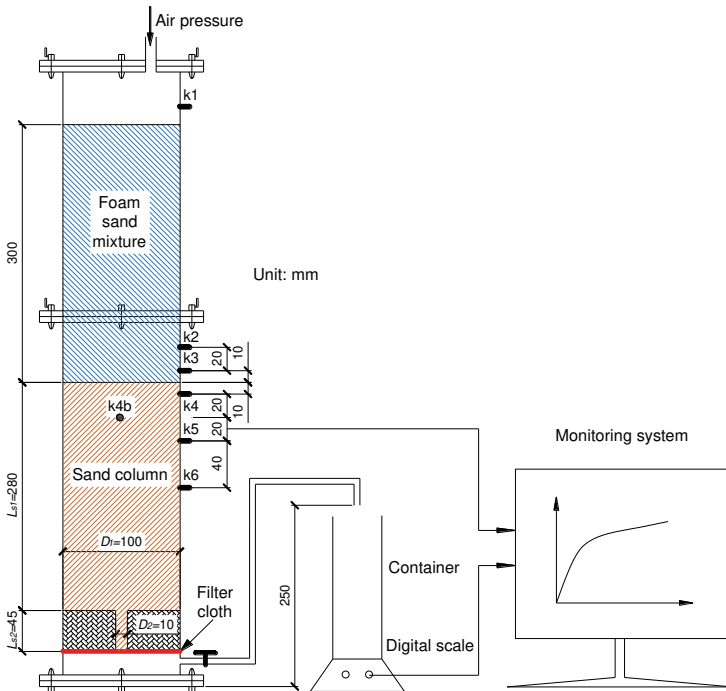


Figure 4-4. Schematic view of the experimental set-up.

The experimental set-up used in this test series is the same as the set-up used in Chapter 2, except the foam was replaced with the foam-sand mixture on top of the saturated sand and the location of the modified pore pressure transducers. Schematic view of the set-up is shown in Figure 4-4. k_1 in the top of the cylinder measures the applied air pressure, k_2 and k_3 measure the pore water pressure in the mixture, and k_4 , k_5 and k_6 measure the pore water pressure in the saturated sand. An extra pressure transducer k_{4b} is used in the tests of 3-1 ~ 3-9 which is in the middle of k_4 and k_5 .

The preparation of the sand sample was the same to that in Chapter 2. The remaining water on top of the sand column is carefully removed by a syringe. The foam is first produced at atmospheric pressure and then pressurized during the test at an absolute pressure of 1.5 bar. According to Boyle's Law the following relation can be obtained:

$$FER_p = \frac{p_a}{p} (FER_a - 1) + 1 \quad (4-1)$$

where FER_p is the FER at the desired air pressure, FER_a the FER at atmospheric pressure, p_a the atmospheric pressure and p the desired air pressure (total pressure: atmospheric plus excess pressure).

According to Equation (4-1), to get a FER 10 at 1.5 bar, the FER should be 14.5 at atmospheric pressure.

The foam-sand mixture is mixed manually until it reached a homogenous state and placed on top of the sand column. An air pressure of 50 kPa is then applied and the experiment starts after the bottom valve is open and the discharged water and pore pressures are recorded every second. The test duration is 4500 seconds (75 min) that is comparable to the standstill time during ring building (Broere & van Tol, 2001). The measurement also stops when the discharge becomes large, caused by the fracturing of air into the medium.

4.4 Results

4.4.1 Discharge

Figure 4-5 shows that there is still some foam infiltration area due to bubble penetration, although the foam front is not quite parallel to the mixture-sand boundary,

it suggests that an infiltration area has been realized.

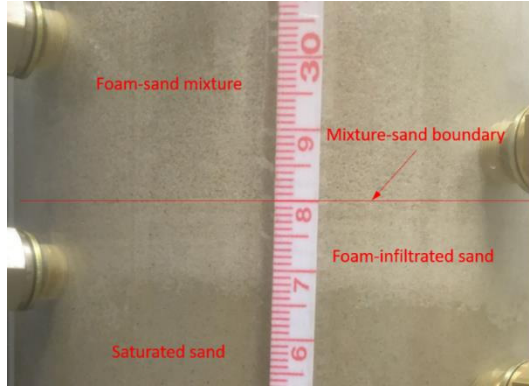


Figure 4-5. Image of the different areas due to foam infiltration 35 minutes after test started (test No. 1-11).

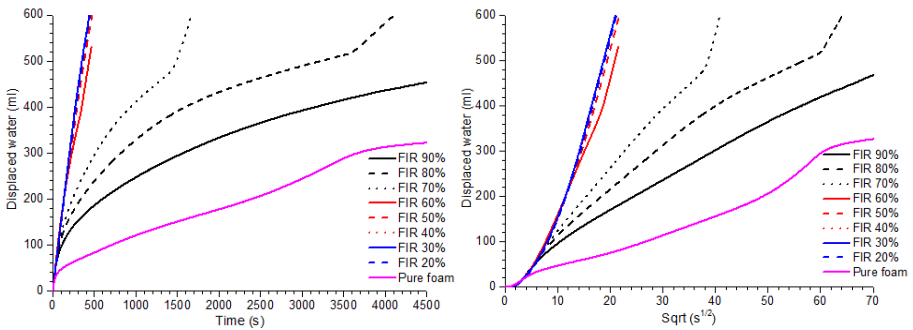


Figure 4-6. Volume discharge against time (a) and square root of time (b) in tests with Sand 1 (different FIR and 0% pore water replacement).

Figure 4-6 shows the discharged water with various FIRs at 0 Vol % pore water replacement in Sand 1. It is found that with a low FIR (< 60 Vol %), the discharge is merely a water flow with a constant flow resistance, the resistance of the sand. When $FIR \geq 70$ Vol %, the discharged water shows a similar pattern as in pure foam experiment. To better compare, the measured volume of water was replotted as a function of square root of time (Figure 4-6b) to examine if there is a comparable consolidation process as in a slurry infiltration.

After the initial fast discharge that is still dominated by flow resistance of the water in the sand and thus follows the same curve for all tests, there is a linear relation

between the expelled volume and square root of time. This linear relation suggests that there is an increase in thickness of a low permeable layer over time. Moreover, the discharge rate will decrease with an increasing FIR, suggesting that increasing the FIR will result in less water leakage with less pressure drop in the excavation chamber. Comparing with the results from the pure foam tests shown in the figure, it can be concluded that mixing the saturated sand with foam will result in more water discharge. Most likely, the increased water discharge comes from the pore water in the mixture.

It should be noted that there is an increase in water discharge at the later stage of some tests due to fracture of air (for example FIR 80 Vol % at around 3600 s). Because fracture of air is not a possible condition that could happen in tunneling during standstill, the increase in discharge will not be discussed anymore.

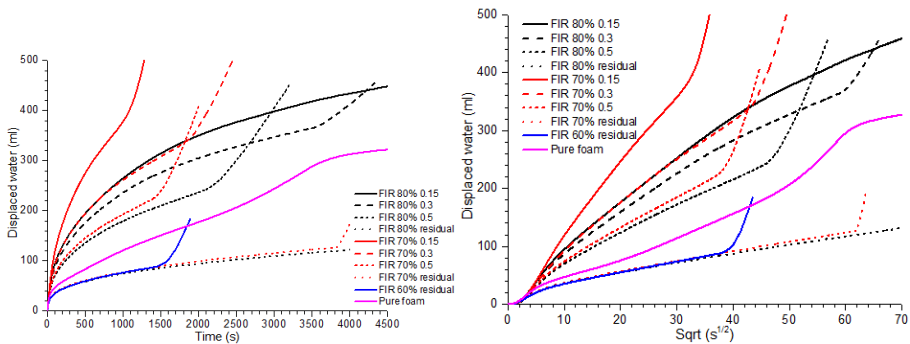


Figure 4-7. Volume discharge against time and square root of time in tests with Sand 1 (different FIR and different pore water replacement ratio).

Figure 4-7 shows the discharged water with different FIRs and different water content of the mixture in Sand 1. The results show that with the same remaining water content, the discharge rate will decrease with an increasing FIR, which is similar to what was found in Figure 4-6. With the same FIR, the discharge rate will decrease with a decreasing remaining water content in the foam-sand mixture. This may be attributed to the low permeability of the layer that is thickening with elapsed time. The ‘determining layer’ is lower in permeability with decreasing water content of the mixture. The slope of the linear section against square root of time becomes smaller as a consequence.

It should be noted that at residual water content, the discharge rate as well as the discharged volume are more or less the same in tests for different FIR, because now the discharged water comes from the foam used to make the foam-sand mixture. Either foam flow or foaming liquid flow is the responsible for the discharge. Figure 4-7 indicates that both increasing the FIR and reducing the remaining water content in the excavated soils can be beneficial in achieving less water leakage which will result in a slower pressure drop in the excavation chamber during standstill. The discharge for pure foam is in general between the condition with residual water content and with limited water content. An interesting point is that the discharge is larger in pure foam condition than mixed with almost dry sand, indicating that adding sand grains in the foam could result in less water leakage. However, the influence from the sand fraction was not so clear and should be further examined.

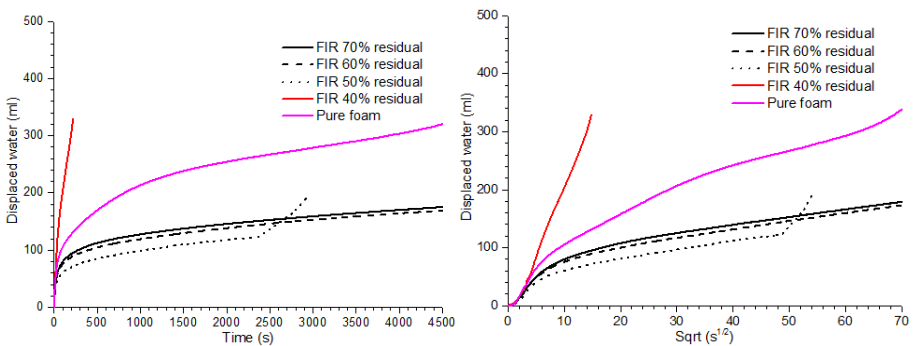


Figure 4-8. Volume discharge against time and square root of time in tests with Sand 2 (at residual water content).

Figure 4-8 shows the discharged water volume with various FIRs at residual water content in Sand 2. The discharge pattern is similar to that in a pure foam infiltration when $\text{FIR} \geq 50 \text{ Vol } \%$. At $\text{FIR} \geq 50 \text{ Vol } \%$, water leakage will be reduced after the initial fast discharge, and the water discharge will be linear against square root of time. The slope of the linear section against square root of time while the total amount of water discharge will increase with increasing FIR.

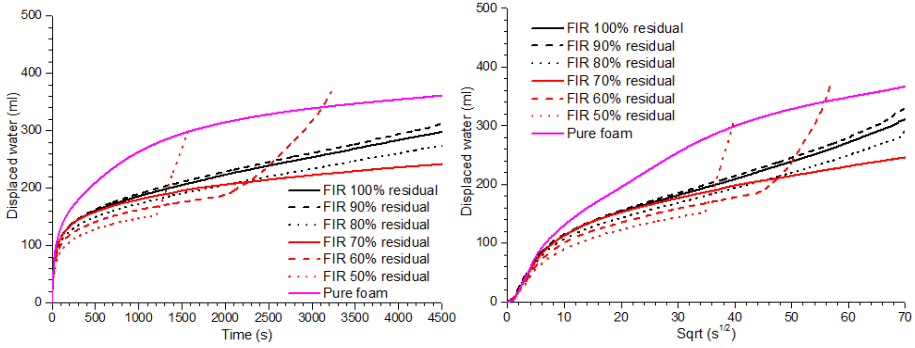


Figure 4-9. Volume discharge against time and square root of time in tests with Sand 3 (at residual water content).

Figure 4-9 shows the discharged water with various FIRs at residual water content in Sand 3. Water leakage reduced after the initial fast discharge in all tests. During the reduced discharge period, the flow behavior is similar to that in a pure foam infiltration. The water discharge will increase with increasing FIR. At $FIR \geq 80$ Vol %, the increase in discharge is not clear.

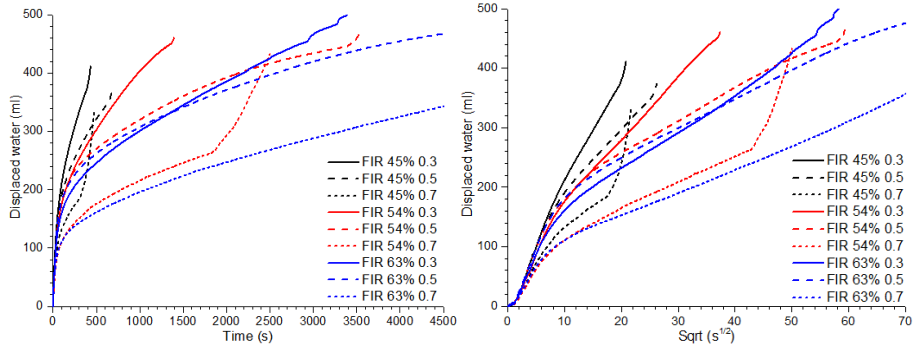


Figure 4-10. Volume discharge against time and square root of time in tests with Sand 3 (different FIR and different pore water replacement ratio).

Figure 4-10 shows the discharged water with different FIRs and different water content of the mixture in Sand 3. Water leakage reduces after the initial fast discharge in all tests and linear relation between the expelled water and square root of time. While the slope of the linear section varies in different tests. With the same FIR, the slope is smaller at a higher pore water replacement ratio (a lower water content). While at the same pore water replacement ratio, the slope is smaller at a higher FIR. It

suggests that both decreasing the water content and increasing the FIR result in a less water leakage with less pressure drop in the excavation chamber.

A possible reason for fracture of air is attributed to the change in the porosity of the mixture. As stated in the introduction part, the injection of foam will result in a mixture with a porosity higher than the maximum porosity. The pressure will be a fluid pressure in the mixture since there is no grain contact. A fluid pressure is isotropic, therefore air couldn't penetrate in a laminar flow condition (which is a slow flow in our tests). However, with ongoing water leakage, the porosity of the mixture decreases and grain contacts become possible. Effective stress develops and the pressure inside the mixture becomes anisotropic. The vertical pressure exceeds the horizontal pressure and the mixture will get fractured by the applied pressure.

The final porosity of the mixture at which the fracture of air occurred from the experimental results could provide some theoretical basis for this explanation. The initial porosity of the mixture is higher than the maximum porosity of the sand, suggesting there is no effective stress. As the water is expelled, the porosity of the mixture becomes smaller. Effective stress develops when its porosity reaches the maximum porosity of the sand and fracturing of the mixture by air is possible after that. The porosity of the mixture as a function of time is calculated assuming the volume decrease in the mixture is related to the expelled water. An upper bound is the foam loss due to foam infiltration since foam bubbles will expand at a lower pressure, and a lower bound with no foam penetration but there is only water loss.

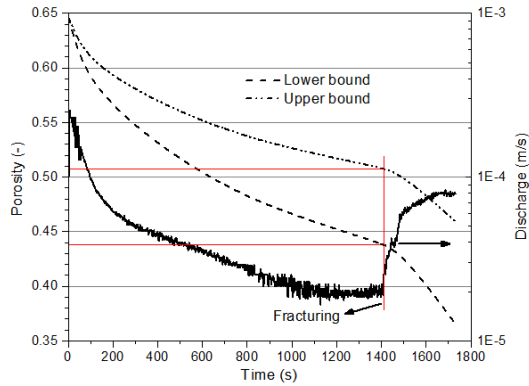


Figure 4-11. Calculated porosity of the mixture and discharge rate as a function of time (Sand 1 FIR 70 Vol %).

Figure 4-11 shows an exemplary plot of the calculated porosity as a function of time. Measured discharge is also included to distinguish the fracturing of the mixture by air (at around 1400 s). The corresponding upper and lower values for porosity are recorded for comparison with the maximum porosity of the sands. Values in different tests are listed in Table 4-3.

Table 4-3. Values found in different tests

Number	Upper value	Lower value	$n_{max} (-)$
1-5	0.505	0.448	0.47
1-7	0.508	0.448	0.47
1-8	0.517	0.458	0.47
1-9	0.512	0.46	0.47
1-10	0.528	49	0.47
1-11	0.538	0.515	0.47
1-12	0.514	0.439	0.47
1-13	0.515	0.443	0.47
1-14	0.528	0.471	0.47
1-15	0.544	0.504	0.47
3-1	0.468	0.417	0.48
3-2	0.499	0.452	0.48
3-3	0.465	0.441	0.48
3-4	0.468	0.406	0.48
3-5	0.467	0.407	0.48
3-6	0.476	0.460	0.48
3-7	0.495	0.433	0.48
3-11	0.445	0.414	0.48

Table 4-3 shows that in most tests with Sand 1, the maximum porosity of Sand 1 lies within the range between the upper and lower values of the calculated porosity. While it is close to the upper values in most cases of Sand 3. The overall match shows good agreement between theoretical and experimental results, considering that the calculated values are just average porosity of the mixture. The general agreements are in support of the mechanism for fracturing.

4.4.2 Pressure

The linear relation between water discharge and square root of time after the initial fast discharge in this series of tests is similar to that in a pure foam infiltration shown in Chapter 2. This suggests that there is an increase in a low permeable layer over time. The low permeable layer is the foam-infiltrated sand in the case of pure foam infiltration, while it remains unclear for sandy foam infiltration. The measured pore

pressures at different locations could provide some information and therefore were analyzed.

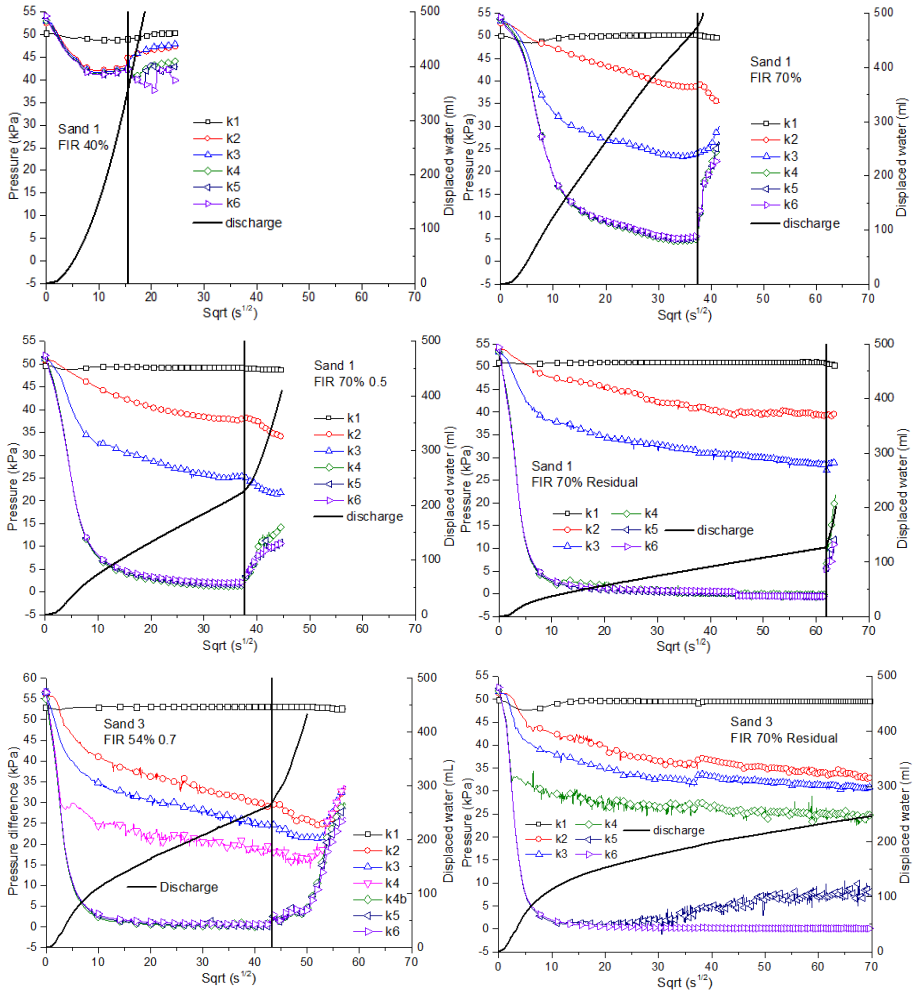
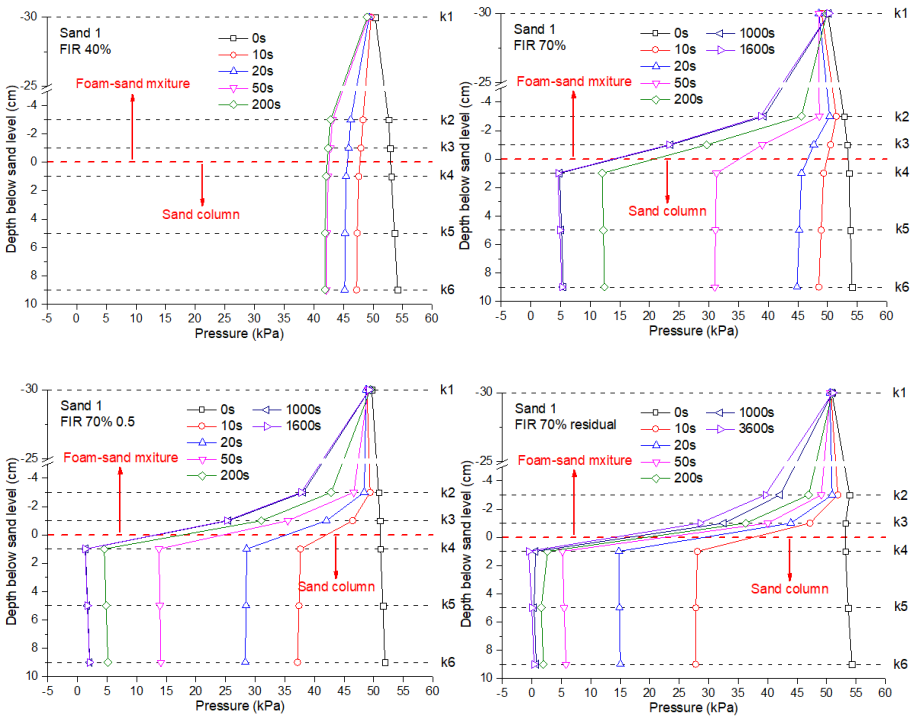


Figure 4-12. Measured pore pressures and discharge volume as a function of square root time in different tests.

Figure 4-12 shows the measured pore pressures and the discharged volume as a function of square root of time in different tests. The black line indicates the time point when fracture of air happens and therefore only the results on the left-hand side of the black line in each figure are of interest. As shown in the above section, the results in Figure 4-12 covers the transition from pure water discharge (Sand 1 – FIR 40 Vol %) to effective plastering (Sand 3 – FIR 70 Vol % residual). It shows that the pore

pressures in the saturated sand is still large with a low FIR of 40 Vol %, indicating that there is no effective plastering during the test, and fracturing occurred right after all the mixture is consolidated. With a larger FIR of 70 Vol %, the pore pressure in the saturated sand is effectively lowered as a consequence of effective plastering. With the same FIR 70 Vol %, the increase in pore water replacement by foam infiltration (PWR at 0.5 and residual level) results in an increased plastering effect as the pore pressure in the saturated sand becomes even lower. Results from Sand 3 – FIR 54 Vol % PWR 0.7 and Sand 3 – FIR 70 Vol % residual also present that there is effective plastering as the pore water pressure in saturated sand reached steady values close to 0.



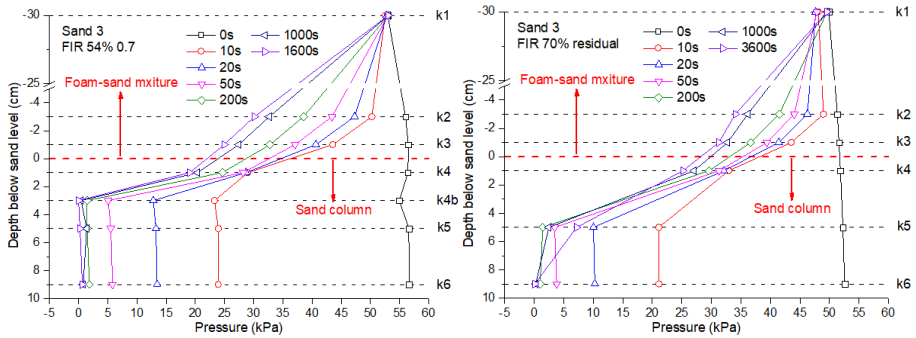


Figure 4-13. Pore water pressure distribution at different times as a function of location in different tests.

Figure 4-13 shows the measured pore pressure as a function of depth at different times in different tests. In general, there is a linear distribution of the pore pressure prior to the start of the test due to the hydrostatic pressure. The pore pressure shows various degree of decrease at different locations when the test started, and the decreasing trend continued with elapsed time. In the test with Sand 1 – FIR 40 Vol %, the decrease in pore pressure was not so obvious in the absence of the effective plastering. In this case, the pore pressure distributes linearly along the 5 m of the equivalent length of the sand column, which indicates that most pressure drop is concentrated in the small cylinder shown in Figure 4-4. While effective plastering is obvious in the other tests that most pressure drop occurred near the sand surface as shown in Figure 4-13. The pressure gradient of k2-k3 (slope of k2-k3) is similar to that of k3-k4 in the results with Sand 1 – FIR 70 Vol % after 1000 s, showing no significant signs of foam infiltration. However, with an increasing pore water replacement (Sand 3 – FIR 54 Vol % PWR 0.7 and Sand 3 – FIR 70 Vol % residual), the gradient of k3-k4 is exceeding the gradient of k2-k3 as shown in Figure 4-13, which is high likely induced by the foam infiltration effect. An extra pressure transducer k4b in the test with Sand 3 – FIR 54 Vol % PWR 0.7 shows that the gradient of k4-k4b can be even higher than the gradient of k3-k4, showing that the permeability is smallest in the foam infiltrated sand. In the test with Sand 3 – FIR 70 Vol % residual, the pore pressure measured by k6 continued to decrease from 200 s to 3600 s while k5 showed an increasing trend, suggesting that k5 has been influenced by foam infiltration.

Figure 4-13 suggests that the plastering effect (which is the formation of a low

permeable layer) is influenced by both the FIR and the remaining water content of the mixture. Since the foam infiltration phenomenon is of interest, the mechanisms during foam infiltration are studied in detail.

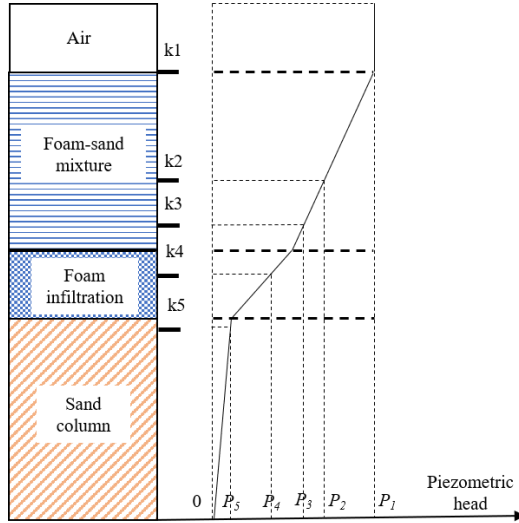
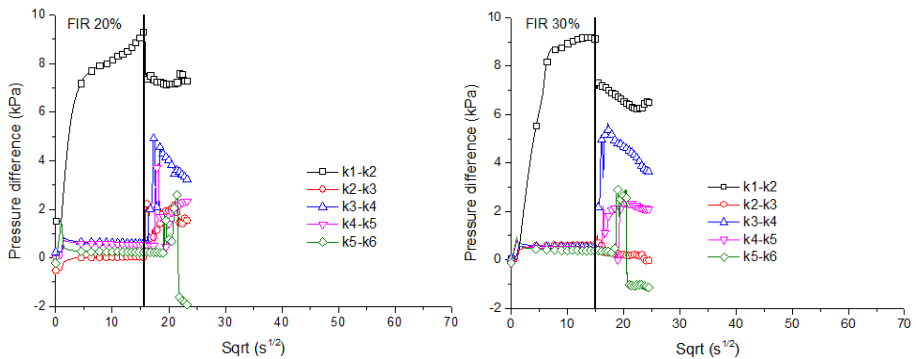


Figure 4-14. Distribution of piezometric head at different locations during sandy foam infiltration.

Figure 4-14 shows the distribution of piezometric head at different locations during sandy foam infiltration. The loss of foam of water from the mixture to the saturated sand results in a consolidation of the mixture, which results in a certain pressure drop in the mixture. While the foam infiltration area has a lower permeability that pressure gradient in that area is the largest in the whole system.



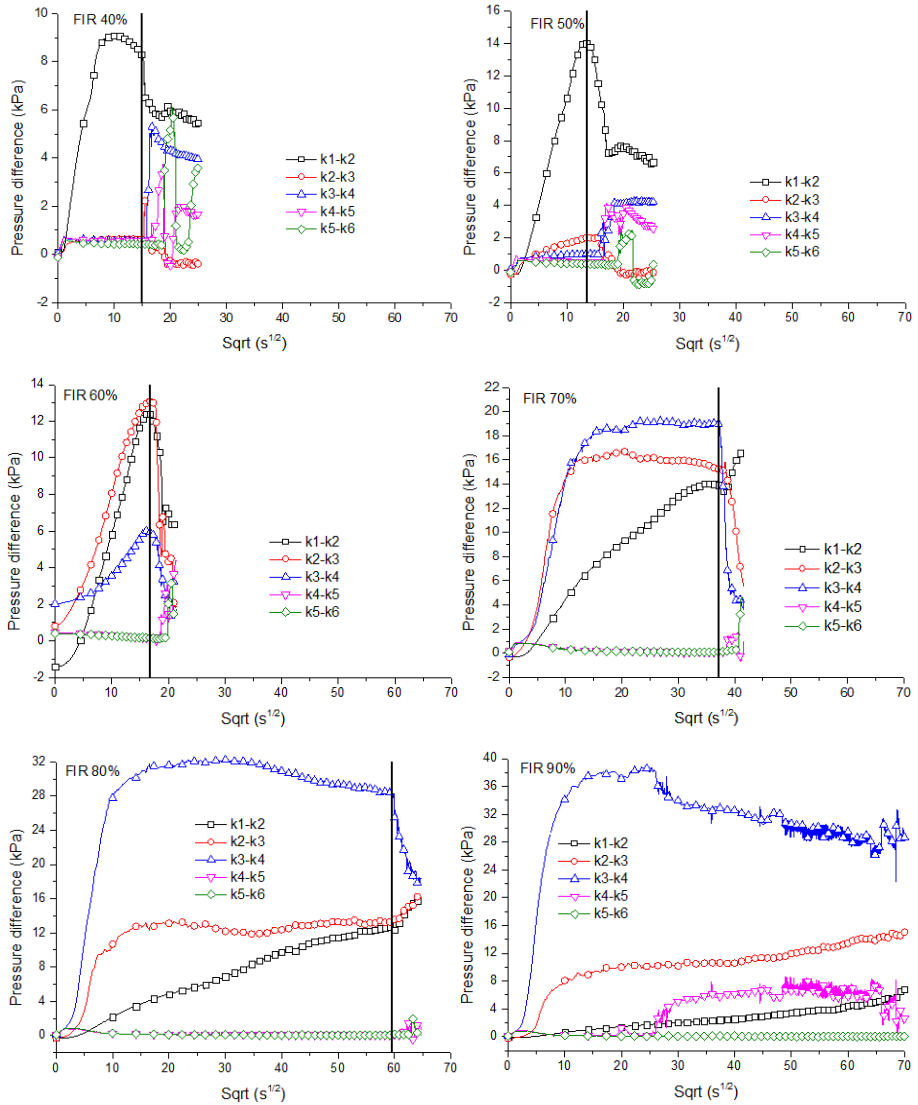
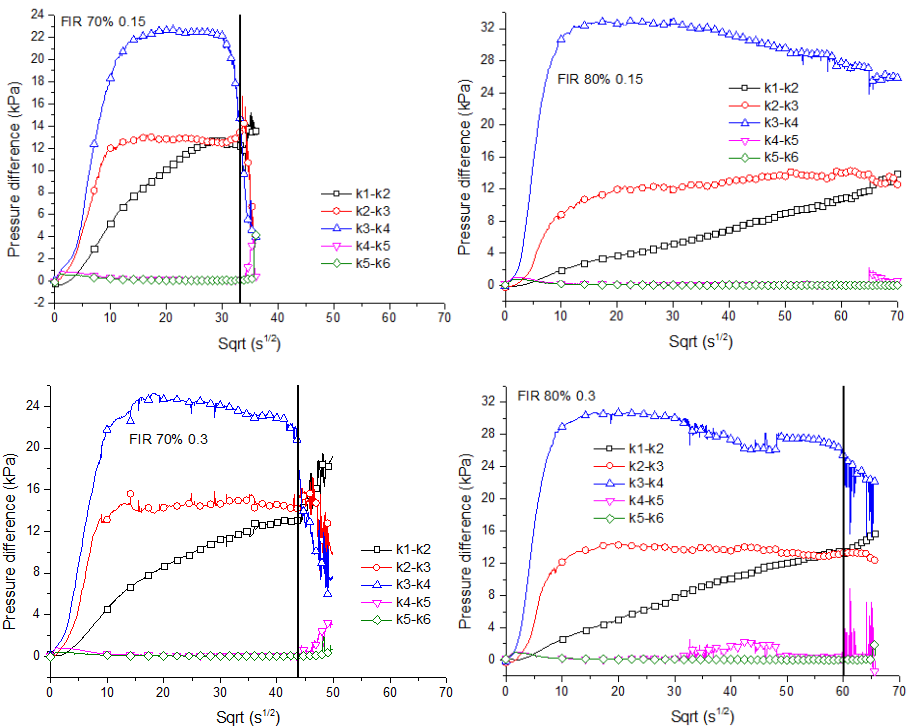


Figure 4-15. Pressure difference in Sand 1 (different FIR and 0 pore water replacement)

Figure 4-15 shows the pressure difference as a function of square root of time with various FIRs at 0 pore water replacement in Sand 1. Figure 4-15 shows that the major pressure drop is taken by the sand in the small cylinder where the flow resistance is high for FIR < 60 Vol %. With a FIR larger than 60 Vol %, the pressure drop between k2 and k3 (k2-k3) builds up and surpasses the pressure drop between k1 and k2 (k1-k2). Indicating that there is a consolidation process of the mixture near the sand

surface. In the tests with FIR 70 Vol % ~ 90 Vol %, there is a linear increase against square root of time in k1-k2, in correspondence with the linear discharge against square root of time shown in Figure 4-6b. This may indicate that there is an increased depth of the consolidated layer of the mixture which has a low permeability. While the water in the mixture continues to be pressed out of the mixture, and consolidation process goes on as a consequence.

Moreover, k3-k4 starts to increase at FIR 60 Vol % and it becomes larger than k2-k3 at FIR 70 Vol %. With a higher FIR, k3-k4 presents an increasing trend, as it increases from about 19 kPa to 32 kPa and 38 kPa when FIR increases from 70 Vol % to 80 Vol % and 90 Vol %, respectively. At FIR 90 Vol %, k3-k4 decreases at around $25 \text{ s}^{1/2}$, while k4-k5 increases simultaneously. Indicating that there is pressure redistribution between k3 and k5 due to foam penetration. More will be analyzed in section 4.4.3.



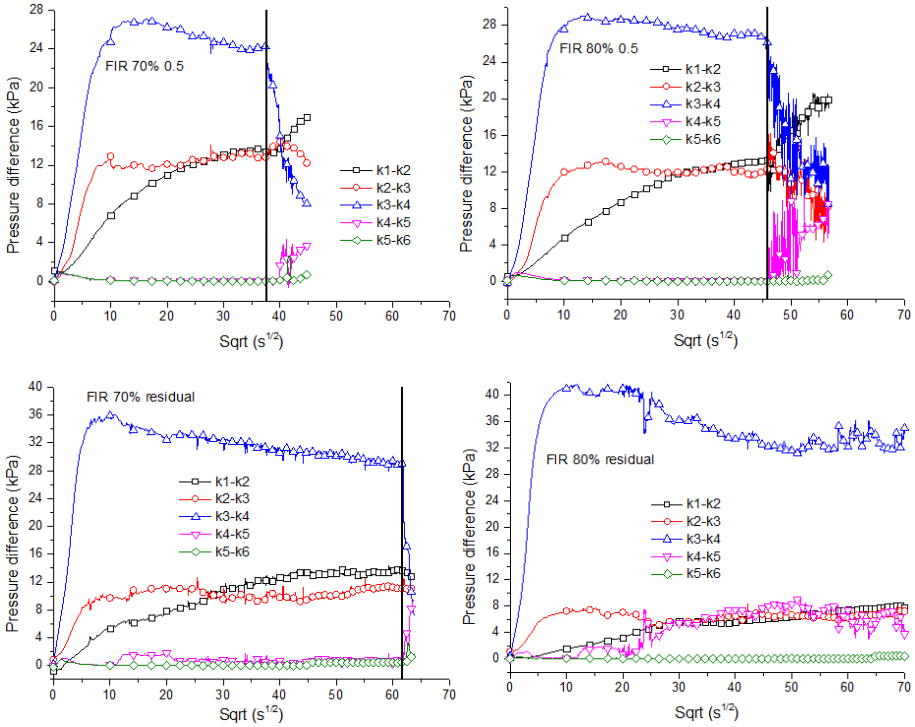


Figure 4-16. Pressure difference in Sand 1 (different FIR and different pore water replacement)

Figure 4-16 shows the pressure differences between adjacent pressure transducers at different locations in tests with Sand 1 different FIR and different pore water replacement. Again, the linear increase in k1-k2 against square root of time is in correspondence with the linear part shown in Figure 4-7b. While the pressure drop of k3-k4 remains more or less constant after the initial fast discharge period. The stable values of k3-k4 after initial fast discharge increases when FIR increases from 70 Vol % to 80 Vol %, in line with the results shown in Figure 4-15.

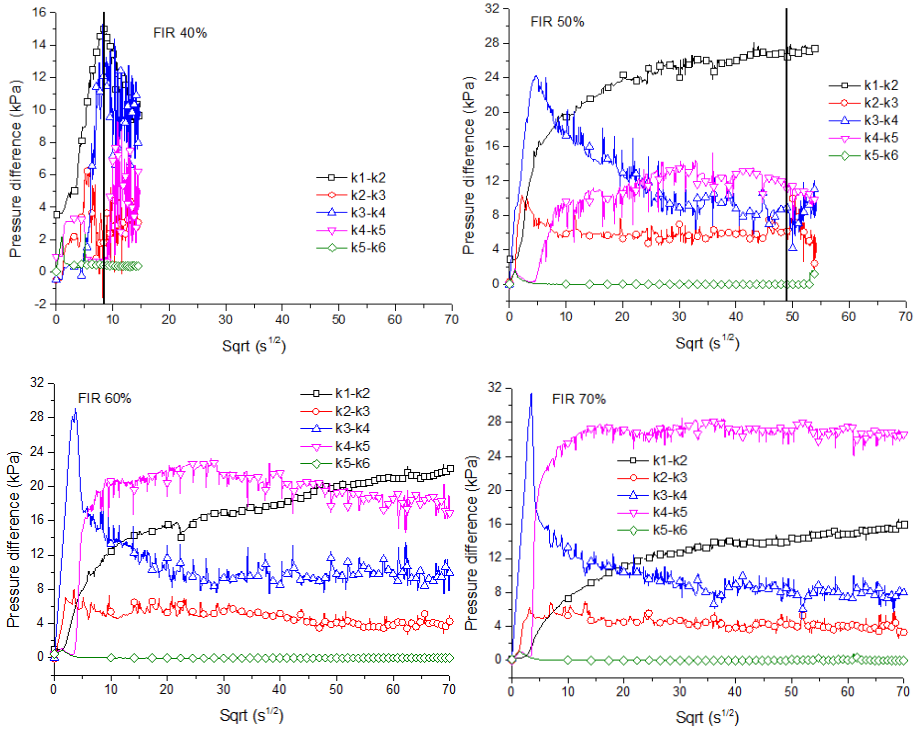


Figure 4-17. Pressure difference in Sand 2 (different FIR at residual water content)

Figure 4-17 shows the results with Sand 2 at residual water content. With a low FIR 50 Vol %, most of the pressure drop is maintained in the consolidated mixture (k1-k2) while more pressure drop over the foam infiltrated sand (k4-k5) at FIR 70 Vol %. Indicating more pressure drop over the foam infiltrated area can be realized with a higher FIR. Figure 4-17 also indicates the pressure drop is primarily maintained in the foam infiltrated sand (instead of the consolidated mixture). There can hardly be any low permeable layer formed due to either consolidation of the mixture or foam infiltration at a low FIR. Effective stress develops in the mixture as a consequence. This should be avoided.

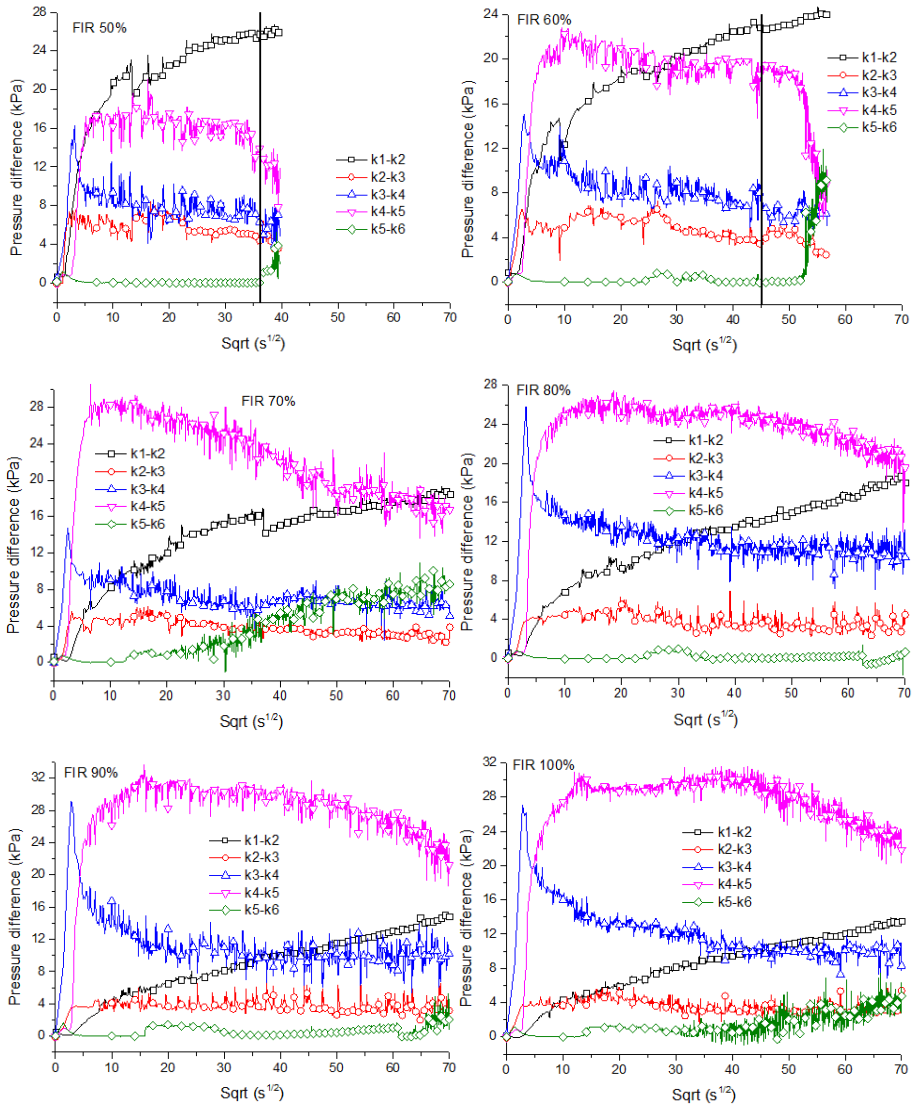
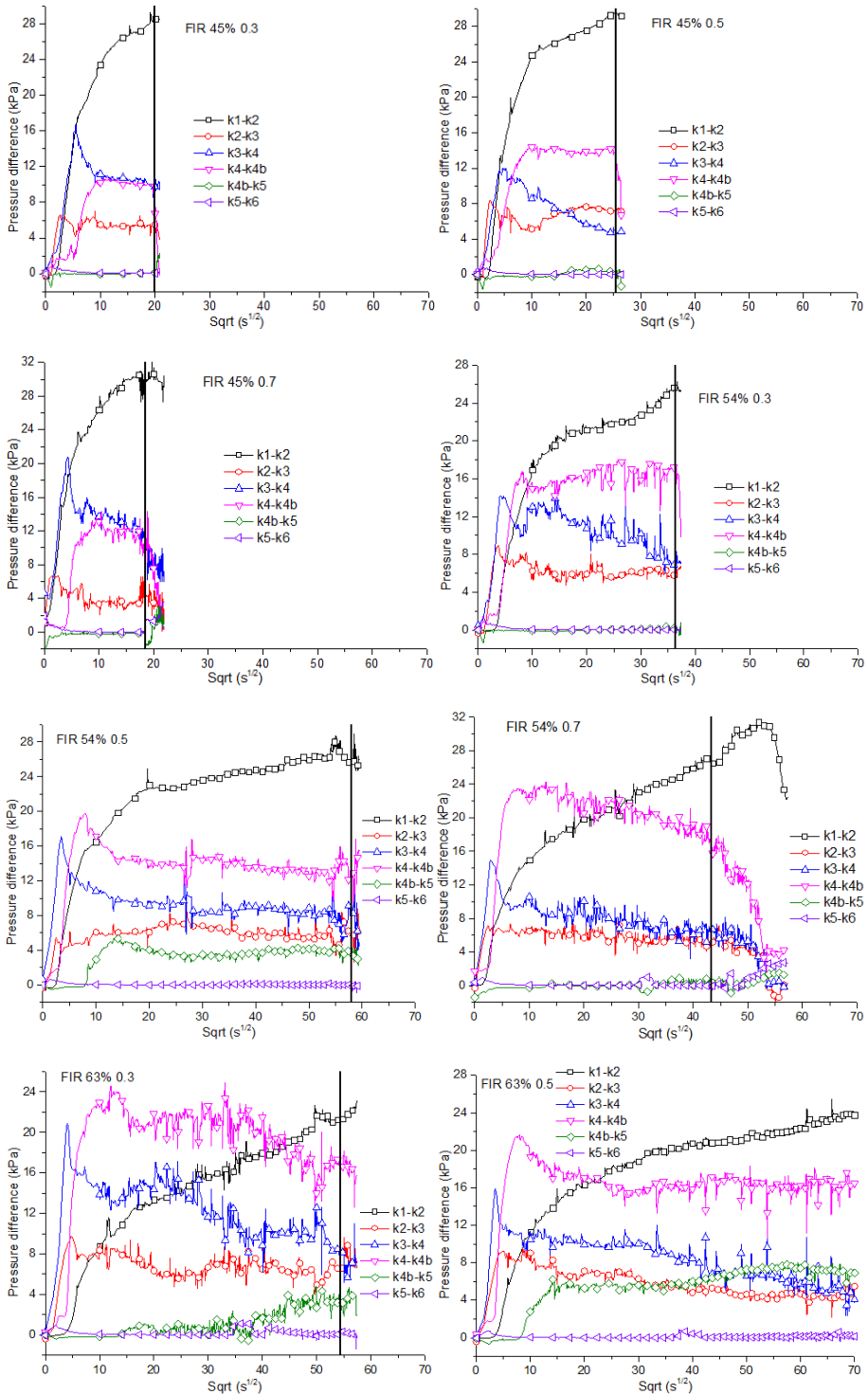


Figure 4-18. Pressure difference in Sand 3 (different FIR at residual water content)

Figure 4-18 shows the results in Sand 3 with different FIR at residual water content. In general, it presents similar results with Figure 4-16. There is a linear increase in k1-k2 against square root of time in relation to the linear discharge against square root of time shown in Figure 4-9b. The pressure drop is primarily maintained in the foam infiltrated sand when FIR > 50 Vol %.



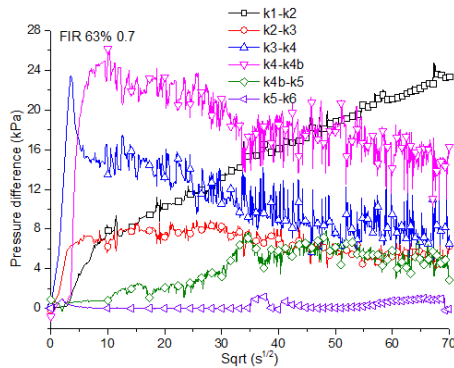


Figure 4-19. Pressure difference in Sand 3 (different FIR at different pore water replacement)

Figure 4-19 shows the results in Sand 1 with different FIR and different pore water replacement. In this test series, an extra pressure transducer k4b was placed in the middle between k4 and k5, so more information can be obtained regarding the foam flow in the sand. It is shown that a large proportion of excess pore pressure is taken by the consolidated mixture. Linear increase in k1-k2 against square root of time after the initial fast discharge is also present in these tests. Owing to the consolidation process of the mixture, the discharge is linear against square root of time as shown in Figure 4-10b.

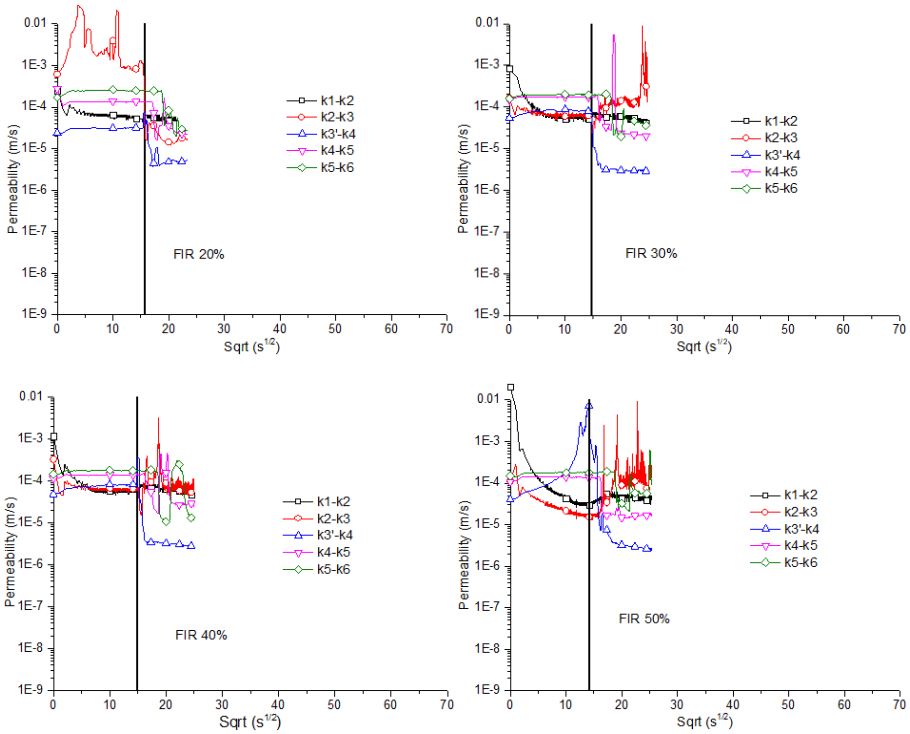
4.4.3 Permeabilities

The permeability of the foam-sand mixture as well as the sand can be calculated by the measured pressures at different locations and the water discharge. It is calculated according to Darcy's law:

$$k = \frac{\Delta L Q}{A_C \Delta \phi} \quad (4-2)$$

With ΔL the distance between two adjacent pressure transducers, Q the measured water discharge, A_C the cross-sectional area of the sand column and $\Delta \phi$ the corresponding difference in piezometric head between adjacent pressure transducers. The permeability of the foam-sand mixture can be calculated with k1 ~ k3. The thickness of the mixture (ΔL) between k1 and k2 is 27 cm and between k2 and k3 is 2 cm. Although the thickness of the mixture between k1 and k2 will decrease due to the drainage, the change is only limited compared with 27 cm. For example, the height

loss at the end of test 3-7 is 4.8 cm, which is 18% of 27 cm, and its influence on the calculated permeability k_{1-2} is negligible. For k_{4-5} and k_{5-6} this distance is 4 cm. Because Figure 4-15 ~ Figure 4-19 show that there is foam infiltration, the permeability of the consolidated mixture may be different to that of the foam infiltrated sand. Assuming there is a linear distribution of pore water pressures between k_2 and the sand surface, the pore pressure at the sand surface (k_3') can be deducted with the values measured by k_2 and k_3 . The permeability of the sand layer between the mixture-sand boundary and k_4 is also calculated using k_3' and k_4 with the distance of 1 cm. The calculations were carried out with all the measurement data.



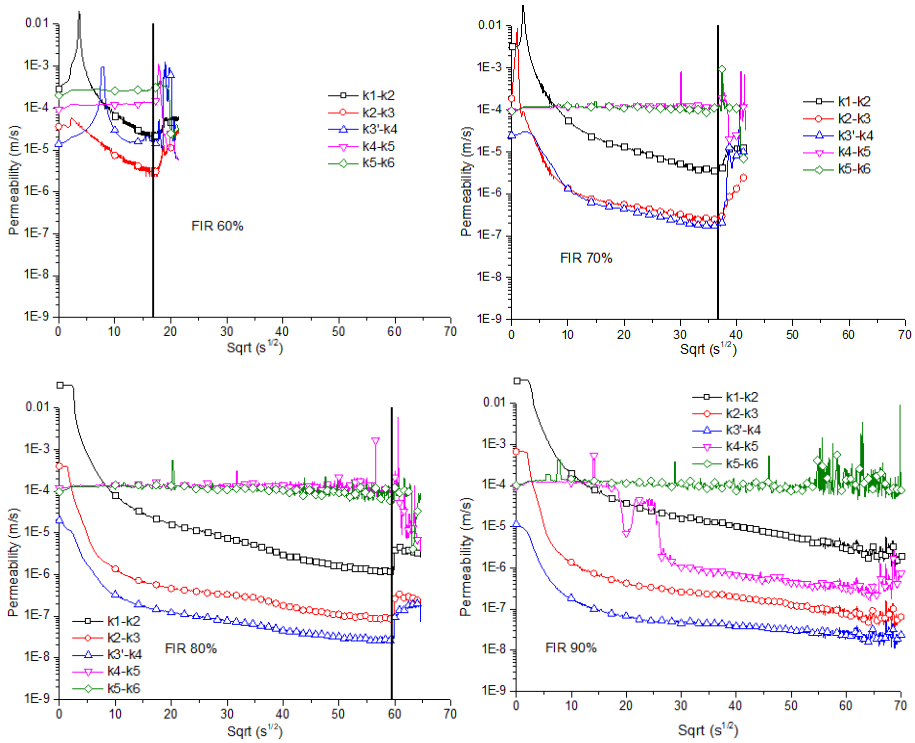


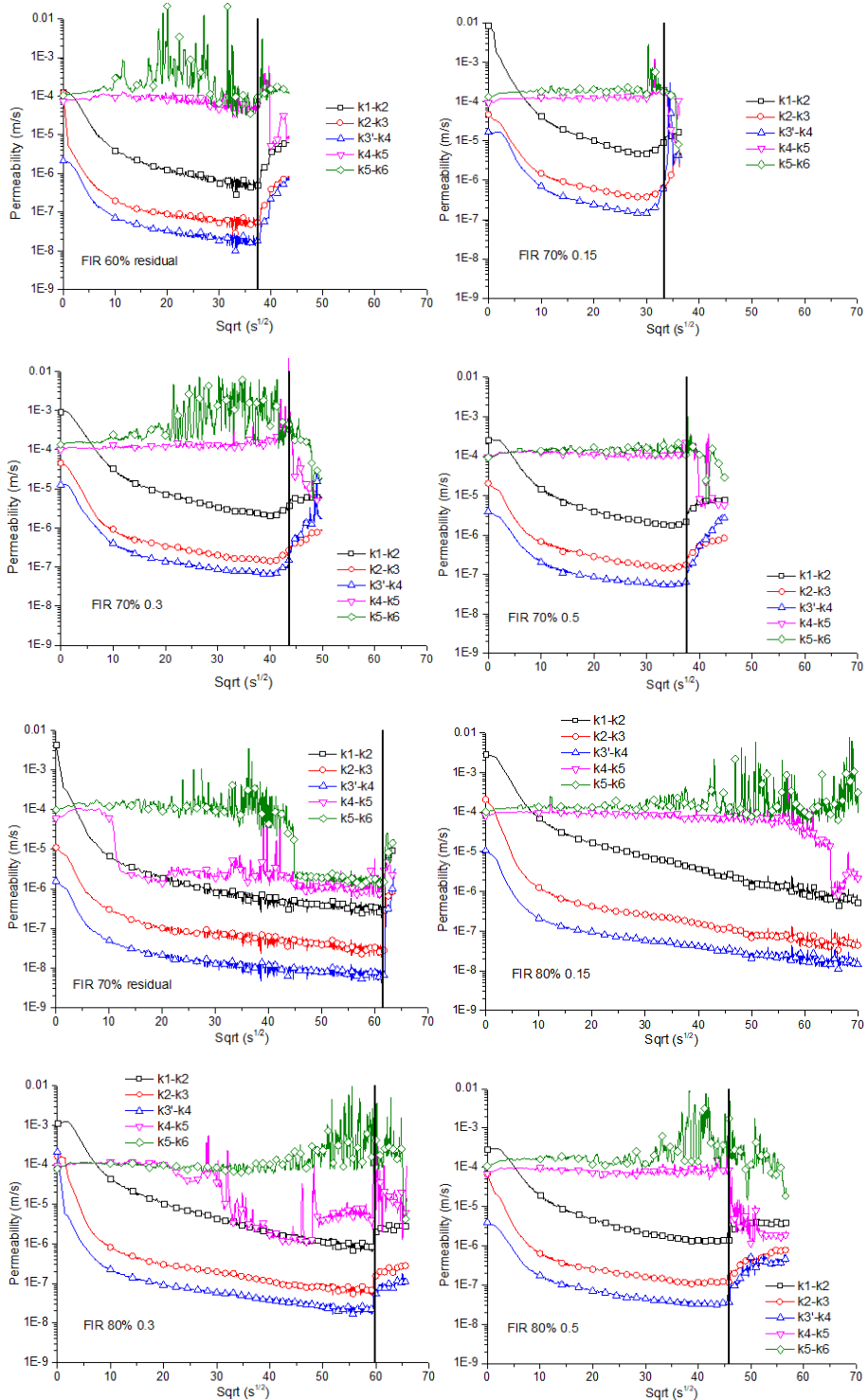
Figure 4-20. Calculated permeabilities in Sand 1 (different FIR and 0 pore water replacement)

Figure 4-20 shows the calculated permeabilities in tests with Sand 1 at different FIR. It shows there is no significant change in the sand permeability either in the mixture or in the original sand when FIR is smaller than 50 Vol %, because all the calculated permeabilities at different locations are close to the permeability of the sand sample. Water leakage from the mixture will be too fast in this case that effective stress will build up quickly and should be avoided in field applications. Besides that, the stability of the tunnel face may not be successfully maintained as the excess pore pressure will dissipate quickly. Therefore, the FIR larger than 50 Vol % is recommended in this soil condition.

The permeability of the foam infiltrated layer (k_{3-4}) is the smallest in the whole system when $FIR \geq 70$ Vol %. Particularly, in tests with FIR 90, the foam bubbles have infiltrated into the sand layer sandwiched by k_4 and k_5 , lowering k_{4-5} as a consequence. This indicates that the infiltration depth by the foam bubbles is larger than 1 cm. Further infiltration into the sand layer sandwiched by k_5 and k_6 is not observed from

k_{5-6} . While in tests with FIR less than 90, the infiltration depth by the foam bubbles is less than 1 cm. Also, when $40 \text{ Vol } \% < \text{FIR} < 70 \text{ Vol } \%$, the permeability of the whole system is controlled by the consolidated mixture as k_{2-3} is the smallest in the whole system. It should be noted that before the foam bubbles infiltrate into the sand pores, the calculated values by Equation (4-1) should reflect the permeability of the sand sample. Figure 4-20 shows that there is a general agreement when comparing the sand parameters shown in Table 4-1.

$k_{3'-4}$ is increasing in the beginning in case of FIR 50 Vol % and 60 Vol %, which could be induced by the overestimation of k_3' at the early stage of the test. Because the consolidation of the mixture first happens in the first 1 cm near the sand surface and the actual pressure drop between k_3 and the sand surface is larger than calculated with k_2 and k_3 . The values of k_3' in this case will be larger than the actual value as a consequence. It is conjectured that there is limited foam penetration and it is an ongoing process. The foam penetration results in a lower value in k_4 . These possible conditions result in the rising trend in $k_{3'-4}$. These also influence the results in $\text{FIR} \geq 70 \text{ Vol } \%$ because there is a slow decrease in $k_{3'-4}$ in the beginning of each test. While it should be decreasing fast due to foam penetration in the beginning.



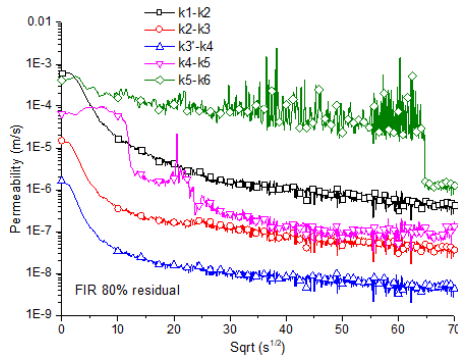


Figure 4-21. Calculated permeabilities in Sand 1 (different FIR and different pore water replacement)

Figure 4-21 shows the calculated permeabilities in tests with Sand 1 at different FIR as well as different pore water replacement. Although the consolidation of the mixture results in a low permeable layer as shown by k_{2-3} , the permeability of the whole system is controlled by the foam infiltrated area as k_{3-4} is the smallest in each test. Comparing this conclusion to that found in Figure 4-20, it is clear that reducing the remaining water content by foam infiltration in the excavated soils could help the formation of a low permeable area. Specifically, the infiltration depth by the foam bubbles seems to be influenced by the remaining water content in the mixture as the infiltration depth is bigger than 1 cm in FIR 80 Vol % 0.15, FIR 80 Vol % 0.3 and FIR 80 Vol % residual, and the time to reach 1 cm of infiltration depth is shorter with less remaining water content. However, this conclusion is not followed in the test with FIR 80 Vol % 0.5 as the infiltration depth is smaller than 1 cm. In the tests with FIR 70 Vol %, the infiltration depth is larger than 1 cm only at residual water level.

A further look into Figure 4-20 and Figure 4-21 shows that there is a good correspondence between the slow decrease in k_{2-3} and k_{3-4} in the beginning of each test, in favor of the speculations mentioned above.

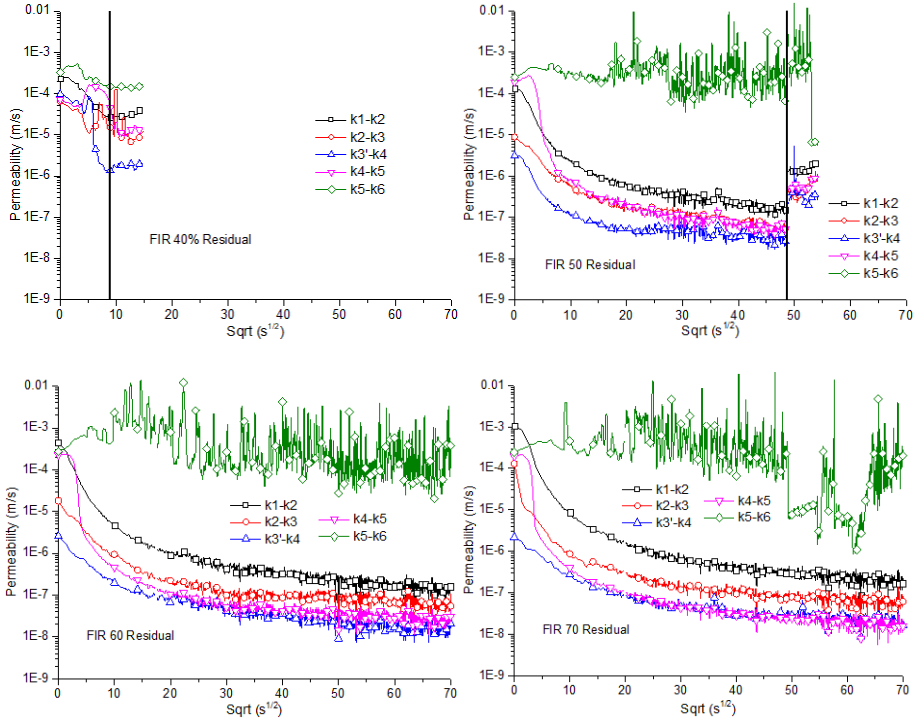
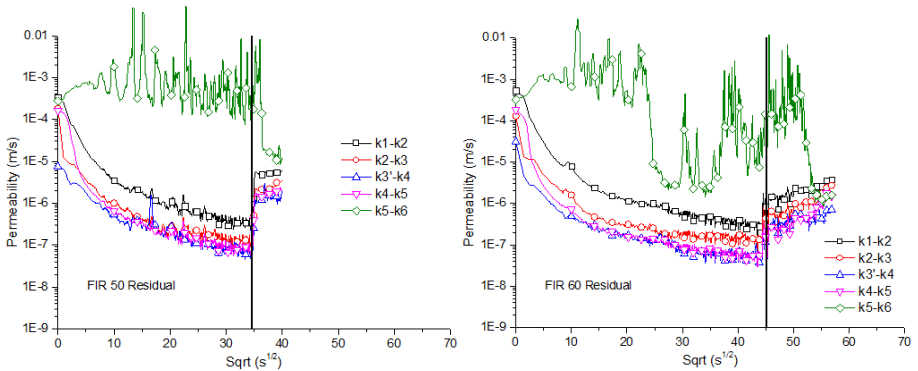


Figure 4-22. Calculated permeabilities in Sand 2 (different FIR at residual water content)

Figure 4-22 shows the permeabilities in tests with Sand 2 at residual water content. It shows that the permeability of the whole system is controlled by the foam infiltrated area as $k_{3'-4}$ and k_{4-5} are smaller than k_{2-3} at the later stage of the test. Specifically, the infiltration depth by foam bubbles is larger than 5 cm in FIR 70 Vol % as k_{5-6} is influenced by the foam bubbles at around 2300 s (48 s^{1/2}).



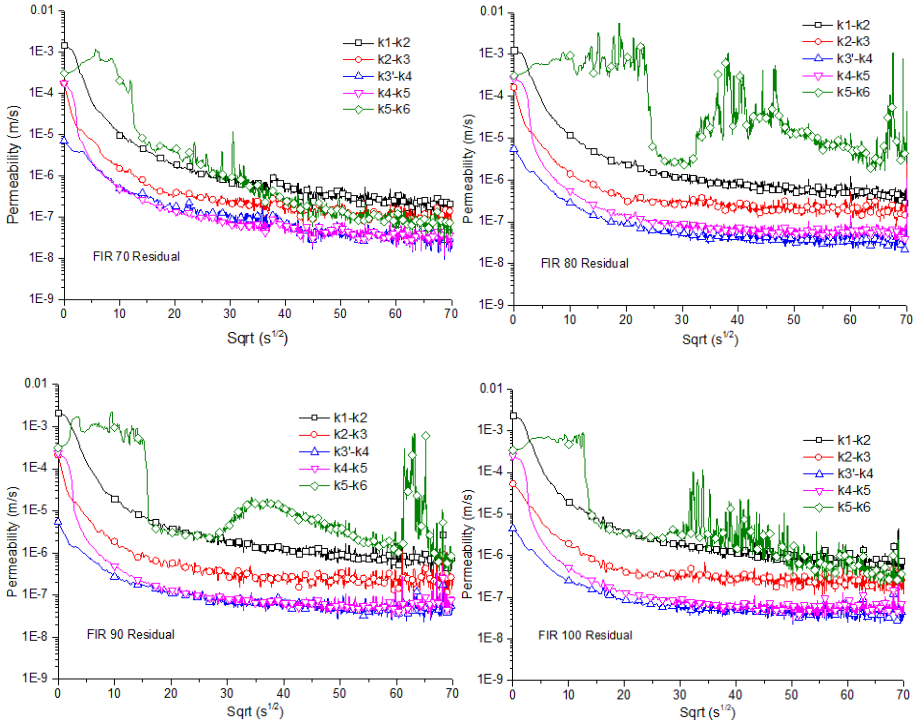
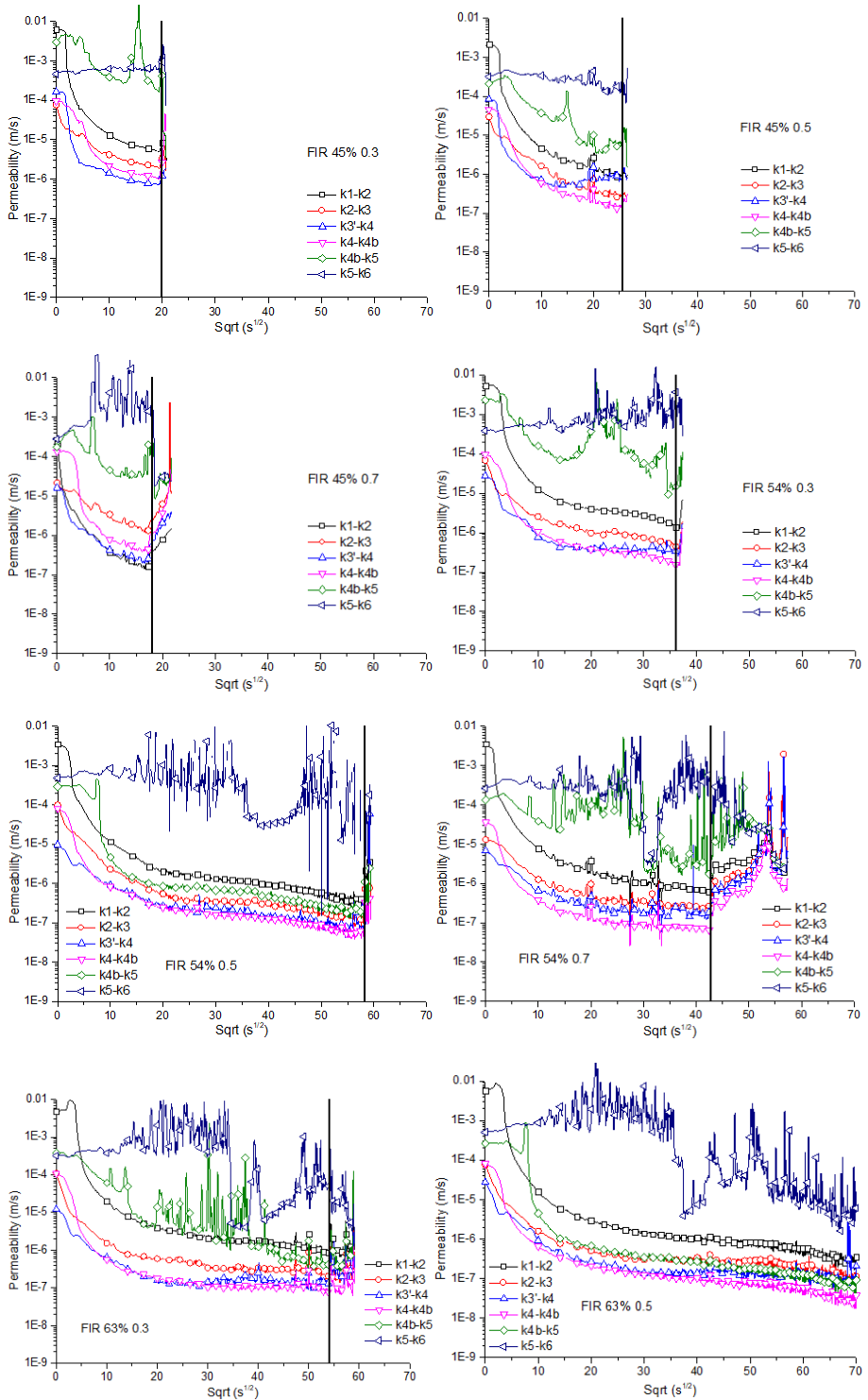


Figure 4-23. Calculated permeabilities in Sand 3 (different FIR at residual water content)

Figure 4-23 shows the calculated permeabilities in Sand 3 with different FIR at residual water content. It shows that the permeability of the foam infiltrated sand is smaller than the consolidated mixture, in line with the results in Sand 1 and Sand 2.



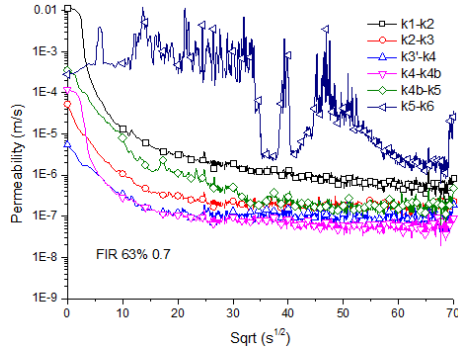


Figure 4-24. Calculated permeabilities in Sand 3 (different FIR at different pore water replacement)

Figure 4-24 shows the calculated permeabilities in Sand 3 with different FIRs at various levels of pore water replacement. It shows that the lowest permeability becomes smaller with a decreasing remaining water content in the mixture at the same FIR. The permeability is lowest in the foam infiltrated sand except in FIR 45 Vol % 0.3, which could be induced by measurement error.

Table 4-2 shows that the fractions of the three phases (air, liquid and sand) in this test series are different in each test and the results can be compared with those presented in Xu et al. (2020). In particular, the sand fraction is the same in test with FIR 45 Vol % 0.3 and FIR 54 Vol % 0.5, Figure 20 shows that the infiltration depth by foam bubbles is larger than 3cm at around 100 s ($10 \text{ s}^{1/2}$) in FIR 54 Vol % 0.5, while not clear in FIR 45 Vol % 0.3. Similar results can be found in tests with FIR 54 Vol % 0.3 and FIR 63 Vol % 0.5, that the infiltration depth is larger than 3cm in FIR 63 Vol % 0.5 before 100 s ($10 \text{ s}^{1/2}$) while not the case in FIR 54 Vol % 0.3. Also, the air fraction increases with a constant sand fraction in Sand 1 FIR 50 Vol %, FIR 70 Vol % 0.5 and FIR 80 Vol % residual as shown in Table 4-2. The foam infiltration is not so clear in FIR 50 Vol %, while it results in permeability reduction in k_{3-4} in FIR 70 Vol % 0.5 and an infiltration depth larger than 1cm in FIR 80 Vol % residual as k_{4-5} is influenced by foam infiltration (see Figure 4-20 and Figure 4-21). These results indicate that an increased air fraction at a fixed sand fraction in the mixture will promote the foam flow, which is contrary to what is found by Xu et al. (2020).

4.5 Discussion

Figure 4-20 to Figure 4-24 show that the foam infiltrated sand has a lower permeability than the consolidated mixture on top of the sand. This is likely caused by the different sand matrix between a foam infiltration layer and a consolidated mixture layer. In a foam infiltration layer, the sand particles are more compacted than those in a consolidated mixture. With a more compacted sand matrix, the foam bubbles are more deformed so that the seepage path for water becomes more tortuous. The consolidated mixture close to the sand surface has a smaller permeability compared with that from a consolidated layer far away from the sand surface, as can be seen that $k_{1,2}$ is larger than $k_{2,3}$ in most cases. A possible scenario is the consolidated mixture close to the sand surface is subjected to considerable foam loss which results in a relatively compacted sand matrix in the layer. While the bubble loss in far away from the sand surface is only limited, and the sand matrix is therefore in a loose state.

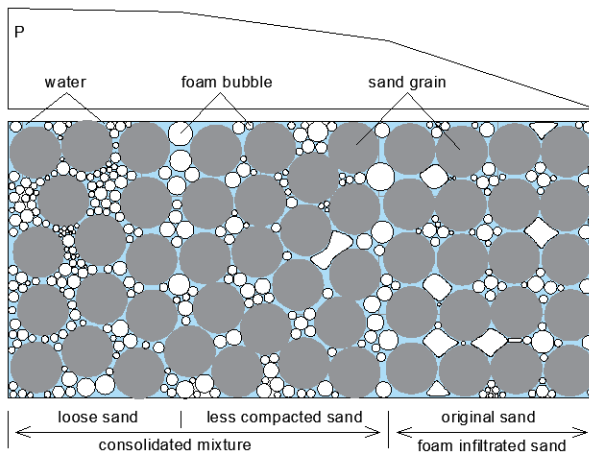


Figure 4-25. Sketch of mechanisms during sandy foam infiltration

Figure 4-25 shows a conceptual sketch of the mechanisms. The bubbles take up the pore space among the sand grains that are densely compacted in the original sand. While the sand grains in the mixture near the sand surface are less compacted during consolidation due to the water and bubble loss. In the mixture far away from the sand surface, the sand grains are in a loose state because the bubble loss is limited due to the blockage effect of the consolidated mixture close to the surface and also the foam

infiltrated sand. The bubbles in the loose sand are more or less connected which results in a smaller pressure drop, and therefore a higher permeability compared with the consolidated mixture close to the sand surface.

The difference in permeability induced by the sand matrix indicates that the permeability of a foam-sand mixture may be well determined by the sand parameters and the foam itself. Because the results from Figure 3-9 suggest that there is a decreasing trend when increasing the FER. It seems there is a critical FIR above which the permeability of the foam-sand mixture after consolidation will not be significantly lowered anymore. Because the maximum pore space in the consolidated mixture is limited (which is the pore volume at maximum porosity).

Looking again at Figure 4-20, k_{1-2} is comparable to k_{2-3} after consolidation in case of FIR 30 Vol % and 40 Vol %, which can be explained that the consolidated mixture is the same at any location without foam infiltration in the saturated sand. It also shows that the permeability of the consolidated mixture is around 5×10^{-5} m/s, comparable to the recommended FIR of 30 Vol % - 40 Vol % by EFNARC (2005). While at $\text{FIR} \geq 50$ Vol %, k_{1-2} is smaller than k_{2-3} after consolidation, indicating that the consolidated mixture close to the sand surface has a lower permeability, which could be induced by the loss of foam bubbles into the saturated sand. The consequence is a denser sand matrix together with the entrapped bubbles which results in a lower permeability than that far away from the sand surface.

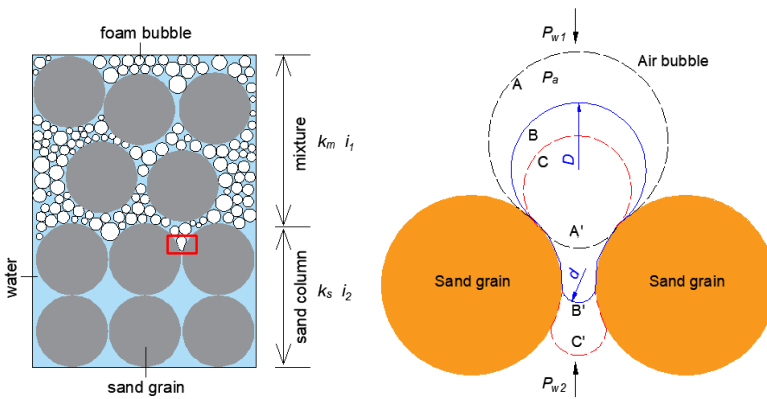


Figure 4-26. Sketch of (a) bubble penetration from sandy foam into saturated sand and (b, from Figure 3-4) bubble deformation during penetration

Figure 4-26a shows a sketch of foam penetration from mixture to saturated sand. The following relation can be obtained according to Darcy's Law:

$$\frac{i_1}{i_2} = \frac{k_s}{k_m} \quad (4-3)$$

With k_m and k_s the permeability of the mixture and the saturated sand, respectively and i_1 and i_2 the hydraulic gradient in the mixture and the saturated sand, respectively.

Figure 4-26b shows the change in shape for a single bubble to penetrate the pore throat. The minimum hydraulic gradient (i_{min}) required for bubble penetration is 36, 23 and 29 for Sand 1, Sand 2 and Sand 3, respectively (from Chapter 3). In both the experiments and the field condition with a shield diameter of 10 m and an extra pore water pressure of 50 kPa, the hydraulic gradient is $i = 1$ (Zheng et al., 2021), indicating that no bubble could penetrate the soils if the mixture has a permeability similar to the soils.

Equation (4-3) suggests foam penetration could only take place when $k_s / k_m > 36$ for Sand 1. The permeability of the foam-sand mixture (k_f) should be smaller than 4×10^{-6} m/s for Sand 1 and 2×10^{-5} m/s for Sand 2 and Sand 3 in this case. It should be noted that the EFNARC (2005) recommended value for the permeability of a foam-sand mixture should be smaller than $10^{-5} \sim 10^{-6}$ m/s, which covers the theoretical values for the mixtures in this study.

The implication from Equation (4-3) can explain the start of foam spurt in a pure foam infiltration. As shown in Chapter 2, bubble penetration will be initiated from the start of the test. Independent foam drainage test shows the permeability of pure foam ranges from 3×10^{-8} m/s to 3×10^{-6} m/s, which is smaller than the maximum permeability required for bubble penetration as shown above. Bubble penetration is therefore an initial process from the beginning of the pure foam infiltration test.

4.6 Chapter summary

Foam infiltration tests were conducted to investigate the infiltration behavior of sandy foam to saturated sand using a column test. Influences from FIR, remaining water content and sand type were examined. Based on the experimental results, several

conclusions can be obtained.

1) Increasing the FIR and reducing the remaining water content result in a foam infiltration layer with a higher flow resistance, which reduces water leakage from the foam-sand mixture to the soils. This sealing effect is realized through the low permeable layer that is formed during foam bubble infiltration. Although the consolidation of the foam-sand mixture also results in a decrease in its permeability, the permeability of the foam infiltrated sand is the lowest in the whole system.

2) The sand matrix plays an important role in determining the permeability of a foam-sand-water mixture. This was ensured by the comparison on the permeabilities among the foam infiltrated sand, consolidated mixture close to the sand surface and that far away from the sand surface. The permeability is smallest in a foam infiltrated sand and largest in the consolidated mixture away from the sand surface. Further experiments on pure foam infiltration with the same sand column while different densities (different sand matrix) can provide additional information to this conclusion.

3) There is no foam infiltration in Sand 1 when the FIR is smaller than 40 Vol %. Hardly any foam penetrating the sand can be expected at such condition. The foam bubbles will remain in the sand-foam mixture. In this situation, the pressure in the excavation chamber can be predicted with the model presented by Bezuijen & Dias (2017).

4) Increasing the FIR just before standstill could be more applicable regarding the pressure maintenance during ring building. Results show that a higher FIR could increase foam infiltration, which will lead to a foam infiltration zone with a lower permeability than that in a consolidated mixture. Less water leakage can be expected in this case and thus less pressure dissipation within a certain time period, which could be beneficial to the tunnel face stability as well as reducing the frequency of foam injection during ring building. However, this should be validated through model or field test.

5) Bubble penetration is influenced by the ratio between the permeability of the foam-soil mixture and the soils at the tunnel face. There is a maximum permeability for a mixture above which no bubble penetration can be expected based on the micro

stability model presented in Chapter 3. Because there will be insufficient pressure gradient to press the foam bubbles out of the foam-sand mixture if the permeability of the mixture is too high. A lower permeability of the mixture results in an increased bubble penetration which is in line with the experimental results. It corresponds to the increased foam penetration when increasing the FIR, which actually means a decrease in the permeability of the foam-sand mixture by increasing the FIR. Further experiments on sandy foam infiltration with sand columns at different hydraulic gradients could provide more information to this conclusion.

Chapter 5 Surface tension of foam and its influence on tunneling

Foam is produced in a predetermined concentration of foaming agent and water and injected to the excavation chamber for soil conditioning in EPB shield tunneling. This mixing process will induce the dilution of the foaming liquid and thus influence its surface tension. This chapter presents an experimental study on the influence of dilution of foaming liquid as could be expected in EPB shield tunneling. The capillary rise method is employed for the measurement of surface tension at different concentrations. It is shown that in a typical tunnel application the surface tension can be twice as high as that in the original foam. Consequences from the increase in surface tension are theoretically analyzed. Volume change and compressibility of the foam bubbles are hardly influenced by the increased surface tension for the foam used in tunneling. It is shown that the influence of a higher surface tension is negative for the formation of a low permeable layer which is anticipated by engineers. The sandy foam infiltration experiments suggest the increase in surface tension due to dilution will lower the foam penetration potential. The study suggests that the change in surface tension due to dilution in tunneling should be incorporated in the inspection of foam-soil interactions.

5.1 Introduction

Foam as an additive for soil conditioning has been widely used in EPB shield tunneling. While only limited research could be found regarding its properties (Wu et al., 2018, Thewes et al., 2012). Conventional tests put more emphasis on the integral properties of such a foam-soil-mixture including its rheology (Peila et al., 2009; Quebaud et al, 1998), shear behavior (Pena, 2007; Psomas, 2001), compressibility (Bezuijen, 2013; Pena, 2007) and permeability (Borio & Peila, 2010; Bezuijen & Schaminée, 1999). These properties are critical in engineering applications and have greatly contributed to the application range of the EPB shield TBM.

Some recent research (Wu et al., 2020; Xu, 2018; Galli, 2016; Psomas, 2001; Bezuijen & Schaminée, 1999; Quebaud et al, 1998) focus on the interaction between foam and

soil that is anticipated in the excavation chamber. However, the macro behavior (such as the infiltration behavior of foam bubbles) of such a mixture sometimes is difficult to be explained due to the lack of knowledge on the foam-soil interaction at micro scale level (Wu et al, 2020; Xu, 2018; Bezuijen, 2013). One of the important parameters related to the foam bubbles is the surface tension, while it is seldom investigated in previous studies.

The role of surfactant is to lower the surface tension of the target liquid, making it possible to produce foam. The pressure difference between the inside and outside of a bubble in liquid is:

$$P_a - P_w = \frac{2\gamma}{R} \quad (5-1)$$

With P_a the pressure inside the bubble, P_w the liquid pressure outside the bubble, γ the surface tension and R the radius of the bubble.

The principle of a foam generator is to mix an air flow and a liquid flow through a porous medium such as a bed of glass beads (Psomas, 2001). With a given air pressure, the size of the generated bubbles will be smaller at a lower γ according to Equation (5-1).

Foam is usually pre-generated at a certain concentration of foaming agent and water and injected into the excavated soils. It is mixed in the excavation chamber together with the excavated soils. Under the groundwater table, the remaining pore water in the excavated soils will induce the dilution of the foaming liquid surrounding the foam bubbles, resulting in a potential change in its surface tension.

To this end, surface tension of foaming liquid at different concentrations is measured with the capillary rise method. A theoretical study is implemented to convey the influence from the increment of surface tension on the micro behavior of the foam such as volume change, compressibility and mobility. A series of sandy foam infiltration test is conducted to study the influence of surface tension on bubble penetration. Consequences for tunneling are discussed.

5.2 Materials and procedure

5.2.1 Foaming liquid and capillary tube

Foaming agent Condat CLB F5/TM is used for this study. The foaming liquid is created by adding foaming agent to water with a predetermined ratio to get different concentrations and mixed manually. The concentration ($C. \%$) of the foaming liquid is calculated:

$$C. \% = \frac{V_s}{V_w + V_s} \quad (5-2)$$

With V_s the volume quantity of the foaming agent and V_w the quantity of water.

A commercial glass capillary tube (CM Scientific, CV1525 Borosilicate Glass Round Capillaries) is used for the measurements. The capillary tube has an inner diameter of 0.15 mm and an outer diameter of 0.25 mm and a length of 300 mm.

5.2.2 Procedure

The capillary tube with a black background is placed on a ruler that is supported with a stick hold vertically by a stand. Because the inner diameter of the capillary tube is only 0.15 mm, a camera with magnification is used for the recognition on the capillary rise in the tube. The container has a diameter of 10 cm and a depth of 3 cm. The capillary end is put 1 cm into the liquid. The measurement is also conducted with water as a reference. All measurements are carried out at a room temperature of 20 °C and each measurement takes 24 hours to get a stable capillary rise. In case there is liquid loss due to vaporization, new liquid is slowly injected with a syringe to achieve a comparable initial liquid level. The whole measuring system is shown in Figure 5-1.



Figure 5-1. Picture of the testing system

5.3 Results and discussion

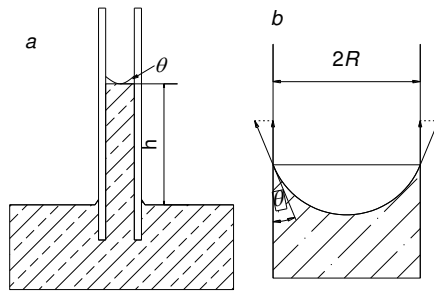


Figure 5-2. Capillary rise in a tube with a small diameter.

Inserting a capillary tube vertically into a liquid will result in a capillary rise due to the surface tension of the liquid (Figure 5-2a). By balancing the pressures between the capillary liquid (under the meniscus) and the atmosphere (Figure 5-2b), the following relation can be obtained:

$$\frac{2\gamma \cos \theta}{R} = (\rho_w - \rho_a)gh \quad (5-3)$$

The surface tension (γ) can be calculated with the measured capillary rise in the tube.

$$\gamma = \frac{(\rho_w - \rho_a)hgR}{2 \cos \theta} \quad (5-4)$$

With ρ_w the density of water, ρ_a the density of air, h the capillary rise in the tube, g the acceleration of gravity, R the radius of the tube and θ the contact angle between the

wall and the liquid, which is usually 0.

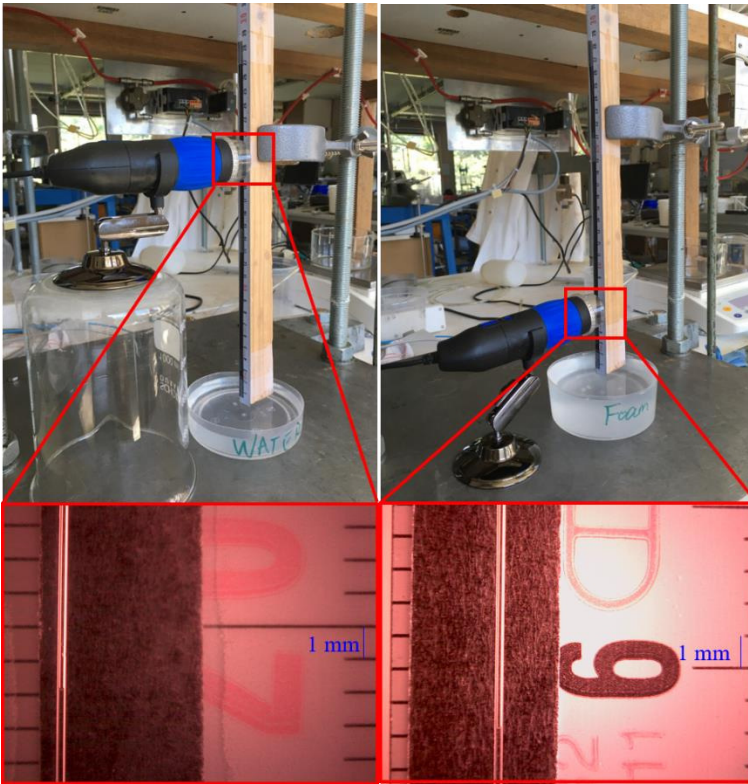


Figure 5-3. Capillary rise at the end of each test (left: water; right: foaming liquid 3%)

Figure 5-3 shows that the measured capillary rise at the end of the test for water and foaming liquid is 19.82 cm and 5.83 cm, respectively. With Equation (5-4), the measured surface tension of water is 0.0728 N/m, very close to the standard value of 0.07275 N/m (Vargaftik et al., 1983), indicating the accuracy of the capillary rise method.

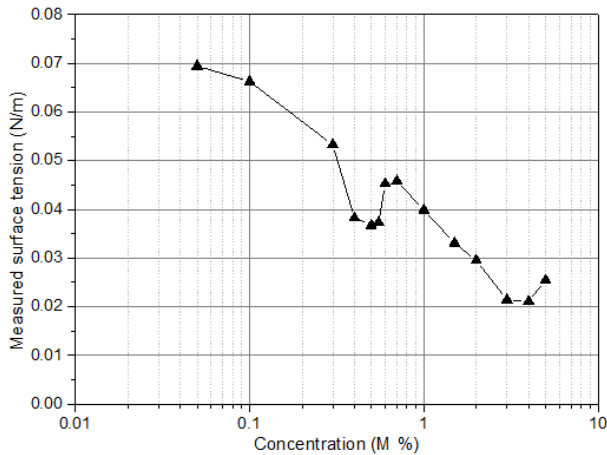


Figure 5-4. Measured surface tension at different concentrations.

Figure 5-4 shows the measured surface tension as a function of concentration for the foaming liquid. It shows that with a concentration of 3 M % foaming liquid, the surface tension can be lowered effectively to around 0.0214 N/m, smaller than one third of the surface tension for water. Barely any reduction on it can be achieved by further increasing the concentration. On the contrary, increasing the concentration to 5 M % results in an increase in its surface tension. This may explain the reason why 3 M % is preferred in field use because it is cost effective and it has a small surface tension.

It should be noted that below 3 M %, the surface tension increases with decreasing concentration as is expected. However, results show that this is not a monotonic relation. Instead, there is a U curve in the range between the concentration of 0.3-0.7 %. Inside this range, the surface tension first decreases with decreasing concentration until 0.5 M %, after which it increases again. After this U curve, the increase will continue as the concentration decreases. At the concentration of 0.05 M %, the surface tension is almost 0.07 N/m, close to the value of water.

Normally the results shown in Figure 5-4 match the initial purpose in the engineering application. Because the foam bubbles produced at the concentration of 3 M % have a low surface tension. However, as mentioned in the beginning, mixing the foam with the excavated soils results in the dilution of the foaming liquid, which will induce the increase in its surface tension.

The increase in surface tension will depend on the ratio between the FIR and the porosity (n_s) of the excavated soils. In this way, the concentration of the foaming liquid in the foam-soil-mixture ($C. '%$) can be calculated as follows:

$$C.'\% = \frac{FIR}{FERn_s(1 - \frac{\lambda}{n_s}) + FIR} C.\% \quad (5-5)$$

It should be noted that the groundwater flow is not considered in Equation (5-5). Because with continuous drilling the concentration of the foam in the mixture will be closer to the original foam. This dynamic condition will complicate the current study that here it is only discussed without the influence of the groundwater flow.

The surface tension of the liquid in this foam-soil-mixture should then be determined with the new concentration calculated with Equation (5-5). Assuming the FIR is 40 Vol % and the porosity of the soils is 0.4. For fine sand there is no foam infiltration at the tunnel face and all pore water is taken into the excavation chamber, which is a reasonable assumption as is found by Bezuijen and Dias (2017). The resulting concentration of the foaming liquid in the excavation chamber according to Equation (5-5) is 0.27 M %. The surface tension of the liquid is then 0.054 N/m, twice the value of the initial foam.

A bubble usually becomes smaller when its surface tension increases. As illustrated in Figure 5-5, when its surface tension increases from γ to γ' , the radius of the bubble decreases from S to s . And the pressure inside the bubble changes from P_a to P_a' .

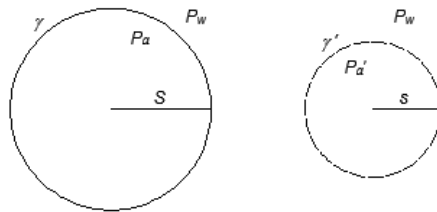


Figure 5-5. Definition sketch of a foam bubble being compressed when its surface tension increases.

By the definition of surface tension (γ), the following relations can be obtained:

$$P_a - P_w = \frac{2\gamma}{S} \tag{5-6}$$

$$P_a' - P_w = \frac{2\gamma'}{s} \tag{5-7}$$

With P_w the pore water pressure.

Combining these two yields:

$$P_a' - P_a = \frac{2\gamma}{s} - \frac{2\gamma'}{S} \tag{5-8}$$

Also, according to Boyle’s Law

$$\frac{P_a' - P_a}{P + P_a} = \left(\frac{S}{s}\right)^3 - 1 \tag{5-9}$$

With P the atmospheric pressure (1 bar).

With Equations (5-8) and (5-9), the volume change of the bubble can be obtained when its surface tension increases.

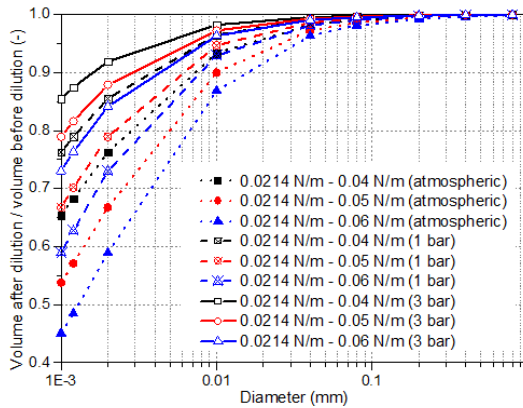


Figure 5-6. Normalized volume ratio between bubble volumes after and before surface tension increases. The different lines represent different γ' for the foam after dilution. Value of γ for the initial foam is 0.0214 N/m.

Figure 5-6 shows that when surface tension increases, the volume of a foam bubble will decrease. With a smaller diameter, the change in volume will be more significant because the surface tension will be dominant. The volume also decreases more with

more increment in surface tension. With a higher pore pressure, the influence on volume change due to the increasing surface tension will be smaller. It shows that for bubbles bigger than 0.02 mm, the volume ratio is still larger than 0.95 when the surface tension increases to 0.6 N/m at a pore pressure of 3 bar, which is a possible scenario in tunneling application.

The diameter of the foam bubbles used in EPB shield tunneling is usually larger than 0.02 mm, as is shown in Chapter 2 and by from Wu et al. (2018) and Wang et al. (2020). When the diameter of the foam bubble is larger than 0.02 mm, the volume ratio after the decrease is still larger than 0.95, indicating that the volume change can be negligible when the foam is mixed with the excavated soils.

Sand grains and liquid are usually treated as incompressible media compared with gaseous phase in a foam-soil-mixture. Assume a foam bubble with an initial radius S , the surrounding pore pressure is P_w and the air pressure inside the bubble is P_a . After applying an excess pore pressure of ΔP_w , the bubble will be compressed and the radius will become s . The situation is illustrated in Figure 5-7.

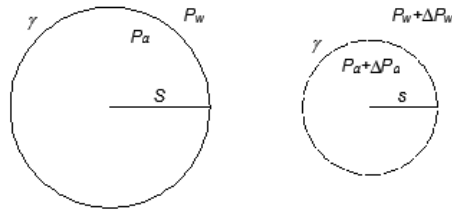


Figure 5-7. Sketch of a foam bubble being compressed when applying an excess pore pressure.

By the definition of surface tension (γ), the following relations can be obtained:

$$P_a - P_w = \frac{2\gamma}{S} \quad (5-10)$$

$$(P_a + \Delta P_a) - (P_w + \Delta P_w) = \frac{2\gamma}{s} \quad (5-11)$$

With ΔP_a the increase in air pressure inside the bubble.

Combining these two equations yields:

$$\Delta P_a - \Delta P_w = 2\gamma\left(\frac{1}{s} - \frac{1}{S}\right) \tag{5-12}$$

Resulting in, according to Boyle’s law

$$\frac{\Delta P_a}{P + P_a} = \left(\frac{S}{s}\right)^3 - 1 \tag{5-13}$$

Equations (5-12) and (5-13) enable the calculation of the volume ratio between the original volume and after being compressed at an excess pressure of 50 kPa (the ratio is 1.5 for ideal gas).

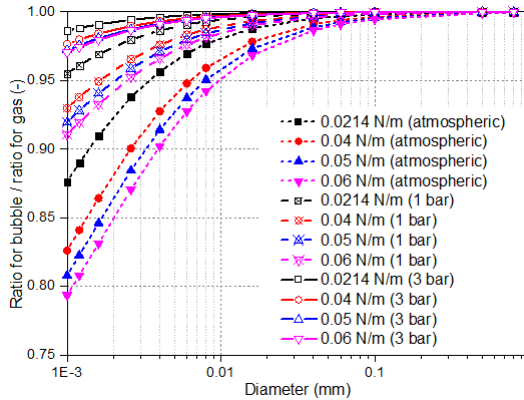


Figure 5-8. Normalized volume ratio between original foam and after being compressed at different surface tensions under various pore pressures. Different lines represent different γ' for the foam after dilution.

Figure 5-8 shows the normalized volume ratio between original foam and after being compressed at different surface tensions under various pore pressures. The situation simulates the volume ratio between the original volume and after being compressed at an excess pressure of 50 kPa (the ratio is 1.5 for ideal gas at atmospheric pressure and 1.25 and 1.125 at 1 bar and 3 bar of pore water pressure, respectively). Results suggest the influence on compressibility is not so obvious in tunneling at a high pore pressure (3 bar) as the compressibility is almost the same to ideal gas even at a larger surface tension (0.6 N/m). While for a smaller pore pressure (for example, atmospheric pressure), the compressibility can be influenced by surface tension, which should be taken into account when conducting experiments at atmospheric pressure.

The above discussions indicate that the influence from the increase in surface tension on volume change and compressibility can be negligible for foams used in tunneling practice. However, the influence from the increase in surface tension can be significant with respect to the mobility of foam bubbles. In the micro stability model presented in Chapter 3, the minimum pressure drop required to for an individual bubble to penetrate is:

$$P_{w1} - P_{w2} = 4\gamma\left(\frac{1}{d} - \frac{1}{D}\right) \quad (5-14)$$

Equation (5-14) shows that the required pressure drop to initiate the penetration process is proportional to the surface tension of the bubbles. The increase in surface tension makes it more difficult for a foam bubble to squeeze through the pore throat. The consequence is the lowered potential of a low permeable layer at the tunnel face which is preferred in tunneling.

To investigate the influence from dilution on the foam infiltration behavior, experiments were conducted to examine the foam infiltration behavior at different surface tension. Sand 3 and foam of FER 10 were used in this series of tests as the grain / bubble size distribution curves are shown in Figure 5-9.

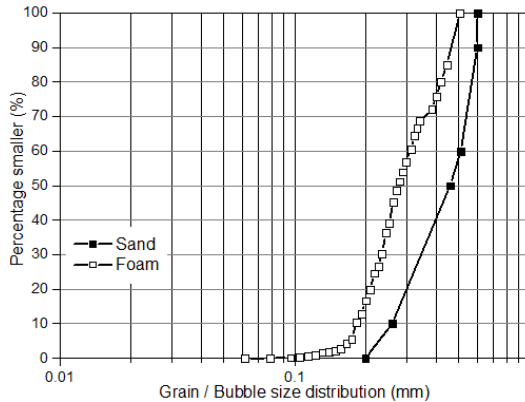


Figure 5-9. Grain / Bubble size distribution curve of sand / foam

The difference in surface tension was achieved by replacing the water used in making the foam-sand mixture with the original foaming liquid (at 3 M %). Table 5-1 shows that when the foam is mixed with water and sand, the resulting mixture has a larger surface tension which is more than two times higher than original foam. Pore water

replacement represents the ratio of pore water in a unit soil volume being replaced by foam infiltration as shown in Chapter 4. In order to get the same mixture with the same fractions of air, liquid and sand, part of water was replaced by foaming liquid when making the mixture. This results in the same mixture with different surface tension as shown in Table 5-1.

Table 5-1. Amount of foam and liquid used for the foam-sand mixture and the resulting surface tension

PWR (-)	Test no.	Weight (g)			Concentration (M %)	γ (N/m)
		Foam	Water	Foaming liquid		
0.3	1-1*		428	0	0.54	0.037
	1-2	94	167	261	1.5	0.033
	1-3		0	428	3.0	0.021
0.5	1-4*		325	0	0.7	0.046
	1-5	99	113	212	1.5	0.033
	1-6		0	325	3.0	0.021
0.7	1-7*		211	0	1.0	0.04
	1-8	105	53	158	1.5	0.033

* Results from Chapter 4.

The experimental set-up shown in Figure 5-10 is similar to that used in Chapter 4 where the principle of the equipment can be found. k1 in the top of the cylinder measures the applied air pressure, k2 and k3 measure the pore water pressure in the mixture, and k4, k5 and k6 measure the pore water pressure in the saturated sand. An additional pressure transducer k7 was used in the test no. 1-1, 1-4, 1-5, 1-6 and 1-7.

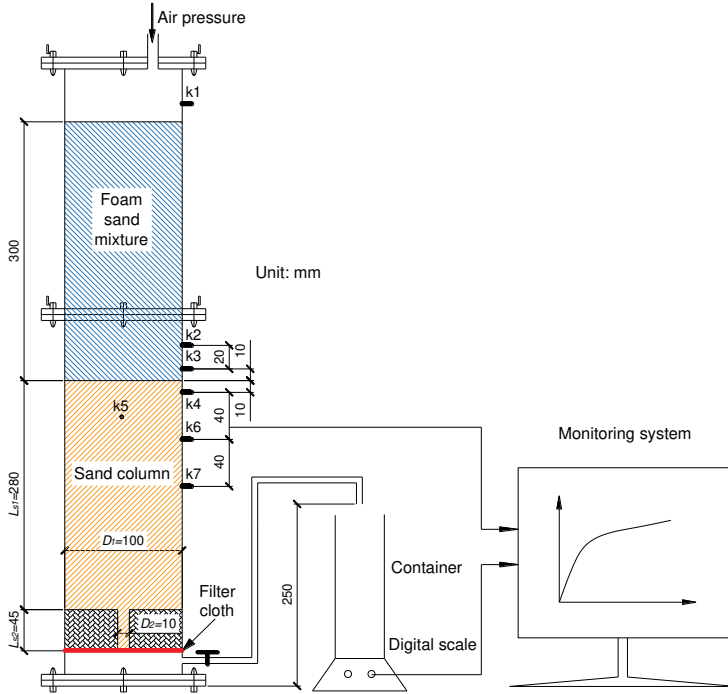


Figure 5-10. Schematic view of the experimental set-up.

The preparation of the sand sample was the same to that in Chapter 2. The foam is first produced at atmospheric pressure and then pressurized during the test at an absolute pressure of 1.5 bar. According to Boyle's Law the following relation can be obtained:

$$FER_p = \frac{P}{P_a} (FER_a - 1) + 1 \quad (5-15)$$

where FER_p is the FER at the desired air pressure, FER_a the FER at atmospheric pressure and p the desired air pressure (total pressure: atmospheric plus excess pressure). According to Equation (5-15), to get an FER 10 at 1.5 bar, the FER should be 14.5 at atmospheric pressure.

The foam-sand mixture is mixed manually until it reached a homogenous state and placed on top of the sand column. An air pressure of 50 kPa is then applied and the experiment starts after the valve is open and the discharged water and pore pressures are recorded every second. Because the focus was to examine the foam infiltration

behavior which is most noticeable during foam spurt as shown in Chapter 2, the test duration was 1 hour in this test series.

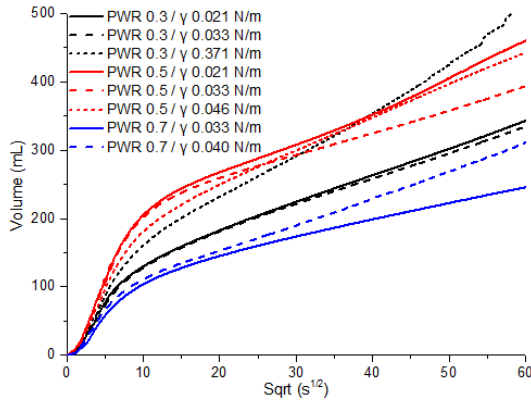
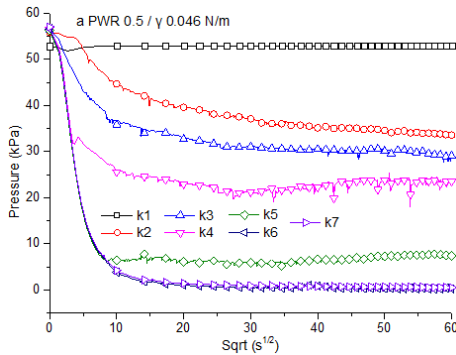


Figure 5-11. Measured water discharge against square root of time

Figure 5-11 shows the measured water discharge in each test. In general, there is a linear relation between the volume and square root of time in each test after the initial fast discharge. As discussed in Chapter 4, the consolidation of the mixture is the dominating process which results in this linear relation. It could also be observed from the figure that the slope of this linear line is different with different surface tension in the mixture. Figure 5-11 shows that there is an increasing potential in the slope of the linear section with an increase in surface tension, which could be induced by the difference in bubble penetration.



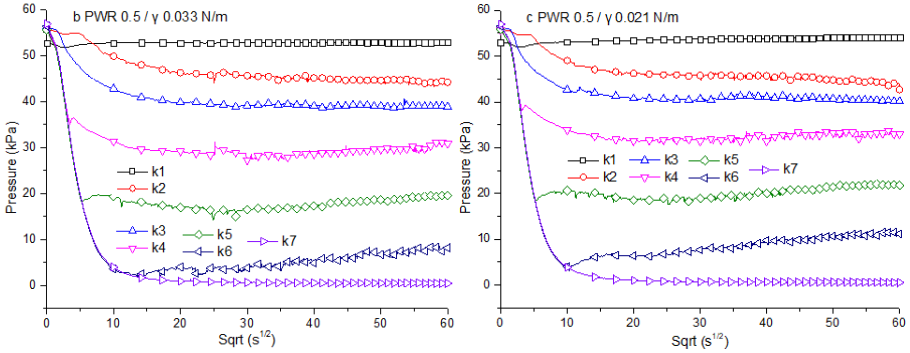


Figure 5-12. Pore water pressure distribution curve in different tests.

Figure 5-12 shows the measured pore pressures in the tests with pore water replacement at 0.5. It shows that the bubble penetration is faster and longer when the surface tension is smaller. As the foam front reached k5 (3 cm below the sand surface) in Figure 5-12a later than in Figure 5-12b and Figure 5-12c. The foam front reached k6 (5 cm below the sand surface) at a decreased time point as the surface tension decreases as shown in Figure 5-12. Indicating an increase in surface tension could induce a decreased potential of bubble penetration.

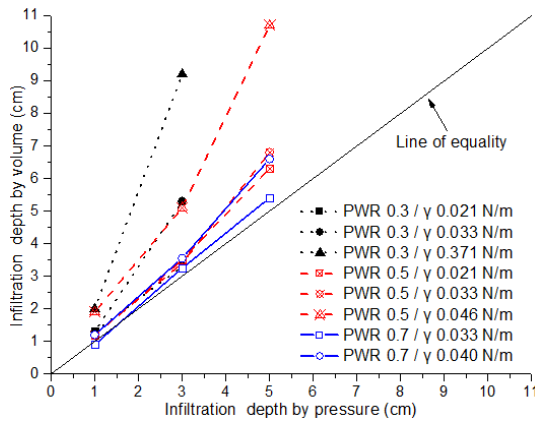


Figure 5-13. Comparison between infiltration depth determined by measured pressure and volume.

Figure 5-13 shows the comparison between the infiltration depth by the measured pore pressures and by the discharged water when the foam front reaches the corresponding pressure transducers. In general, the bubble penetration depth is in most cases smaller

than that calculated with the discharged water. The only exception is in the test with 0.7 Water + Foaming liquid where the bubble penetration depth at 1 cm is larger than calculated with discharge water. Figure 5-13 also shows that an increase in surface tension results in a larger deviation between the two depths. The results suggest the increase in surface tension lowers the potential of bubble penetration, which is in support of the speculation that dilution of the foam will weaken its penetration ability and will lead to a higher permeability at the front face. The consequence should be considered when evaluating the foam infiltration behaviors.

Early results from Bezuijen and Schaminée (1999) show that a foam-sand mixture could stay much more stable than pure foam. This was further proved by Wu et al. (2020) who have shown that the soils play an important role in stabilizing the foam when it is mixed with soils. In their study, bubble evolution was observed with elapsed time and results indicated that the bubble coalescence was hampered in the presence of soil particles. Moreover, the soil particles could prevent the upward movement of the bubbles due to gravity and thus contribute to the stability of foam. However, the research by Wu et al. (2020) only considered one water content (indicating only one value of surface tension of the resulting foam) in their experiments. With different water contents, the results may vary accordingly. This makes it an interesting topic for further research.

It should be noted that the foam bubble size found in literature was measured at atmospheric pressure. While the foam is produced at applied air pressure up to several bars in tunneling practice. The results from Wu et al. (2020) suggest that the bubble size for foam that are compressed at a certain pressure is almost identical to the one for foam that are generated at that pressure. For bubbles with a diameter of 0.02 mm at atmospheric pressure, applying a pressure of 3 bar (30 m below water table) will induce a reduction on the bubble diameter from 0.02 mm to 0.016 mm according to Boyle's law. With Figure 5-6, it can be seen that the volume change due to the increase of surface tension can still be negligible at this size range.

5.4 Chapter summary

An experimental study on surface tension of foaming liquid at different concentrations

was conducted with the capillary rise method. Injecting foam into the excavated soils induces the dilution of the foaming liquid surrounding the foam bubbles and consequently results in an increase in surface tension. Up till now, works on foam research failed to incorporate this influence. This work suggests that the surface tension after the foam being mixed with the excavated soils can be twice the value before mixing. Volume change and compressibility for the foam used in tunneling can be negligible within the range of increment in surface tension. While the ability for foam to penetrate the grain skeleton is lowered as a result. The conceptual model described was supported by a series of sandy-foam infiltration tests, where the same foam-sand mixtures with different surface tension were created by replacing different amount of water content with the foaming liquid. Results suggest that the increase in surface tension due to dilution will lower the penetration potential. The influence on the stability of the foam-sand mixture should be further investigated.

Chapter 6 A New Model for Predicting the Marsh Funnel Test

This chapter is adapted from the technical note: Zheng, D., Bezuijen, A., & Di Emidio, G., 2021. A new model for predicting the Marsh funnel test. Int. J. Geomech., 21(2): 06020042. [https://doi.org/10.1061/\(asce\)gm.1943-5622.0001913](https://doi.org/10.1061/(asce)gm.1943-5622.0001913)

This chapter presents a new model for predicting the fluid flow through a Marsh funnel (MF). Based on Herschel-Bulkley fluid model, the model considers both the friction force and the dynamic force. Pressure drop due to the yield stress in the conical section is accounted in the model. In addition, an improved testing system is proposed for the validation of this new model. Experiments were conducted with several Newtonian fluids as well as some non-Newtonian fluids. Experimental and model results on dynamic forces show good agreement. Although the model slightly under-predicts the Marsh funnel time, the overall match is good. The general agreement suggests that the new model can be used for a fast estimation of the rheology parameters of a liquid using Marsh funnel test results and can be used in field applications.

6.1 Introduction

The MF test has been used in a wide range of applications including oil industries (Balhoff et al., 2011; Sedaghat et al., 2017), grouting application (Le Roy & Roussel, 2005; Sadrizadeh et al., 2017), drilling industries (Pitt, 1999; Guria et al., 2013) and tunneling (Peila et al., 2011; Schoesser & Thewes, 2015). Developed in the late 1920s, the Marsh funnel test is a robust and simple testing method in quality control over the target fluid. Traditionally, a Marsh funnel test results in just one value, the MF time. This makes the measurement easy but does not allow testing viscous and plastic properties separately. Different approaches (Pitt, 1999; Le Roy & Roussel, 2005; Balhoff et al., 2011; Guria et al., 2013; Sedaghat et al., 2017; Sadrizadeh et al., 2017) have been proposed to measure the rheological properties of the fluids using the Marsh funnel test.

The Marsh funnel testing method has been applied in mechanized tunneling for quality

control of the bentonite suspensions (Schoesser and Thewes, 2015). The resulted MF time reflects the fluidity of the bentonite suspensions utilized in field applications. The optimal value of the MF time for these bentonite suspensions is in the range of 30-45 seconds (Peila et al., 2011). Recent studies (Xu & Bezuijen, 2019) have illustrated the importance of the rheological properties such as yield stress and viscosity on influencing the infiltration characteristics of bentonite slurries into sand. These infiltration characteristics have consequences for the excess pore water pressure in front of a tunnel face during drilling with a slurry shield tunnel boring machine (TBM). Since the MF test is a simple and inexpensive testing method frequently used in field applications for quality control, it is therefore of great interest to explore the possible potential of using the Marsh funnel to obtain more information on the tested fluids.

Pitt (1999) investigated the flow behavior of the Marsh funnel test using a numerical solution based on the power law fluids and derived a simplified equation for field use. Le Roy and Roussel (2005) studied the possibility of using the Marsh funnel test for measuring the viscosity of Newtonian fluids and extended the measurement on cement pastes. The predicted and measured flow time was compared and the correlation between flow time and cement pastes viscosity stayed valid only for no yield stress cement pastes and for flow time higher than 15 s in the chosen funnel. Balhoff et al. (2011) developed a new model describing non-Newtonian fluid flow through a Marsh funnel. By fitting the measured height against time data in a Marsh funnel test to the model, rheological parameters can be obtained numerically. Moreover, the yield stress can be measured under the condition that there is a stagnation point in the funnel after the test. Guria et al. (2013) established a model in which the wall shear stress is evenly distributed over the wall in the funnel and converted the measured drainage volume against time data into the consistency plot of the fluid. The methodology was adopted by Schoesser and Thewes (2015) in which they compared the consistency plots obtained by the model and by the standard viscometer. Large deviations, however, were found when comparing the results. Sadrizadeh et al. (2017) investigated both the analytical and the numerical approaches to a Marsh funnel test with Newtonian fluids. A discharge coefficient in the analytical model is introduced and determined by

comparing the numerical and analytical evaluations. Sedaghat et al. (2017) also developed a new model concerning the Marsh funnel test. A flow factor similar to the discharge coefficient mentioned in the model by Sadrizadeh et al. (2017) is presented in the model and determined experimentally. It seems that the discharge coefficient (Sadrizadeh et al., 2017) and the flow factor (Sedaghat et al., 2017) are somewhat related to the dynamic force that is addressed by Pitt (1999) as kinetic energy.

In this chapter, a new model is established based on the Herschel-Bulkley fluid model. The new model considers the pressure loss due to the acceleration of the fluid in the funnel and due to the yield stress in the conical section. The new model is based on physical analysis. A numerical solution is implemented to obtain the simulation results. An improved testing system is established, and comparative tests are conducted to measure the dynamic forces. Experiments are conducted with several Newtonian fluids as well as some non-Newtonian fluids. Measured dynamic forces and MF times are compared to the model results. Further application, making use of the measured MF test data for predictions of rheological parameters, is discussed.

6.2 Marsh funnel geometry

Geometry of a Marsh funnel may vary according to different testing standards. Figure 6-1 shows the standard dimensions of an American Petroleum Institute (API, 2009) recommended Marsh funnel. In this test, the funnel is filled with 1500 ml of fluid and the time it takes for one quart (946 ml) of that fluid to drain is recorded as the MF time (API, 2009).

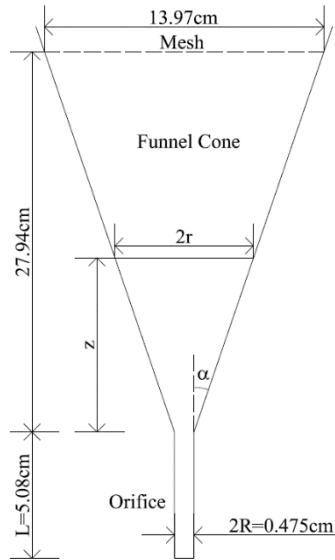


Figure 6-1. Marsh funnel dimensions according to API (2009)

6.3 Theoretical development

6.3.1 Rheology model

According to API (2009), the rheological behavior of bentonite slurries can be described by the Herschel-Bulkley model. This model consists of three parameters: yield shear stress (τ_0), consistency index (C) and flow index (n). The model can describe a lot of fluid models (Newtonian, Power law, Bingham etc. See Figure 6-2). It reduces to the Bingham model in the case of the flow index (n) becoming 1, which can be expressed as:

$$\tau = \tau_0 + C\gamma^n \quad (6-1)$$

With τ the shear stress, τ_0 the yield stress and γ the shear rate.

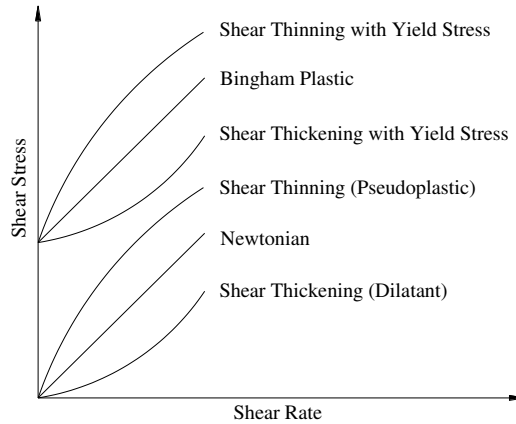


Figure 6-2. Possible behavior of a Herschel-Bulkley model depending on parameters (Data from Schoesser & Thewes, 2015)

6.3.2 Model assumptions:

Some simplifications are necessary to be able to describe the flow through the Marsh funnel. The simulation model presented in this chapter is based on the following assumptions:

- 1) The fluids being tested are incompressible.
- 2) A static condition for the flow in the upper cone section is assumed. The shear rate in the upper cone section will be much less than in the capillary tube and only the yield stress will be dominant in the cone. The friction force on the sidewall is equal to the yield stress (τ_0) under this assumption.
- 3) Entrance effects at the connection between the conical section and the capillary tube are neglected.
- 4) The flow in the entire capillary tube is fully developed Poiseuille flow. The fluid in the Marsh funnel will accelerate due to the dynamic pressure. The velocity of the fluid along the capillary tube is the same as required by continuity.

6.3.3 Model derivation

The fluid in the upper conical section is static as assumed, and it is accelerated due to

energy transformation when it enters the capillary tube. Following Bernoulli's equation, the relation between dynamic pressure (p_d) and mean velocity (v) can be written as:

$$p_d = 0.5\rho v^2 \quad (6-2)$$

With ρ the density of the fluid and v the mean velocity.

According to Skelland (1967), the relation between the wall shear stress (τ_w) and the discharge rate (Q) in a Hershel-Bulkley fluid flowing through a tube with a constant flow rate can be written as:

$$Q = \frac{\pi R^3 (\tau_w - \tau_0)^{1/n+1}}{C^{1/n} \tau_w^3} \left[\frac{(\tau_w - \tau_0)^2}{1/n + 3} + \frac{2\tau_0(\tau_w - \tau_0)}{1/n + 2} + \frac{\tau_0^2}{1/n + 1} \right] \quad (6-3)$$

With R the radius of the tube.

The relation between the pressure difference (ΔP_{tot}) and the wall shear stress (τ_w) in the capillary tube can be written as:

$$\Delta P_{tot} = 2\tau_w \frac{L}{R} + 0.5\rho \left(\frac{Q}{\pi R^2} \right)^2 \quad (6-4)$$

With L the length of the capillary tube.

ΔP_{tot} in this model is determined by the hydrostatic pressure minus the shear stress in the conical section and will be calculated later. Equation (6-4) can be written as:

$$\tau_w = 0.5 \frac{R}{L} \left[\Delta P_{tot} - 0.5\rho \left(\frac{Q}{\pi R^2} \right)^2 \right] \quad (6-5)$$

The first term on the right-hand side of this formula describes the total driving pressure that is independent of Q , the second term describes the dynamic part which is proportional to Q^2 .

Equations (6-3) and (6-5) describe the relation between Q and τ_w . This is an implicit relation which has to be solved numerically. Here an iterative method is used with under-relaxation. This method reduces oscillations in the solution and helps keep the computation stable. Without under-relaxation the iterative method would follow this

procedure: assuming a starting value of τ_w , Q is calculated with Equation (6-3), with this Q , τ_w is calculated using Equation (6-5) and this τ_w is used again in Equation (6-3). With under relaxation the new value of τ_w is a combination of the new $\tau_{w\ new}$ and the previous $\tau_{w\ old}$ according to the relation:

$$\tau_w = \beta\tau_{w\ new} + (1 - \beta)\tau_{w\ old} \quad (6-6)$$

In this relation β is a number between 0 and 1. In the calculations presented here, β is equal to 0.02 or even smaller for very low viscosity liquids like water.

The total pressure difference (ΔP_{tot}), corrected for the difference in height over the capillary tube in this model is determined by the hydraulic pressure difference in the entire funnel minus the contribution of the shear stress in the conical section that causes the slurry flow to be restrained due to the presence of the sidewalls. The principle can be shown in the equation below:

$$\Delta P_{tot} = \rho g(z + L) - F(\tau_0, \alpha, z) \quad (6-7)$$

With g the acceleration of gravity, $F(\tau_0, \alpha, z)$ the function representing the upward pressure induced by the sidewall in the conical section, z the height from the top of the capillary tube to the liquid surface at that moment and α the angle between the funnel wall and the vertical direction.

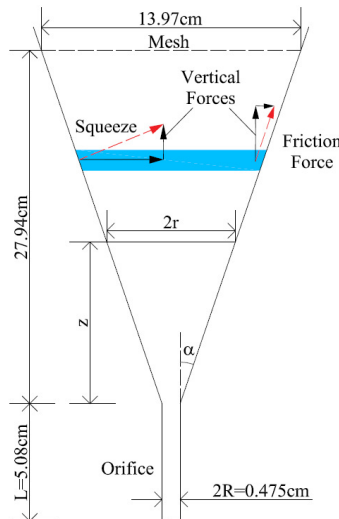


Figure 6-3. Vertical forces on a layer of slurry due to friction and ‘squeeze’

On closer examination, the function (F) has two components. The first component is that the slurry is restrained due to the presence of the sidewalls. The second component is that the slurry is ‘squeezed’ when the liquid height decreases, and the diameter of the slurry will become smaller. The first component gives a force that is shown on the right-hand side of Figure 6-3 and the second component is shown on the left-hand side. The friction force is equal to the yield stress τ_0 of the material and it induces a vertical stress on the fluid. The squeezing force perpendicular to the side wall is according to plasticity theory approximately 2 times τ_0 which also results in a vertical stress. The total upward pressure induced by the two components can be written as:

$$dF = 2\tau_0 \left[\frac{dz}{r} + 2 \frac{dz}{r} \tan \alpha \right] \quad (6-8)$$

With r the local radius.

Since r and z are related according to $z = (r-R)/\tan \alpha$, Equation (6-8) can be written as:

$$dF = 2\tau_0 \left[\frac{dr}{r \tan \alpha} + 2 \frac{dr}{r} \right] \quad (6-9)$$

Integration from R to r results in:

$$F = 2\tau_0 \left[\frac{1}{\tan \alpha} + 2 \right] \ln \left(\frac{r}{R} \right) \quad (6-10)$$

Combing Equation (6-10) with Equation (6-7) yields:

$$\Delta P_{tot} = \rho g(z+L) - 2\tau_0 \left[\frac{1}{\tan \alpha} + 2 \right] \ln \left(\frac{r}{R} \right) \quad (6-11)$$

With the Equations (6-3), (6-5) and (6-11) it is possible to calculate the flow and the slurry level in the funnel at every moment after the test is started.

In case there is a stagnation point which means the fluid in the funnel is not completely drained. The stagnation point in the funnel can be back calculated when the drained volume is known. The model can be used to calculate the yield stress (τ_0) of the fluid. When there is no flow, combining Equation (6-4) and (6-11) yields:

$$\tau_0 = \frac{\rho g(z+L)}{2 \left[\ln \left(\frac{r}{R} \right) \left(\frac{1}{\tan \alpha} + 2 \right) + \frac{L}{R} \right]} \quad (6-12)$$

Mathematically, in Equation (6-12) there is a lowest value of τ_0 as z increases from 0 to maximum (27.94 cm) assuming there is a stagnation point in the funnel. Below this value, there will be a complete drainage in the funnel. The lowest yield stress can be found with the Microsoft Excel's SOLVER function by finding the smallest value and it is $11.44\rho/\rho_w$ with ρ_w the density of water.

6.4 Experimental verification

An improved testing system (Figure 6-4) was designed and adopted for the test. As is shown in the figure, a device was placed beneath the tube. An electrical scale was used to measure the weight at a given time intervals of 0.2 second. The scale is connected to a computer for recording the outflow weight as a function of time.

After the funnel is filled, the finger is removed, and the fluid will flow out of the tube. In a conventional Marsh funnel test without the added device, the fluid gets velocity due to the dynamic pressure and “hits” the bottom of the container, creating an impact force, which, together with the weight of the slurry, can be measured by the digital scale. With the added device, the impact force due to the dynamic pressure can be effectively eliminated, because the vertical component in the outflowing fluid is minimized. This impact force can be obtained by comparing the results through experiments with and without the added device.

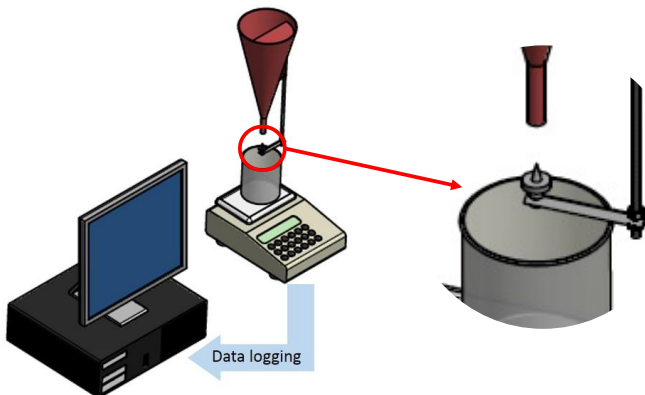


Figure 6-4. Testing system with the added device to eliminate the impact forces

Several kinds of bentonite slurries, including a slurry with polymer modified bentonite, were used in the experiment in order to get different rheological parameters. Water

and two different kinds of mineral oils were also used in the experiment as standard Newtonian fluids. Table 6-1 shows the used materials for the fluids.

Table 6-1. Materials and parameters found in the experiment

Fluid	Provider	Rheometer	Parameters		
			τ_0 (Pa)	C (Pa·s ⁿ)	n (-)
Water	UGent	Fann	0	0.001	1
		Funnel			
Multiswellable bentonite 6 wt%*	Wyo-Ben, Inc., USA	Fann	0.26	0.022	0.88
Natural Gel bentonite 6 wt%*	Hojun Corp., Japan	Funnel	0.26	0.022	0.96
		Fann	1.7	0.081	0.7
Polymer modified bentonite 5 wt%*	UGent	Fann	1.74	0.084	0.79
		Funnel	3.3	0.66	0.56
White mineral oil	Amazon.de	Fann	1.51	0.43	0.65
		Funnel	0	0.03	1
Renoil 500-W (high viscosity)	Renkert Oil, LLC, USA	Fann	0	0.037	1
		Funnel	0	0.23	1
Mineral oil†	-	Fann	0	0.26	1
Bentonite 8.6 wt%†	-	Fann	0	0.19	1
HPAM 1 wt%†	-	Fann	11	0.69	0.74
		Fann	0	7	0.27

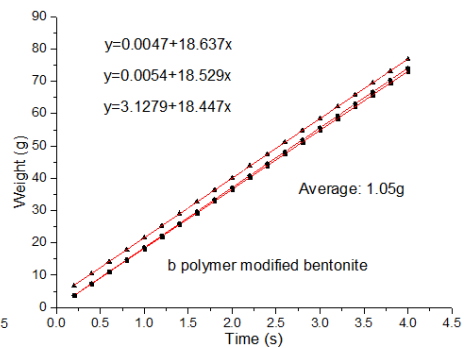
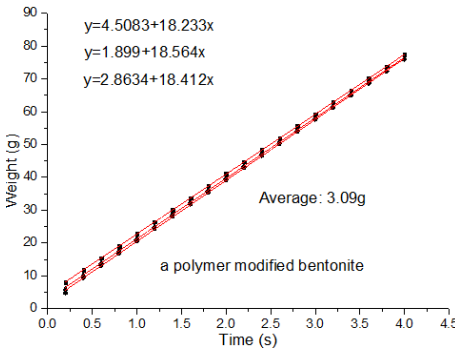
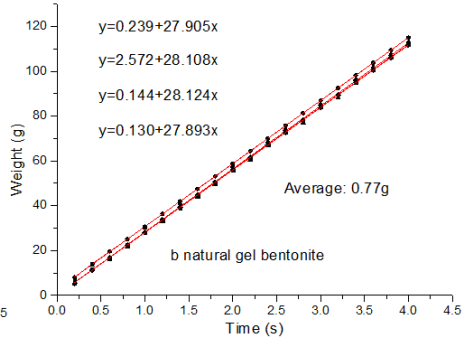
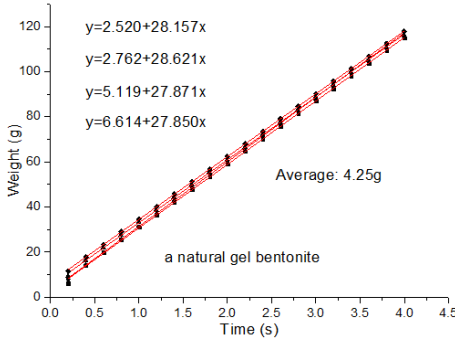
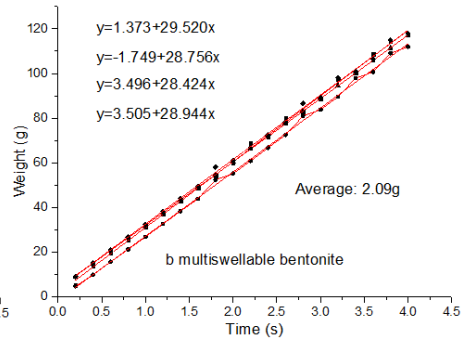
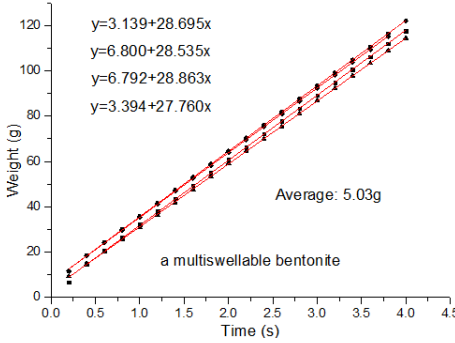
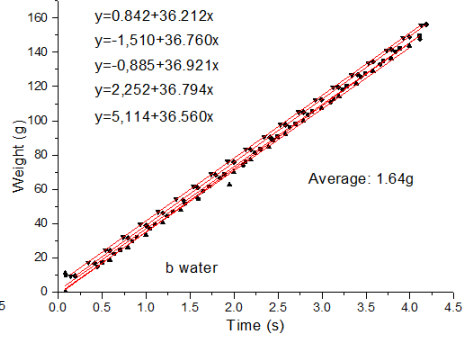
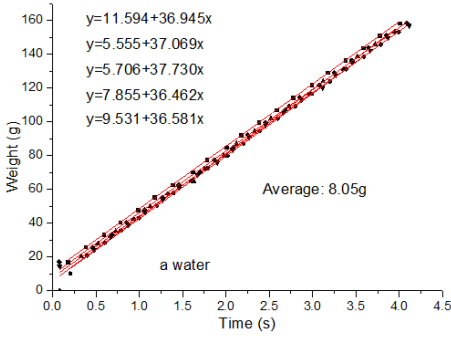
* The bentonite slurries were prepared according to API (2009).

† Experimental results from Balhoff et al. (2011).

A series of tests were carried out in order to obtain the parameters required in the model as well as the MF time for each fluid. The testing procedure for each fluid is briefly introduced below:

1) The fluid was tested with the Fann Model 35 viscometer to acquire the shear stresses under 6 different shear rates. The obtained data were fit into the Herschel-Bulkley model to get the Herschel-Bulkley parameters (τ_0 , C and n). Results are presented in Table 6-1.

2) The density of the bentonite slurries was determined with a mud balance and a pycnometer for mineral oils.



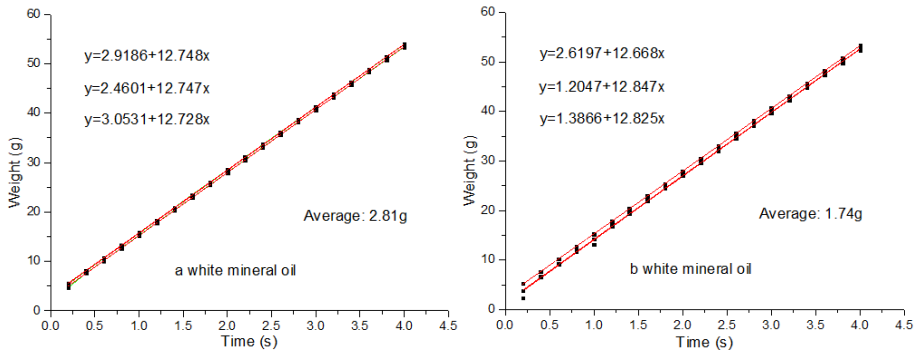


Figure 6-5. Weight versus time data for different fluids during the first 4 seconds of the test and impact forces extrapolated from measured data (a-without the added device; b-with the added device)

3) The Marsh funnel test was performed first with the added device and then without the added device for the second time. Impact force will be obtained by extending the trend lines of the weight-time data points from the first 4 seconds (linearly distributed) to intersect the y-axis. The difference in the intercepts between the tests with and without the added device will be the impact force due to the dynamic pressure. Figure 6-5 shows an example of the procedure. This procedure was repeated 3-5 times and the average value was taken in order to minimize the noise from the test. In case of a high viscosity fluid, the dynamic force will be too small to be measured. Therefore, the measurement on dynamic force was not conducted with Renoil 500-W.

Table 6-2. Experimental and numerical results

Fluid	Dynamic force ($\times 10^{-2}$ N)		MF time (s)			
	measured	predicted	measured	predicted	predicted without dynamic force	Balhoff et al. (2011)
Water	5.4	6.2	27	22.8	1.2	1.2
Multiswellable bentonite 6 wt%	3.7	2.9	36	28.4	9.4	9.4
Natural Gel bentonite 6 wt%	3.7	3.4	38	28.8	6.8	6.6
Polymer modified bentonite 5 wt%	1.8	2.0	58	42.8	24.6	24
White mineral oil	1.1	0.8	67	58.2	49.6	49.6
Renoil 500-W (high viscosity)	-	-	399	357	355.8	355.8
Mineral oil	-	-	-	297.2	295.4	295.4
Bentonite 8.6 wt%	-	-	-	365.6	337.6	286.8
HPAM 1 wt%	-	-	-	58.2	32.2	32.2

Table 6-2 and Figure 6-6 show the measured values and those determined from the new model based on Equations (6-3), (6-5) and (6-11). Specifically, Figure 6-6a shows that all the data points lie within the $\pm 30\%$ bounds around the line of equality. Also, the dynamic force of the tested fluid will decrease when the MF time increases, indicating that the influence from the dynamic force will be rather limited when the MF time is large. To explore how this dynamic part influences the model prediction, the MF times of the tested fluids were calculated and compared to the model predictions when the dynamic part is not included. When the dynamic force is not considered, Equation (6-5) will be replaced by:

$$\tau_w = 0.5 \frac{R}{L} \Delta P_{tot} \tag{6-13}$$

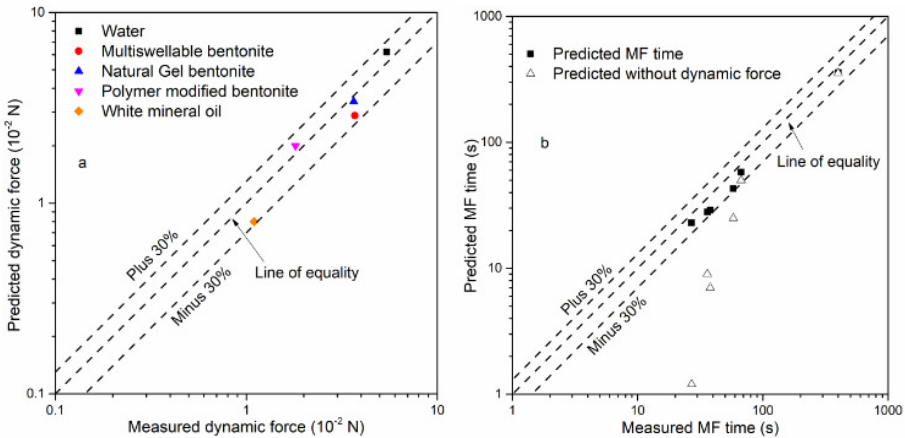


Figure 6-6. Comparison between measured and predicted dynamic forces and MF times

Figure 6-6b shows the measurement results as well as the model results considering and not considering the dynamic force. From Figure 6-6b it can be seen that the dynamic part plays an important role in model predictions when the measured MF time is less than 60s. The influence from the dynamic part is not clear when the MF time is large as is shown in the results of Renoil_500 W. Figure 6-6b shows that although the simulation data points (predicted with dynamic force) represent under-predictions by the model compared to measurement data, the overall match is good. The general agreement between model prediction and experimental result suggests that the model can be used in a wide range of applications from small to large values

with respect to the measured MF time.

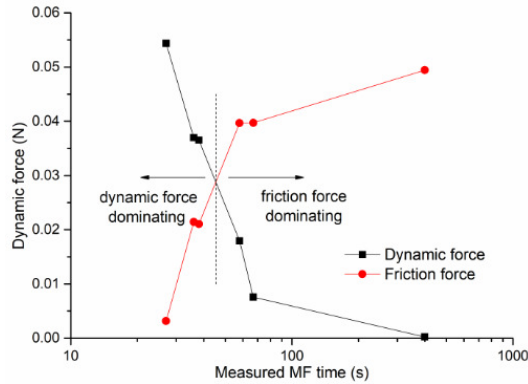


Figure 6-7. Comparison between calculated dynamic force and calculated friction force

Meanwhile, by comparing the dynamic force and the friction force in a Marsh Funnel test, as is shown in Figure 6-7, we are able to tell that dynamic force dominates for fluids with small MF values in a Marsh Funnel test. With increasing MF values, the friction force increases, and the dynamic force decreases since the discharge Q decreases. The friction force becomes dominating at a MF time of around 50 seconds. This means that for bentonite slurries with a MF time at around 30-45s, the dynamic force dominates and should be taken into consideration with respect to modelling.

6.5 Discussion

The dynamic part described in the model plays an important role in case of small Marsh funnel values, which is in line with the numerical solution provided by Pitt (1999) when power law model was assumed. However, the power law model does not incorporate the yield stress that is typical in a non-Newtonian fluid. While the model presented in this chapter also considers the pressure drop due to the yield stress in the conical section of the funnel. The dynamic force and the friction force in the capillary tube are determined by numerical iteration.

Balhoff et al. (2011) developed a model in which the MF time can be estimated with the rheological parameters of a fluid. The Balhoff et al. (2011) model predictions are also included in Table 6-2 as a comparison. Because the dynamic force is not included, Table 6-2 shows that the Balhoff et al. (2011) model gives lower predictions on the

MF time compared with the model in this study. Moreover, it shows that the results by the Balhoff et al. (2011) model are quite comparable to the model predictions in this study when the dynamic part is not included. Specifically, for fluids without yield stress, the model by Balhoff et al. (2011) gives same results to the predictions with the model in this study when the dynamic part is not included. For other fluids with yield stresses (except for Multiswellable bentonite 6 wt%), the Balhoff et al. (2011) model predictions are a bit smaller than the predictions with our model when the dynamic part is not included.

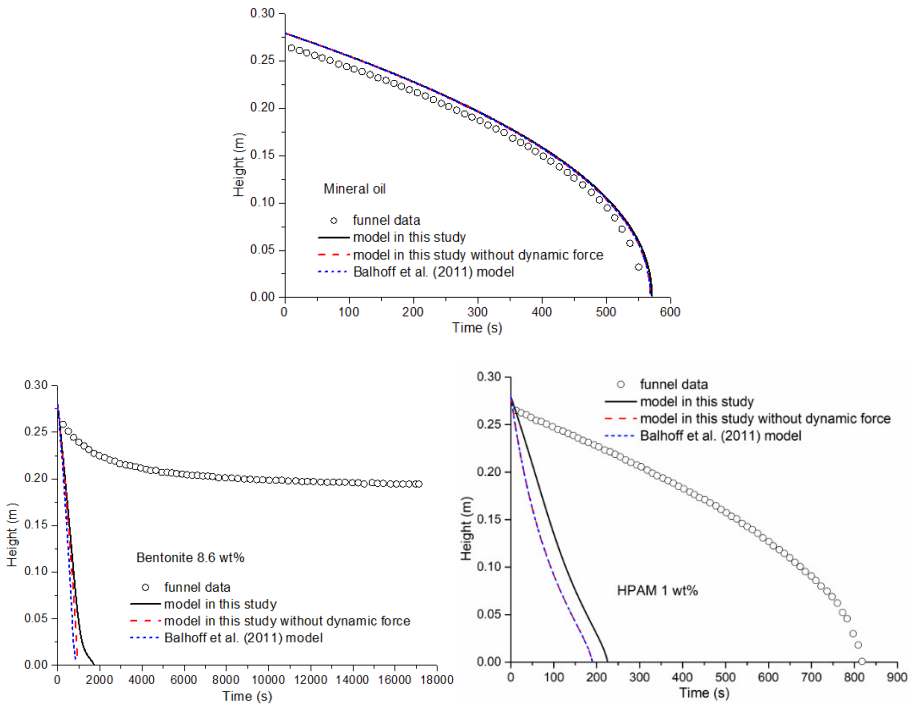


Figure 6-8. Fluid height in the conical section funnel data for different fluids (from Balhoff et al., 2011) compared to model results.

Figure 6-8 shows the measurement data from Balhoff et al. (2011) compared with the different model predictions. The Herschel-Bulkley parameters of the fluids are included in Table 6-1 and are used in the model predictions. In general, Figure 6-8 presents similar conclusions that are discussed above. For fluids without yield stress (Mineral oil and HPAM 1 wt%), the model by Balhoff et al. (2011) gives same results to the predictions with the model in this study when the dynamic part is not included,

while for fluids with yield stress (Bentonite 8.6 wt%), the Balhoff et al. (2011) model predictions are smaller than the predictions with our model when the dynamic part is not included. The difference is clear as is shown in Table 6-2 and Figure 6-8.

This difference in model predictions with the yield stress fluids could be induced by the different treatment on the pressure loss due to yield stress in the conical section of the funnel (ΔP_{cone}). In Balhoff et al. (2011), this term is calculated:

$$\Delta P_{cone} = \frac{2H_F}{R_F} \tau_0 \quad (6-14)$$

With H_F the maximum filling height of the conical section of the funnel and R_F the maximum radius.

While in our model, this term is expressed in Equation (6-10), different from Equation (6-14). The difference is relevant to the yield stress. Therefore, the pressure loss due to yield stress in the conical section of the funnel with both Equation (6-10) and (6-14) were plotted in Figure 6-9.

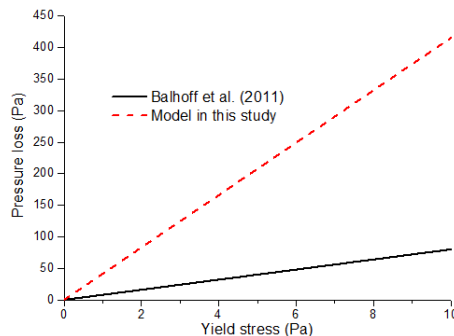
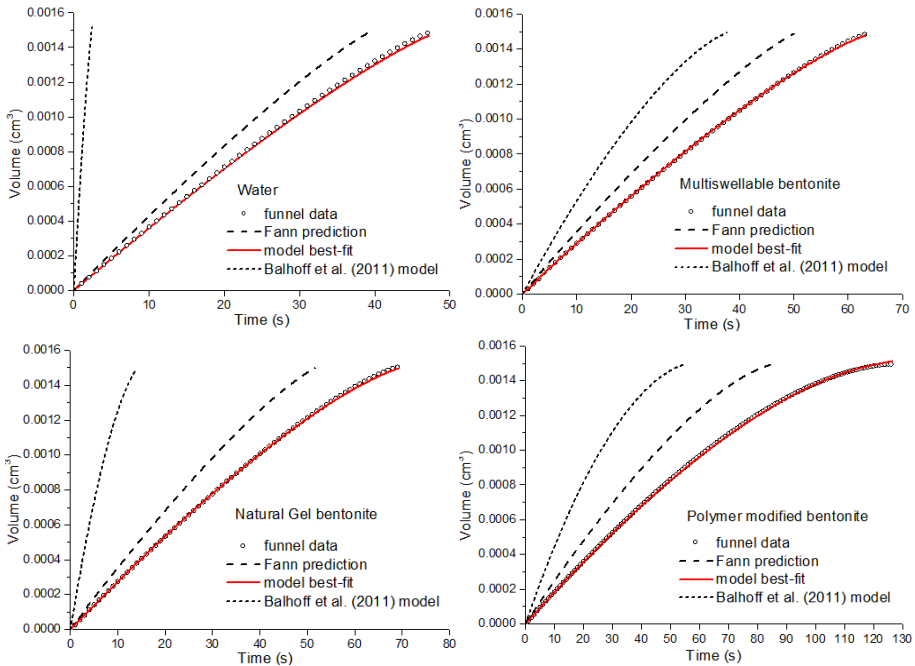


Figure 6-9. Pressure loss due to yield stress in the conical section in the model of Balhoff et al. (2011) and this study.

Figure 6-9 shows that the maximum possible pressure loss due to yield stress in the conical section is larger in the model of this study, and the difference is larger with increasing yield stress. This explains that for Multiswellable bentonite with a small yield stress, the Balhoff et al. (2011) model gives same prediction to that with our model when the dynamic part is not included. While for the other three fluids (Natural Gel bentonite 6 wt%, Polymer modified bentonite 6 wt% and Bentonite 8.6 wt%) with larger yield stresses, the Balhoff et al. (2011) model predictions are a bit smaller.

The different treatment on the pressure loss due to yield stress also influences the yield stress measurement when there is a stagnation point after the test. The smallest yield stress can be measured by the Balhoff et al. (2011) model is $11.65\rho/\rho_0$, which is slightly bigger than that in our model ($11.44\rho/\rho_0$).

Although the new model broadens applications both in measured MF times and in fluid types, it should be noted that it is used for the prediction in MF test with the rheological parameters as an input. Further application making use of the measured MF test data for the prediction of the rheological parameters could be realized with the Microsoft Excel’s SOLVER function. The rheological parameters of the tested fluid can be found by fitting the model results to the measured data points of the MF time and the total drainage time. Parameter estimation is performed by finding a least-squares fit of the volume versus time data to the solution of the model (Equations (6-3), (6-5) and (6-11)). Some constraints regarding the yield stress and the flow index should be considered as there is no stagnation point at the end of the test ($\tau_0 < 11.44\rho/\rho_0$) and the bentonite slurries are shear thinning fluids ($n < 1$). The rheological parameters found by the funnel data were listed in Table 6-1.



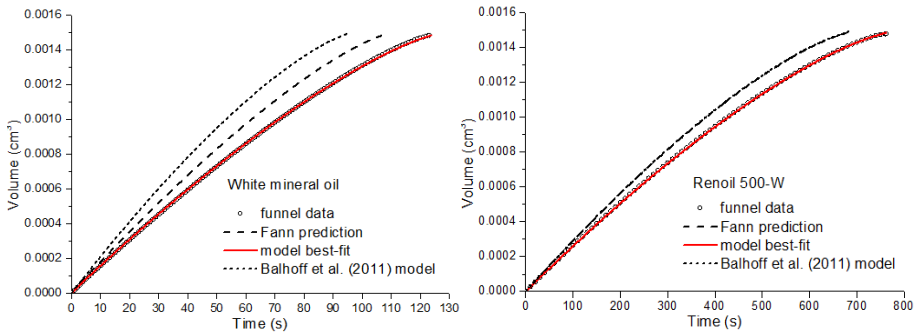


Figure 6-10. Volume versus time funnel data for different fluids compared to model results.

Figure 6-10 shows the measurement and the model results using both the Fann viscometer parameters and the funnel data (MF time and total drainage time). It can be seen that the model results using the funnel data could perfectly match the experimental results, suggesting the right physics of the new model. The Balhoff et al. (2011) model results were also included in the figure. It shows that for fluids with small MF values, the Balhoff et al. (2011) model gives large deviations to the model presented in this study. While for high viscosity fluids (such as Renoil-W and Mineral oil in Figure 6-8a), the results by the two models are almost identical. This suggests that the dynamic force should be considered with small MF values and can be neglected with large MF values. Figure 6-10 also indicates that for field use, two measuring points (MF time and total drainage time) from the Marsh funnel test can be utilized for estimating the rheological parameters with the new model.

6.6 Chapter summary

A new model concerning the Marsh funnel test is proposed based on the Herschel-Bulkley model. The new model considers both the friction force and the dynamic force. An improved testing system has been utilized for the measurement of the dynamic force. A series of tests has been conducted to verify the model. From the experimental results and the model predictions, it can be concluded:

1) The new model does a good job in predicting the dynamic force and the MF time of the tested fluids. Although the model slightly underpredicts the MF time, general agreement was found when comparing with measurement data. The tested MF time ranges from 27-399 s, covering most applications in different fields such as tunneling,

grouting and oil industry. Indicating that the model can be used in a wide range of applications.

2) For a fluid with a small MF time that can be expected in a slurry shield TBM, where the slurries typically possess small MF values between around 30 ~ 45s, the influence from the dynamic force is significant. As a consequence, the dynamic force should be considered in modelling work and the proposed model is suggested for further research.

3) The yield stress can be estimated with the new model when there is a final stagnation point after the test. Owing to the shear rate naturally reduces to 0, it could be a better approach compared with other testing methods in which extrapolation is used for estimating the yield shear stress.

Chapter 7 Closing remarks

The research presented in this thesis consists of studies on the fluid problems that could be encountered in TBM excavations. It includes models, experiments and field measurements. The main contribution is the better understanding on the physics of the foam infiltration behaviors during pure foam and sandy foam infiltration, as well as the fluid flow in a Marsh funnel test. Although conditions may be much more complex in field applications, this research has provided sound descriptions on the mechanisms that govern the flow behaviors.

7.1 Summary

In this thesis, foam infiltration behaviors in relation to the EPB shield TBM were first experimentally and theoretically studied. The results with pure foam infiltration were compared with the field measurement data from the Botlek Rail tunnel and better understanding on the pressure development at the tunnel face was obtained. The mechanisms during pure foam infiltration were discussed and theoretically explored. With a better understanding on pure foam infiltration, the infiltration behaviors from sandy foam to saturated sand were studied with several influencing factors including FIR, water content in the mixture and sand type. Mechanisms were discussed and the potential foam penetration behavior was predicted with the model for bubble penetration. The change in surface tension of the foam due to dilution was investigated and its influence on the infiltration behavior was studied.

In the second part a new model regarding the Marsh funnel test was established, which is more applicable in evaluating the bentonite slurries for the slurry shield TBM. The new model accounted for the pressure drop in the upper conical section due to the yield stress of the fluids as well as the dynamic pressure in the lower capillary tube. Validation tests were conducted to demonstrate the dynamic pressure in the beginning of the test. Comparison with some previous models has shown the advantage of the new model. Further application by making use of the measured MF data for a fast estimation of the rheological parameters for the tested fluid was discussed.

7.2 Conclusions and recommendations for future work

Major conclusions throughout this study can be summarized as follows:

1. Foam spurt in the beginning of pure foam infiltration results in a low permeable layer that will take most of the excess pore pressure. Pressure redistribution can be expected when foam bubbles penetrated the soils. The low permeable layer functions similarly to a filter cake in a slurry infiltration, and the support pressure can be effectively transferred to the soils at the tunnel face.

2. Further infiltration is the main process after foam spurt in a pure foam infiltration. During further infiltration, there is an increase in the total discharge while the pressure distribution in the foam infiltration zone is stabilizing. The measured pore pressures ahead of the foam front shows some minor changes due to bubble infiltration. This can be similar to the deep bed filtration in a slurry infiltration where bentonite particles are retained in the pores that the permeability of the sand decreases slowly. However, bubbles will not adhere to the sand grains but only get entrapped in the pores due to its larger volume compared with the pore throats. The coalescence of the foam bubbles in the sand is the possible reason that the pressure redistribution could happen during the further infiltration process as can be found from experiments.

3. The model study on foam flow into saturated sand provides a good way to quantify the foam infiltration behavior during foam spurt. The good agreement between model and experimental results suggests that the model describes the right physics of the foam spurt process that can be expected in field applications. The pore pressures and water leakage under such conditions can be predicted with the model which could be a starting point for the work on soil-foam-TBM interactions.

4. Consolidation of the foam-sand mixture is the dominating process that results in a consolidated mixture with a smaller permeability. In case there is foam penetration into the sand, the consolidated mixture close to the sand surface has a lower permeability than that away from the sand surface. Probably because the consolidated mixture close to the sand surface is subjected to a considerable bubble loss that has a denser sand content. However, a kind of fracturing by fracture of air occurs when all mixture is consolidated. This phenomenon is also reported from experiments with

bentonite slurry when slurry mixed with sand is used.

5. Sand matrix plays an important role in determining the permeability of a foam-sand mixture. In case there is foam penetration into the sand, there can be three layers with different permeabilities. This was ensured by the comparison on the permeabilities among the foam infiltrated sand, consolidated mixture close to the sand surface and that far away from the sand surface. The permeability is smallest in the foam infiltrated sand and largest in the consolidated mixture away from the sand surface.

6. Bubble penetration is influenced by the ratio between the permeability of the foam-soil mixture and the soils at the tunnel face. For a foam-sand mixture with a small FIR, the permeability will not be small enough to create a sufficient pressure gradient to initiate the foam penetration. This was confirmed in combination with the model for pure foam infiltration and experimental results.

7. The change in surface tension due to dilution in tunneling could influence the foam penetration behavior, while its influence on the compressibility of the foam-sand mixture is negligible. Experiments on sandy foam infiltration has shown that the bubble penetration can be influenced by its surface tension.

8. The new model regarding the Marsh funnel test has shown to be especially feasible to its tunneling applications since the dynamic force is incorporated in the model in combination with the Herschel-Bulkley flow model. The dynamic force was proved to be the dominating force for the bentonite slurries with a small MF value. In addition to that, the model has the advantage for the testing of fluids with a yield stress to which the pressure drop in the upper conical section is mainly related. The yield stress can be estimated with the new model when there is a final stagnation point after the test. Owing to the shear rate naturally reduces to 0, it could be a better approach compared with other testing methods in which extrapolation is used for estimating the yield shear stress.

Further experimental and theoretical work is required to establish a higher level of understanding on the foam-soil interaction as well as the Marsh funnel test. Some recommendations can be summarized:

1. Further experiments on pure foam infiltration with the same sand column while

different densities. The results from sandy foam infiltration have shown that the sand matrix plays an important role in determining the permeability of a foam-sand mixture. The sand column with different densities represents the difference in sand matrix. By comparing the permeabilities of the foam-infiltrated sand, more information could be obtained.

2. Further experiments on sandy foam infiltration with sand columns at different hydraulic gradients could provide more information to this conclusion. It was shown that the bubble penetration is influenced by the ratio between the permeability of the foam-soil mixture and the soils at the tunnel face. The hydraulic gradient is only 1 with a shield diameter of 10 m and an extra pore water pressure of 50 kPa. In the experiments, this was achieved by adding a small cylinder at the bottom to create an extra flow resistance. To better illustrate, comparison tests with different hydraulic gradients in order to get different k_s / k_m could provide more information on this conclusion.

3. Further mixing tests with different combinations of foam, water and sand. In the results with sandy foam infiltration, it was shown that increasing the FIR could promote the foam infiltration which can be beneficial for tunnel face stability and pressure maintenance during standstill. However, a higher FIR may lead to the poor mixing of a mixture in which the water, the foam bubbles and the sand grains separate from each other in an unstable state. This requires further experimental work as well as physical models to better understand the mixing process and the influencing factors such as mixing time and mixing pattern. In this way, the governing parameters that define a ‘good mixture’ could be revealed which will definitely benefit the engineers as well as the operators in a TBM operation.

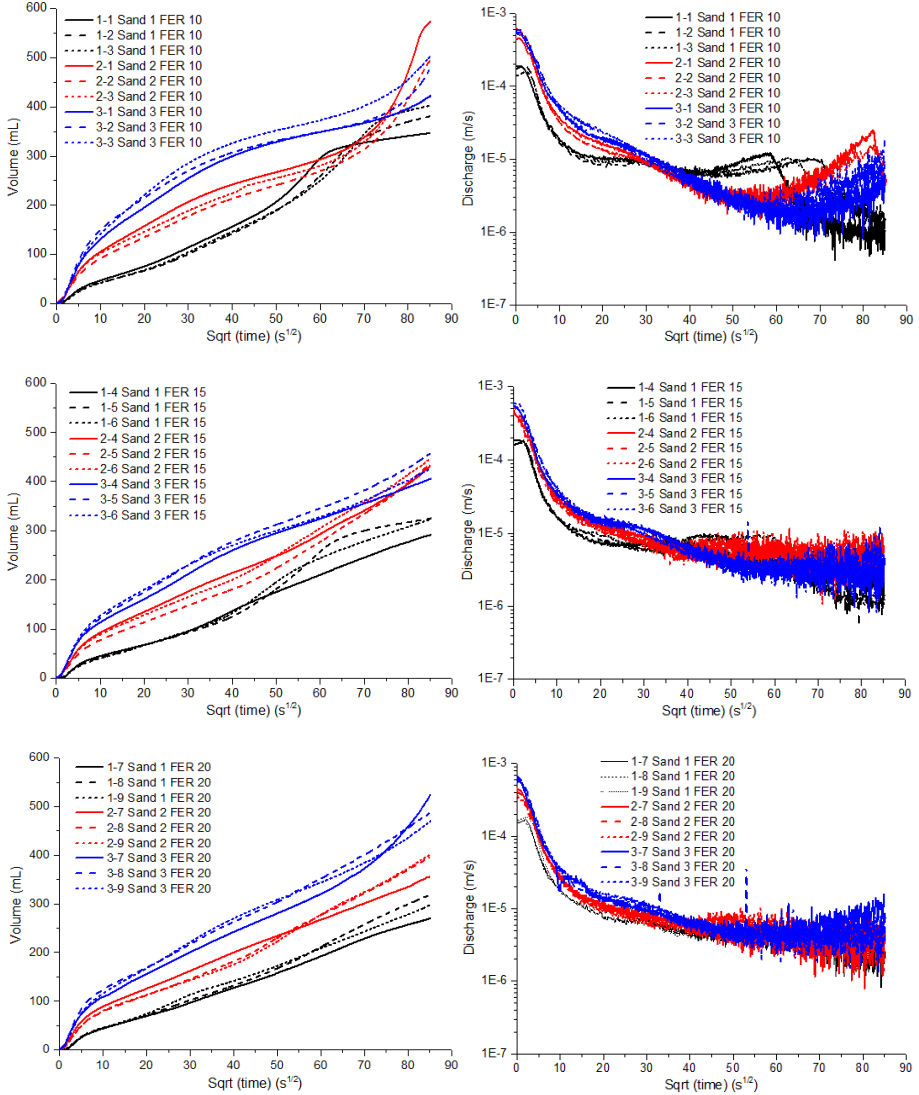
4. Further work on characterizing the rheological properties of foam. The model on the pure foam infiltration simplifies the foam flow to be a Bingham liquid, which might not be the case. The yield stress of pure foam may not be detected with existing measuring technics due to the larger dimensions compared with the foam bubbles. While the foam bubbles are relatively large in its flow through the pores of the sand. This may require a new concept to define the bubble flow in porous media.

5. Further work on the Marsh funnel test can be focused on the characterization of the influence from the entrance effect. As shown in Chapter 6, the new model underestimated the MF times within 30%, this can be related to the entrance effect from the upper cone section to the capillary tube. Both numerical and experimental work could be conducted to clarify the influence, which might be optimized by new dimensions that is more compatible with the proposed physical model.

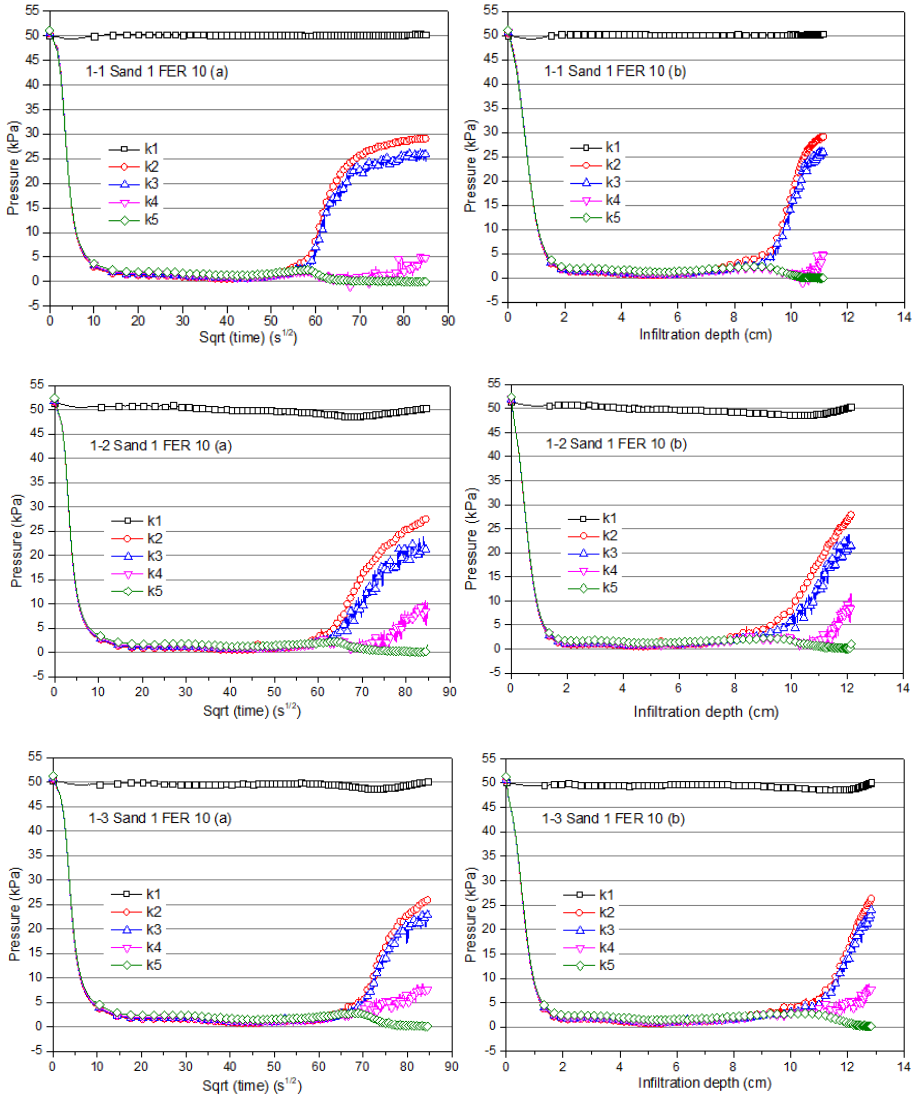
6. Combining the two parts of the thesis, a modified Marsh funnel test could be developed to characterize the rheological properties of the foam-sand mixture. At present, the slump test is widely used to assess the plasticity and the mass behavior of the foam-sand mixture. However, there is now a lack in a field-testing method suitable for the rheological aspects of a foam-sand mixture. To apply, the Marsh funnel has to be changed with a larger opening of the capillary part. This can be further developed combining the improved understanding over the Marsh funnel test shown in Chapter 6.

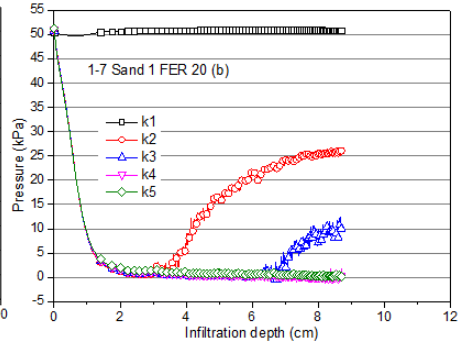
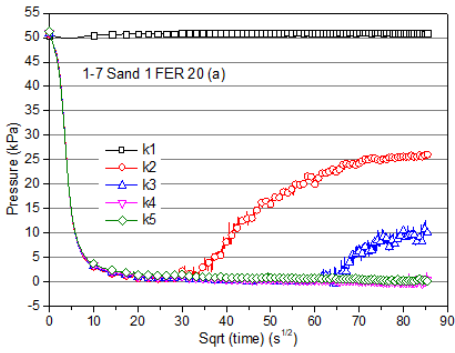
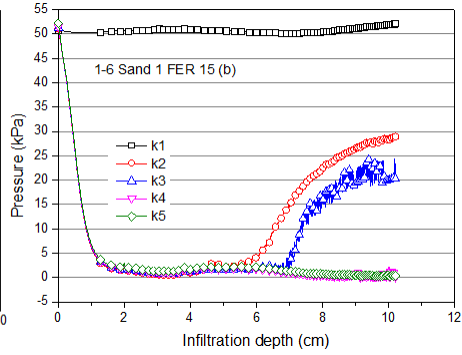
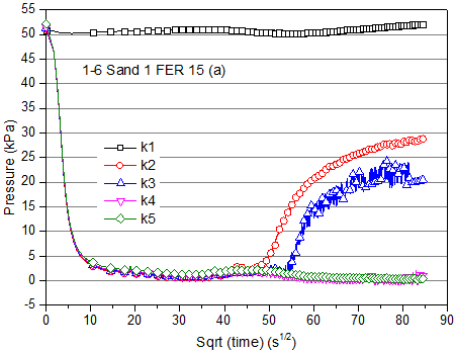
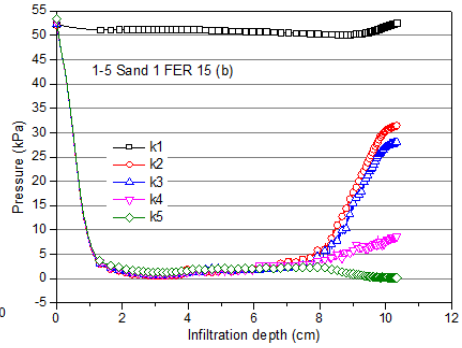
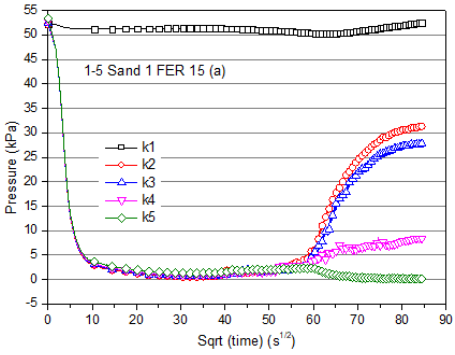
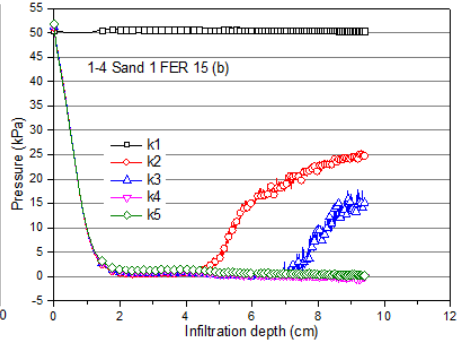
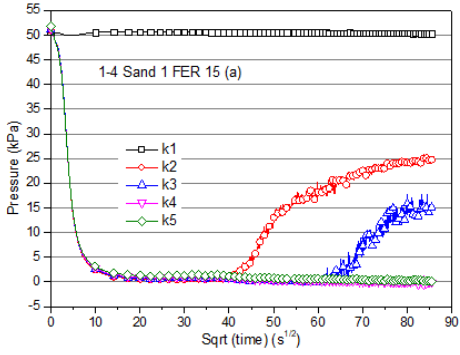
Appendix: results for all pure foam infiltration tests

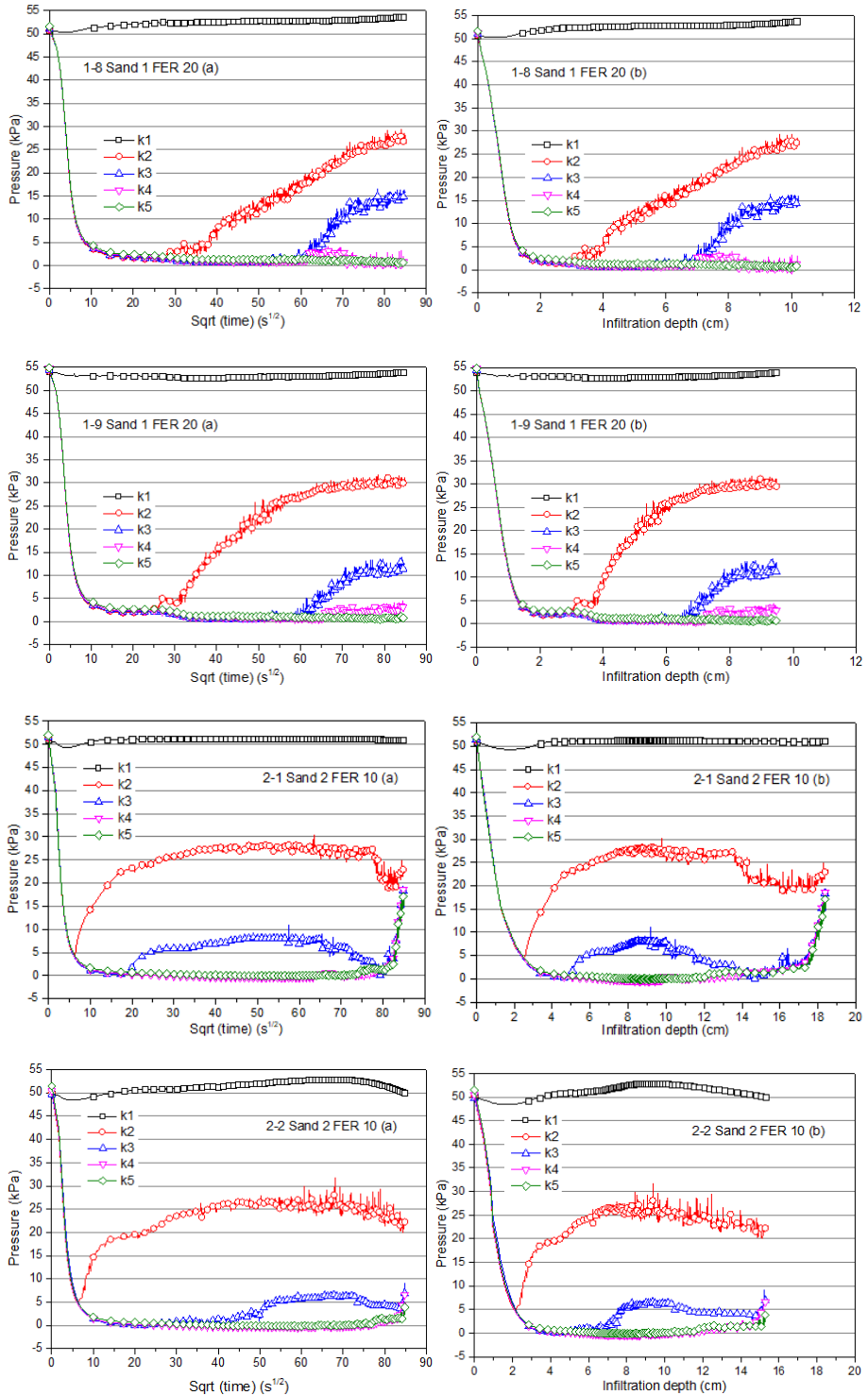
Discharge

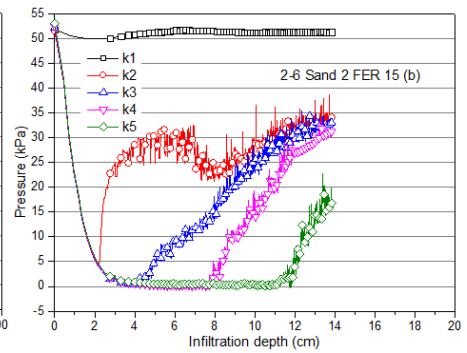
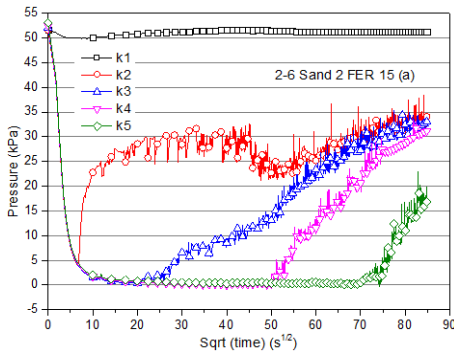
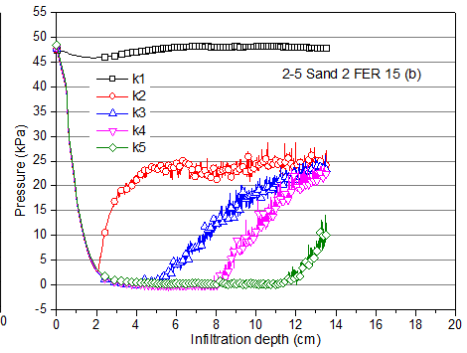
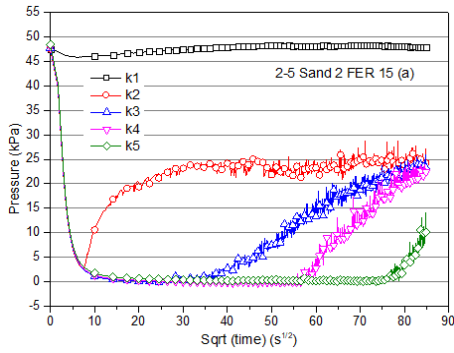
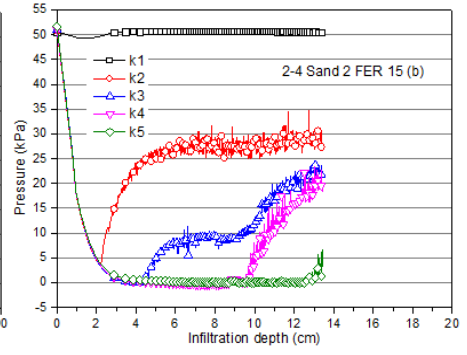
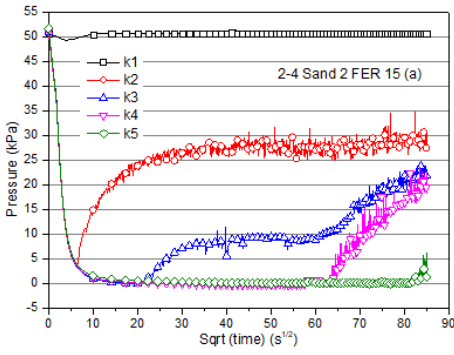
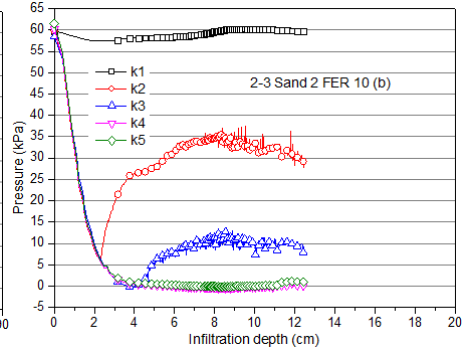
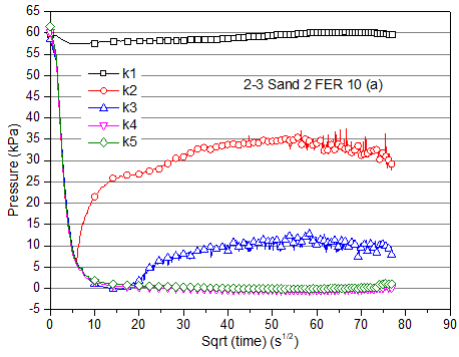


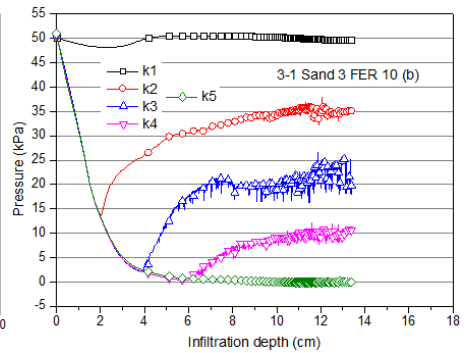
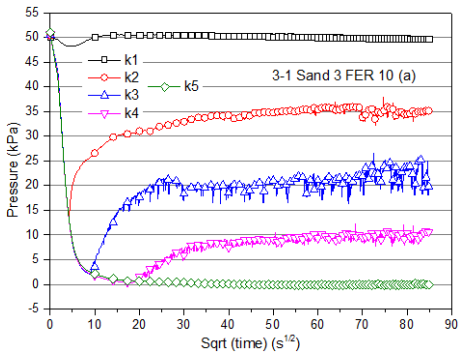
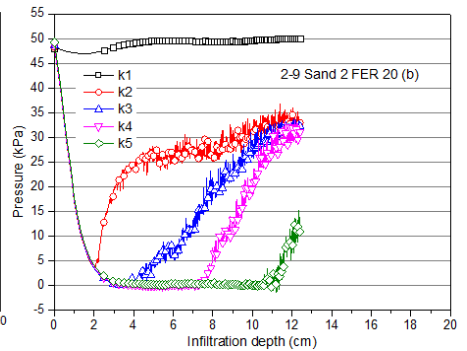
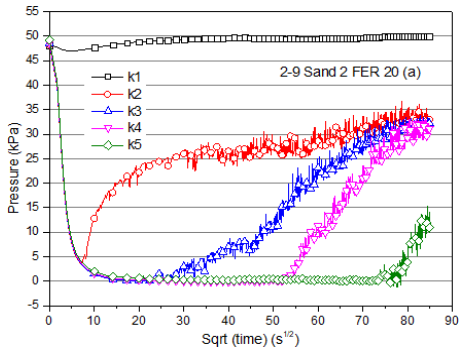
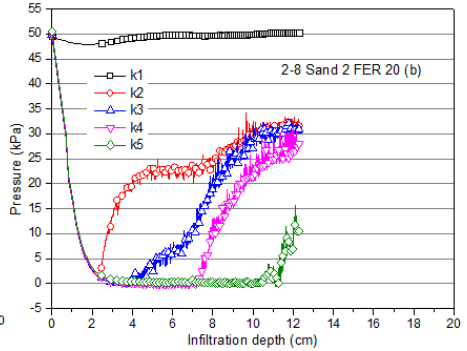
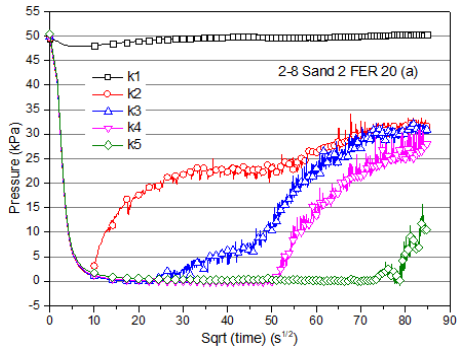
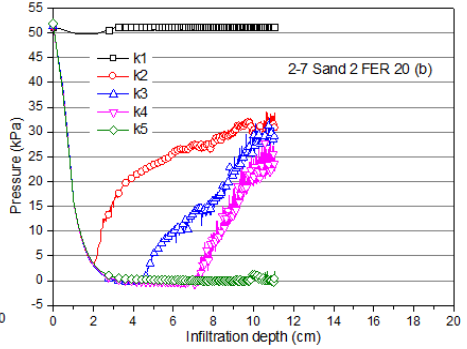
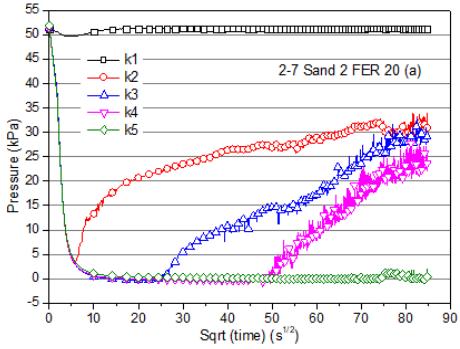
Pore water pressures

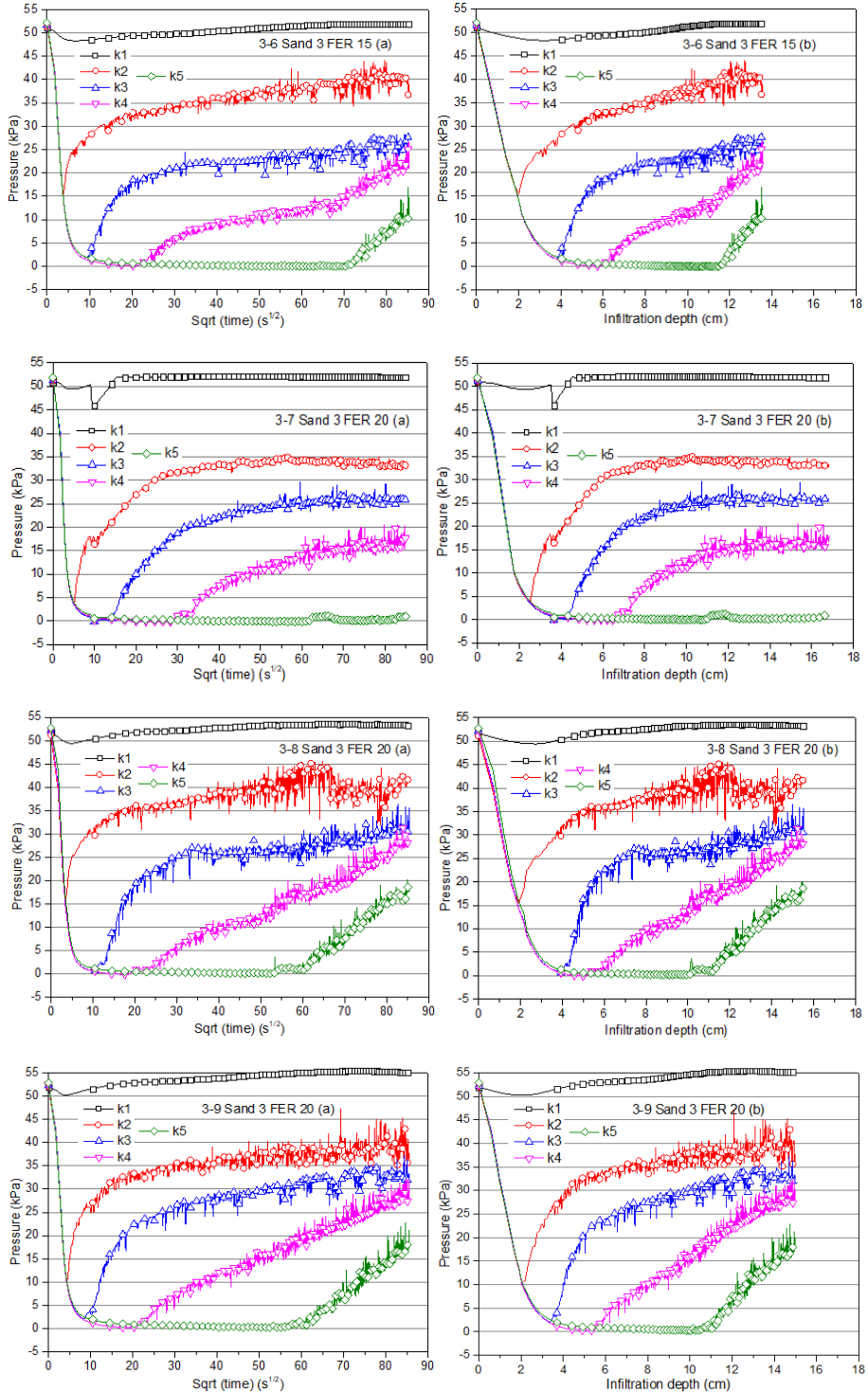












References

- Anagnostou, G. & Kovári K., 1994. The face stability of slurry-shield-driven tunnels. *Tunnelling and Underground Space Technology* 9 (2): 165-174.
- Anagnostou, G. & Kovári K., 1996. Face Stability Conditions with Earth-Pressure-Balanced Shields. *Tunnelling and Underground Space Technology* 11 (2): 165-173.
- API (American Petroleum Institute). 2009. Recommended practice for field testing of water-based drilling fluids. 4th ed. API RP 13B-1. Washington, DC: API.
- Balhoff M.T., Lake L.W., Bommer P.M., Lewis R.E., Weber M.J. & Calderin J.M., 2011. Rheological and yield stress measurements of non-Newtonian fluids using a Marsh funnel. *Journal of Petroleum Science and Engineering* 77: 393-402.
- Bäppler, K., Battistoni, F. & Burger, W., 2018. Variable Density TBM – Combining Two Soft Ground TBM Technologies. *Geosource journal* 1: 21-27.
- Bezuijen, A., Schaminée, P.E.L. & Kleinjan, J.A., 1999. Additive testing for earth pressure balance shields. *Proc. 12th Eur. Conf. on Soil Mech. and Geotech. Engrg.*, Amsterdam, Balkema, Rotterdam, pp. 1991–1996.
- Bezuijen, A., Pruiksmá, J.P. & van Meerten, H.H., 2001. Pore pressures in front of tunnel, measurements, calculations and consequences for stability of tunnel face. *Proc. Int. Symp. on Modern Tunneling Science and Techn.* Kyoto.
- Bezuijen, A., 2002. The influence of soil permeability on the properties of a foam mixture in a TBM. *4th Int. Symp. on Geotechnical Aspects of Underground Construction in Soft Ground - IS Toulouse 2002.*
- Bezuijen, A., 2005. Pressure gradients and muck properties at the face of an EPB. *5th Int. Symp. on Geotechnical Aspects of Underground Construction in Soft Ground - Rotterdam.*
- Bezuijen, A., Pruiksmá, J. P. & van Meerten, H.H., 2006. Pore pressures in front of tunnel, measurements, calculations and consequences for stability of tunnel face. *Tunnelling. A Decade of Progress. GeoDelft 1995-2005*, 27-33.
- Bezuijen, A., 2010. Compensation grouting in sand: experiments, field experiences

- and mechanisms. Doctoral thesis. Delft University of Technology, The Netherlands.
- Bezuijen, A., 2011. Foam used during EPB tunneling in saturated sand, description of mechanisms. Proc. WTC, Helsinki.
- Bezuijen, A., 2012. Foam used during EPB tunnelling in saturated sand, parameters determining foam consumption. Proc. WTC, Bangkok.
- Bezuijen, A., 2013. Foam parameters in saturated sand, theory and model tests. Proc. WTC, Geneva.
- Bezuijen, A. & Talmon, A.M., 2014. Soil pressures at the cutting wheel and the pressure bulkhead of an EPB shield. Proc. 7th Int. Symp. Geotech. Aspects of Underground Construction in Soft Ground, Seoul.
- Bezuijen, A., Steeneken, S. P., et al., 2016. Monitoring and Analysing Pressures Around a TBM. Proc. 13th International Conference Underground Construction, Prague.
- Bezuijen, A. & Dias, T.G.S., 2017. EPB, chamber pressure dissipation during standstill. EURO: TUN 2017, Innsbruck University, Austria
- Bezuijen, A. & Xu, T., 2019. Foam soil interaction and the influence on the stability of the tunnel face in saturated sand. Tunnels and Underground Cities: Engineering and Innovation meet Archaeology, Architecture and Art.
- Bezuijen, A., 2020. Keynote Lecture: Soil-water-tunnel interaction at the front face of a TBM. Geotechnics for Sustainable Infrastructure Development, Lecture Notes in Civil Engineering 62, https://doi.org/10.1007/978-981-15-2184-3_26.
- Bezuijen, A., Dang, T.S. & Meschke, G., 2020. Asymmetric pressure distribution in EPB shields: Evaluation of measurements and numerical simulations. Proc. 10th Int. Symp. Geotech. Aspects of Underground Construction in Soft Ground, London. To be published
- Bezuijen, A. & Meschke G., 2020. Pressure distribution in the excavation chamber of an EBP shield. To be published. Proc. WTC 2020, Malaysia.
- Borio, L. & Peila, D., 2010. Study of the Permeability of Foam Conditioned Soils with

- Laboratory Tests. *American Journal of Environmental Sciences* 6 (4): 365-370
- Broere, W. & van Tol A.F., 2000. Influence of Infiltration and Groundwater Flow on Tunnel Face Stability. *Geotechnical Aspects of Underground Construction in Soft Ground*, Tokyo, Japan, 2000, pp. 339-344.
- Broere, W. & van Tol, A.F., 2001. Time-dependant infiltration and groundwater flow in a face stability analysis. In: *Proceedings of International Symposium on Modern Tunnelling Science and Technology*, Kyoto, pp. 629–634.
- Budach, C., Thewes, M., 2015. Application ranges of EPB shields in coarse ground based on laboratory research. *Tunnelling and Underground Space Technology*, 50: 296-304.
- Budach, C., Thewes, M., 2018. Application ranges of EPB shields in coarse ground based on laboratory research. *Tunnelling and Underground Space Technology*, 50: 296-304.
- EFNARC (ed.) (2005), *Specification and guidelines for the use of specialist products for mechanized tunnelling (TBM) in soft ground and hard rock*.
- Galli, M., 2016. Bochum Rheological characterisation of Earth-Pressure-Balance (EPB) support medium composed of non-cohesive soils and foam. Doctoral thesis. Ruhr-Universität, Germany.
- Galli, M., Thewes, M., Freimann, S. & Schröer, M., 2021. Residual water content of excavated soil in EPB tunnelling. *TUST*, 114 (2021): 103991. doi.org/10.1016/j.tust.2021.103991
- Guria C., Kumar R. & Mishra P., 2013. Rheological analysis of drilling fluids using Marsh funnel. *Journal of Petroleum Science and Engineering* 105, 62-69.
- Herrenknecht, M., Thewes, M. & Budach, C., 2011. The development of earth pressure shields: from the beginning to the present. *Geomechanics and Tunnelling* 4 (2011): 11-35
- Koehler, S.A., Hilgenfeldt, S. & Stone, H.A., 2004. Foam drainage on the microscale I. Modeling flow through single Plateau borders. *Journal of Colloid and Interface Science* 276 (2004): 420-438.

- Le Roy R. & Roussel N., 2005. The Marsh Cone as a viscometer: theoretical analysis and practical limits. *Materials and Structures* 38: 25-30
- Lins, Y., 2009. Hydro-Mechanical Properties of Partially Saturated Sand. Doctoral thesis. Ruhr-Universität, Germany.
- Magrabi, S.A., Dlugogorski, B.Z. & Jameson G.J., 1999. Bubble size distribution and coarsening of aqueous foams. *Chemical Engineering Science* 54 (1999): 4007-4022.
- Maidl, U., 1995. Erweiterung der Einsatzbereiche der Erddruckschilde durch Bodenkonditionierung mit Schaum. Doctoral Thesis, Ruhr-Universität Bochum, AG Leitungsbau und Leitungsinstandhaltung.
- Maidl, U., 1999. Design features of the Botlek Rail Tunnel in the Betuweroute. *Tunnelling and Underground Space Technology* 14(2): 135-140.
- Mair, R.J., 2011. Tunnelling and deep excavations – ground movements and their effects. Keynote Lecture, Proc. 15th European Conference on Soil Mechanics and Geotechnical Engineering, Athens, September 2011.
- McKinley, J.D. & Bolton, M.D. 1999. A geotechnical description of fresh cement grout: filtration and consolidation behaviour. *Mag. Concrete Res.* 51, No. 5, 295–307.
- Merritt, A. S., Mair, R. J. 2006. Mechanics of tunnelling machine screw conveyors: model tests. *Géotechnique* 56 (9): 605–615.
- Milligan, G.W.E., 2000. “Soil conditioning and lubrication in tunnelling, pipe jacking and microtunnelling. A State-of-the-art review”. August.
- Min, F., Zhu, W., & Han, X., 2013 Filter cake formation for slurry shield tunneling in highly permeable sand. *Tunnelling and Underground Space Technology* 38(9): 423-430.
- Mitchell, J. K., 1976. *Fundamentals of soil behaviour*. New York: John Wiley & Sons.
- Mooney, M.A., Wu, Y., Mori, L., Bearce, R., Cha, M., 2016. Earth Pressure Balance TBM soil conditioning: it’s about the pressure. In: *Proceedings of the ITA-WTC 2016, San Francisco*, pp. 22–28.

- Mori, L., Mooney, M. & Cha, M., 2018. Characterizing the influence of stress on foam conditioned sand for EPB tunneling. *Tunnelling and Underground Space Technology* 71 (2018): 454-465.
- Oung, O. & Bezuijen A., 2003. Selective pore pressure transducers for use in model tests to study two-phase flow in porous media. *International Journal of Physical Modelling in Geotechnics* 3 (4): 31-41.
- Peila, D., Oggeri, C., & Vinai, R., 2007. Screw conveyor device for laboratory tests on conditioned soil for EPB tunneling operations. *Journal Geotechnical and Geoenvironmental Engineering* 133: 1622–1625.
- Peila, D., Oggeri, C. & Borio, L., 2009. Using the slump test to assess the behaviour of conditioned soil for EPB tunnelling. *Environmental & Engineering Geoscience* XV (3): 167–174.
- Peila D., Borio L. & Pelizza S., 2011. The behavior of a two-component backfilling grout used in a tunnel boring machine. *Acta Geotechnica Slovenica* 1: 5-15.
- Pena, M., 2007. *Foam as a Soil Conditioner in Tunnelling: Physical and Mechanical Properties of Conditioned Sands*, Doctoral thesis. Oxford.
- Pitt M. J., 1999. The Marsh Funnel and Drilling Fluid Viscosity-A new Equation for Field Use. *SPE Drill Complet.* 15(1), 5-8.
- Psomas, S., 2001. *Properties of foam/sand mixtures for tunneling applications*. Master's thesis, Oxford.
- Quebaud, S., Sibai, M. & Henry, J.P., 1998. Use of chemical foam for improvements in drilling by earth pressure balance shields in granular soils. *Tunnelling and Underground Space Technology* 13 (2): 173-180.
- Rossen. W.R., 1990. Theory of Mobilization Pressure Gradient of Flowing Foams in Porous Media. *Journal of Colloid and Interface Science* 136 (1): 1-16.
- Rossen, W.R. & Gauglitz, P.A., 1990. Percolation Theory of Creation and Mobilization of Foams in Porous Media. *AIChE J.* 36: 1176–1188.
- Sadrizadeh S., Ghafar A.N., Halilovic A. & Hakansson U. (2017) Numerical, experimental and analytical studies on fluid flow through a Marsh funnel. *Journal*

of Applied Fluid Mechanics, 10 (6): 1501-1507.

Schoesser B. and Thewes M., 2015. Marsh funnel testing for rheology analysis of bentonite slurries for Slurry Shields. ITA WTC 2015 Congress and 41st General Assembly May 22-28, 2015, Lacroma Valamar Congress Center, Dubrovnik, Croatia.

Sedaghat A., 2017. A novel and robust model for determining rheological properties of Newtonian and Non-Newtonian fluids in a Marsh funnel, Journal of Petroleum Science and Engineering, doi: 10.1016/j.petrol.2017.06.057.

Skelland A.H.P., 1967. Non-Newtonian flow and heat transfer. John Wiley & Sons, New York.

Talmon, A. M. & Bezuijen, A., 2002. Muck discharge by the screw conveyor of an EPB tunnel boring machine, proceedings of the conference on geotechnical aspects of underground construction in soft ground, Toulouse, Vol. 1, pp. 89–94.

Talmon, A. M., Mastbergen, D. R., & Huisman, M., 2013. Invasion of pressurized clay suspensions into granular soil. Journal of Porous Media 16: 351-365.

Thewes, M., 2007. TBM Tunnelling Challenges—Redefining the State-of-the-Art, Keynote lecture at the 2007 ITA World Tunnel Congress, Prague, Tunnel. pp. 13–21.

Thewes, M., Budach, C. & Bezuijen, A., 2012. Foam conditioning in EPB tunneling. Geotechnical Aspects of Underground Construction in Soft Ground. London.

USACE (2000) Engineering Manual 1110-2-1913, Design and Construction of Levees.

https://www.publications.usace.army.mil/Portals/76/Publications/EngineerManuals/EM_1110-2-1913.pdf.

Vargaftik, N.M., Volkov, B.N. & Voljak, L.D., 1983. International Tables of the Surface Tension of Water. Journal of Physical and Chemical Reference Data. 12 (3): 817-820.

Wang, S., Hu, Q., Wang, H., Thewes, M., Ge, L., Yang, J. & Liu, P., 2021. Permeability Characteristics of Poorly Graded Sand Conditioned with Foam in Different

- Conditioning States. *Journal of Testing and Evaluation*. Published ahead of print, September 01, 2021, <https://doi.org/10.1520/JTE20190539>.
- Wei, Y., Yang, Y. & Qiu, T., 2019. Effects of Soil Conditioning on Tool Wear for Earth Pressure Balance Shield Tunneling in Sandy Gravel Based on Laboratory Test. *Journal of Testing and Evaluation* 49. <https://doi.org/10.1520/JTE20180851>.
- Winterwerp, J.C. & van Kesteren, W.G.M., 2004. *Introduction to the Physics of Cohesive Sediment in the Marine Environment, Developments in Sedimentology*, 56, Elsevier, New York.
- Wu, Y., Mooney, M.A. & Cha, M., 2018. An experimental examination of foam stability under pressure for EPB TBM tunneling. *Tunnelling and Underground Space Technology* 77 (2018): 80-93.
- Wu, Y., Nazem, A., Meng, F. and Mooney, M.A., 2020. Experimental study on the stability of foam-conditioned sand under pressure in the EPBM chamber. *Tunnelling and Underground Space Technology* 106 (2020): 103590.
- Van Genuchten, M. Th. 1980. A closed-form equation for predicting the hydraulic conductivity of unsaturated soils. *Soil Sci. Soc. Am. J.* 44:892-898.
- Vargaftik, N.M., Volkov, B.N. and Voljak, L.D., 1983 *International Tables of the Surface Tension of Water*. *Journal of Physical and Chemical Reference Data* 12 (3): 817-820.
- Xu, T., 2018. *Infiltration and excess pore water pressures in front of a TBM, Experiments, Mechanisms and Computational models*, Doctoral thesis. Ghent University, Belgium.
- Xu, T. & Bezuijen, A., 2018. Numerical methods in predicting excess pore water pressure in front of slurry shield in saturated sandy ground. *Tunnelling and Underground Space Technology* 73 (2018): 203–211.
- Xu, T. & Bezuijen, A., 2018. Pressure infiltration characteristics of bentonite slurry. *Géotechnique* 69 (4): 364-368.
- Xu, T., Bezuijen, A. & Dias T.G.S., 2018. Slurry infiltration ahead of slurry TBM in saturated sand: Laboratory tests and consequences for practice. *Geotechnical*

Aspects of Underground Construction in Soft Ground. London. pp. 121-126.

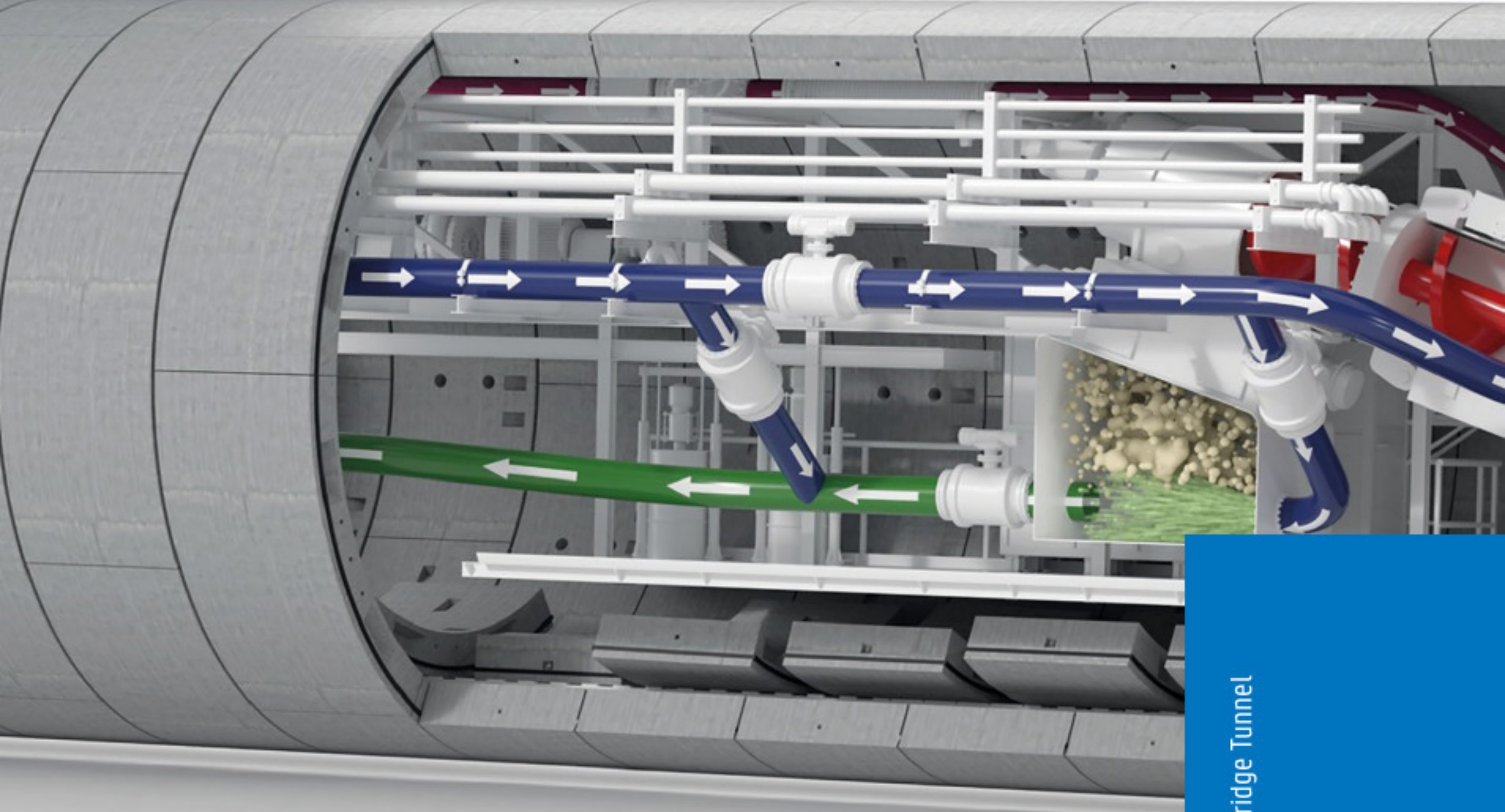
- Xu T. & Bezuijen A., 2019. Bentonite slurry infiltration into sand: filter cake formation under various conditions. *Géotechnique*, <https://doi.org/10.1680/jgeot.18.P.094>.
- Xu, T., Bezuijen, A. & Thewes, M., 2020. Pressure infiltration characteristics of foam for EPB shield tunnelling in saturated sand – part 1: ‘clean’ foam. *Géotechnique*. <https://doi.org/10.1680/jgeot.19.P.187>
- Xu, T., Bezuijen, A. & Thewes, M., 2020. Pressure-infiltration characteristics of foam for EPB shield tunnelling in saturated sand – part 2: soil–foam mixture. *Géotechnique*. <https://doi.org/10.1680/jgeot.19.P.188>
- Yin, T., Zhang, Z., Huang, X., Shire, T. & Hanley, K.J., 2021. On the morphology and pressure-filtration characteristics of filter cake formation: Insight from coupled CFD–DEM simulations. *Tunnelling and Underground Space Technology* 111 (2021): 103856. <https://doi.org/10.1016/j.tust.2021.103856>
- Yu, H., Mooney, M. & Bezuijen, A., 2020. A simplified excavation chamber pressure model for EPBM tunneling. *Tunnelling and Underground Space Technology*. <https://doi.org/10.1016/j.tust.2020.103457>.
- Zhang, N., Shen, S., Zhou, A. & Lyu, H., 2020. Challenges of earth-pressure-balance tunnelling in weathered granite with boulders. *Geotechnical Engineering, ICE Proceedings*, DOI: <https://doi.org/10.1680/jgeen.20.00030>.
- Zheng, D., Bezuijen, A., & Di Emidio, G., 2021. A new model for predicting the Marsh funnel test. *International journal of geomechanics*, 21(2): 06020042. [https://doi.org/10.1061/\(asce\)gm.1943-5622.0001913](https://doi.org/10.1061/(asce)gm.1943-5622.0001913)
- Zheng, D., Bezuijen, A. & Thewes, M. 2021. An experimental study on foam infiltration into saturated sand and its consequence for EPB shield tunneling. *Tunnelling and Underground Space Technology* 111 (2021): <https://doi.org/10.1016/j.tust.2021.103878>
- Zheng, D., Bezuijen, A. & Thewes, M., Model the infiltration behavior of foam into saturated sand considering the capillary resistance for EPB shield tunneling. In

preparation.

Zheng, D., Bezuijen, A. & Thewes, M., Experimental study on sandy foam infiltration into saturated sand for EPB shield tunneling: A Mechanism Study. In preparation.

Zizka, Z., Schoesser, M., Thewes, M., 2017. Excavation cycle dependent changes of hydraulic properties of granular soil at the tunnel face during slurry shield excavation, Proceedings of 9th International Symposium on Geotechnical Aspects of Underground Construction in Soft Ground, Sao Paulo.

Zizka, Z., Schoesser, B., Thewes, M., Schanz, T., 2018. Slurry shield tunneling: New methodology for prediction of increased pore pressures resulting from slurry infiltration at the tunnel face under cyclic excavation processes. International Journal of Civil Engineering 7: 113–130.



The variable density TBM built for the future Hampton Roads Bridge Tunnel Expansion Project (illustration by Herrenknecht AG).